DEPARTMENT OF PHYSICS
UNIVERSITY OF JYVÄSKYLÄ
RESEARCH REPORT No. 7/2012

NUMERICAL STUDIES OF TRANSPORT IN COMPLEX MANY-PARTICLE SYSTEMS FAR FROM EQUILIBRIUM

BY
JANNE KAUTTONEN

Academic Dissertation
for the Degree of
Doctor of Philosophy

To be presented, by permission of the
Faculty of Mathematics and Natural Sciences
of the University of Jyväskylä,
for public examination in FYS1 of the
University of Jyväskylä on October 1, 2012
at 12 o'clock noon

Jyväskylä, Finland
August 2012

Preface

This work has been conducted during the years 2006-11 in the University of Jyväskylä at the Department of Physics. This research has provided both days with enthusiasm and the joy of discovering new, but also days with despair and frustration. However, by experiencing these both, I have learned much more during this time and I am ready for future challenges.

I am grateful to my supervisors, Juha Merikoski for his guidance and support during these years, and Otto Pulkkinen for his assistance in finishing this Thesis. I also had a pleasure to work with Janne Juntunen, a past member of our small but devoted statistical physics research group. The overall working atmosphere at the Physics Department has been pleasant.

Financial support from the Finnish Academy of Science and Letters (Väisälä fund), the Magnus Ehrnrooth Foundation, the Emil Aaltonen Foundation and the Rector of the University of Jyväskylä is gratefully acknowledged.

Finally I would like to thank my family and my beloved Sanni for their encouragement and support.

Jyväskylä, August 2012

Janne Kauttonen

Abstract

Kauttonen, Janne
Numerical studies of transport in complex many-particle systems far from equilibrium
Jyväskylä: University of Jyväskylä, 2012
(Research report/Department of Physics, University of Jyväskylä,
ISSN 0075-465X; 7/2012)
ISBN paper copy: 978-951-39-4786-6
ISBN electronic: 978-951-39-4787-3

In this Thesis, transport in complex nonequilibrium many-particle systems is studied using numerical master equation approach and Monte Carlo simulations. We focus on the transport of the center-of-mass of deformable objects with internal structure. Two physical systems are studied in detail: linear polymers using the Rubinstein-Duke model and single-layer metal-on-metal atomic islands using a semi-empirical lattice model. Polymers and islands are driven out of thermodynamic equilibrium by strong static and time-dependent external forces. Topics covered in this work include introductions to nonequilibrium statistical mechanics, master equations and computational methods, with construction and numerical solving of master equations, and numerical optimization. For small systems (up to $\sim 10^6$ states), solving master equations numerically is found to be efficient, especially when studying parameter sensitive and elusive properties, such as drifts caused by the ratchet effect. Speed and accuracy of the method allows optimization with respect to continuous model parameters and transition cycles, which helps in understanding the coupling between the internal dynamics of deformable objects and their center-of-mass displacement.

Firstly, we study transport of polymers in spatially periodic time-dependent potentials using a standard and relaxed versions of the Rubinstein-Duke model. Two types of potentials, flashing and traveling, are considered with stochastic and deterministic time-dependency schemes. Rich non-linear behavior for the transport velocity, diffusion and energetic efficiency is found. By varying the polymer length, we find current inversions caused by a 'rebound' effect that is only present for objects with internal structure. These results are different between reptating and non-reptating polymers. Transport is found to become more coherent for deterministic time-dependency scheme and as the polymer gets longer. The results show that small changes in the molecule structure (*e.g.* the charge configuration) and the environment variables can lead to a large change in the velocity.

Secondly, we study transport of single-layer metal-on-metal islands using a semi-empirical lattice model for Cu atoms on Cu(001) surface. Two types of time-dependent driving are considered: a pulsed rotated field and an alternating field with a zero average force (an electrophoretic ratchet). The main results are that a pulsed field can increase the velocity in both diagonal and axis directions as compared to a static

field, and there exists a current inversion in an electrophoretic ratchet. In addition to a 'magic size' effect for islands in equilibrium, a stronger odd-even effect is found in the presence of large fields. Master equation computations reveal nonmonotonous behavior of the leading relaxation constant and effective Arrhenius parameters. Optimized transition cycles shed light on microscopic mechanisms responsible for island transport in strong fields.

Author's address Janne Kauttonen
Department of Physics
University of Jyväskylä
Finland

Supervisors Docent Juha Merikoski
Department of Physics
University of Jyväskylä
Finland

Doctor Otto Pulkkinen
Department of Physics
Tampere University of Technology
Finland

Reviewers Doctor Jan Åström
CSC - IT Center for Science Ltd.
Finland

Professor Mikko Karttunen
Department of Chemistry
University of Waterloo
Canada

Opponent Professor Joachim Krug
Institute for Theoretical Physics
University of Cologne
Germany

List of Publications

The main results of this Thesis have been reported in the following articles:

I J. Kauttonen, J. Merikoski, and O. Pulkkinen: *Polymer dynamics in time-dependent periodic potentials*, Phys. Rev. E **77**, 061131 (2008). doi:10.1103/PhysRevE.77.061131.

II J. Kauttonen and J. Merikoski: *Characteristics of the polymer transport in ratchet systems*, Phys. Rev. E **81**, 041112 (2010). doi:10.1103/PhysRevE.81.041112.

III J. Kauttonen and J. Merikoski: *Single-layer metal-on-metal islands driven by strong time-dependent forces*, Phys. Rev. E **85**, 011107 (2012). A separate supplemental material to this article is available on the corresponding website of the article. doi:10.1103/PhysRevE.85.011107

The Author of this Thesis has done all theoretical and numerical computations, and performed all data analysis. He has written the first versions of all the articles.

Contents

1 Introduction

Research of transport of complex molecular and micro-scale objects has flourished in the last two decades. Important discoveries have been made and knowledge has been gained on molecular motors, polymers and in surface physics, where the development in experimental and computational techniques have reached the level which allows studying and manipulation of individual molecules and atoms [85, 34, 33]. Theoretical research of simplified models has a center stage in unraveling the operational principles of these systems. In this work two complex micro-scale systems are studied: linear polymers and single-layer atomic islands [5, 86, 110, 139]. We apply a master equation approach and simulations, and concentrate on the transport properties of polymers and islands under the effect of strong static and time-dependent external forces. Topics covered in this work include introductions to nonequilibrium statistical mechanics, master equations and computational methods, with construction and numerical solving of master equations, and numerical optimization.

Statistical mechanics consists of two rather different parts: equilibrium and nonequilibrium statistical mechanics. A system is said to be in thermodynamic *equilibrium* when it is thermally, mechanically, radiatively and chemically in balance, *i.e.* there are no net flows of matter or energy, no phase changes, and no unbalanced potentials or driving forces, within the system [27]. An equilibrium system experiences no changes when it is isolated from its surroundings. If any of these conditions is not met, the system is in a *nonequilibrium* state [75].

The success of equilibrium statistical mechanics has been spectacular. It has been developed to a high degree of mathematical sophistication, and applied with success to subtle physical problems like the study of critical phenomena. By contrast, the progress of nonequilibrium statistical mechanics has been much slower. For systems in equilibrium, everything is well understood and validated, but as the systems and processes of interest are taken further from thermodynamic equilibrium, their study becomes much more difficult. We still depend on the insights of Boltzmann for our basic understanding of irreversibility, and further progress has been mostly on dissipative phenomena close to equilibrium, resulting in Onsager reciprocity relations, Green-Kubo formula, and related fundamental results [75, 27, 138]. Theory of nonequilibrium systems is still immature and under development. Indeed, developing a fundamental and comprehensive understanding of physics far from equilibrium is recognized to be one of the 'grand challenges' of our time, by both the US National Academy of Sciences and the US Department of Energy [33, 201]. Perhaps the most

striking feature of nonequilibrium systems is the possibility for mass transport. Transport near equilibrium is covered by the linear response theory and is generally well understood. On the other hand, far from equilibrium, complex and strongly system-dependent, non-linear transport phenomena arise. The motivation behind this work is to gain understanding about these phenomena.

The master equation approach is an efficient way to study the statistical mechanics of complex nonequilibrium many-particle systems. In this work, we concentrate on the numerical methods for large master equation sets and provide in-depth analyses of discrete state polymer and single-layer metal island models in nonequilibrium conditions. Both polymers and atomic islands have large numbers of internal configurations. Our main focus lies on the transport properties of these deformable objects, which are very different from objects without internal structure, such as point-like particles. Nonequilibrium state is obtained by introducing strong static and time-dependent potentials that force the system out of equilibrium.

In the first part of this work, we concentrate on the numerical solution methods of master equations. If the number of master equations is of order 10^6 or less, numerically exact results for the probability distribution and observables of nonequilibrium models can be computed. As opposed to the Monte Carlo simulations, which is the traditional numerical method, speed and accuracy of the numerical master equation method allows numerical optimization with respect to continuous model parameters and transition cycles. This helps in understanding the coupling between the internal dynamics of deformable objects and their center-of-mass displacement. Numerical master equation approach has been previously used mostly in studies of chemical reaction networks (*e.g.* stoichiometry) and related fields [63]. In this work, we show that this method can be also used as a standard tool in studies of complex many-particle systems in nonequilibrium statistical physics. This has became possible mainly due to the recent advances in computer technology and numerical methods, particularly in linear algebra and optimization. In this Thesis, we will cover all necessary theoretical and numerical aspects of the master equation method for nonequilibrium discrete models.

The Thesis is organized as follows. In Chapter 2, the theoretical basis of nonequilibrium systems, the ratchet effect and master equations are presented. The presentation is kept general without making assumptions of any specific models. In Chapter 3 we present and define the models and observables studied in this work. In Chapters 4 and 5, methods to set up and solve master equations are discussed. In Chapters 6 and 7, results for the repton and island model are presented and discussed. Finally, in Chapter 8, the summary and outlook of this Thesis is presented.

2 Theory

In this Chapter, the general theoretical background of the Thesis is presented. To keep the representation compact and readable, many mathematical details are omitted. We concentrate on systems with a finite discrete set of states, with brief exceptions made in Sections 2.1.4 and 2.2.1.

2.1 Statistical mechanics

2.1.1 Systems in and out of equilibrium

The fundamental property of the equilibrium is that the probability to find the system in a given state follows the *Boltzmann distribution* [138]

$$P_{\mathrm{eq}}(y) = \frac{1}{Z} e^{\frac{-E(y)}{k_{\mathrm{B}}T}}, \tag{2.1}$$

where y denotes the microstate of the system with energy $E(y)$, k_{B} is the Boltzmann constant, T is the temperature and $Z = \sum_y \exp\left(-E(y)/k_{\mathrm{B}}T\right)$ is the partition function over all available microstates in the canonical ensemble. The second requirement for thermodynamic equilibrium is the *local detailed balance* condition [138]

$$P_{\mathrm{eq}}(y)W(y', y) = P_{\mathrm{eq}}(y')W(y, y'), \tag{2.2}$$

where $W(y', y)$ is the transition rate (probability per unit time) for a transition from state y to state y'. The products of the form $P(y)W(y, y')$ are called *probability flows* or *currents*. Together with the distribution P, these flows have a special role in characterizing the steady states uniquely [200]. For discrete time systems, W is the transition probability (see Section 2.2.3 for more details). The detailed balance condition is a very strong property, because it indicates that there cannot be net currents between any states in the system, and if $W(y, y')$ is non-zero, then also $W(y', y)$ must be non-zero. From the detailed balance condition, it also follows that the dynamics of the equilibrium system is independent of the direction of time and the entropy production of the system is zero.

For a nonequilibrium system, equations (2.1) and (2.2) do not hold. There is no general paradigmatic theoretical framework that describes nonequilibrium systems, neither in

thermodynamics nor in statistical mechanics [75, 194]. Especially, this means that there is no general principle whereby one can calculate the distribution of the system's states from the sole knowledge of the system's invariants or external constraints imposed on the system. At present, the most promising results in the search for universal properties of nonequilibrium systems are the fluctuation and pumping theorems [76, 29, 8]. These theories go beyond linear response regime (see below), but the practical usefulness of these expansions remains an open question. They provide certain limits and requirements for the work and current distributions, but do not provide an actual access to their distributions [8]. Numerical methods remain the main tool to study complex systems far from equilibrium.

In this work, we only consider *ergodic* (*irreducible*) systems, which means that the system has a non-zero probability to visit all microstates regardless of the initial state. If this is not true, then the system consists of disconnected sub-systems (the system is *decomposable*) and each sub-system can be treated as separately from each other. Any ergodic system finally relaxes to an unique *steady state* corresponding to a function W if allowed to run infinitely long. For equilibrium systems, W must be time-independent and lead to the Boltzmann distribution with the detailed balance [138]. A nonequilibrium state can be steady or *transient*. A transient nonequilibrium state appears, for example, after the system is suddenly pushed out of equilibrium. If the system is pushed out of equilibrium with periodic or constant forces, the system will end up in a *nonequilibrium steady state*. In this work, we mainly concentrate on the latter type of nonequilibrium systems.

2.1.2 Linear response theory

It is known empirically, that for a large class of irreversible phenomena and under a wide range of experimental conditions, irreversible flows are linear functions of thermodynamic forces [120, 27]. Majority of studies and theory of nonequilibrium statistical mechanics are limited within the linear response regime near the equilibrium. When thermodynamic forces are introduced in a system in thermodynamic equilibrium, irreversible dynamics with currents appear. If the forces are small, the response of the system can be linearized such that

$$\dot{X}_i = \sum_j L_{i,j} F_j,$$

where F_j are the thermodynamic forces and X_i are the resulting currents. The coefficients $L_{i,j}$ are called *Onsager kinetic coefficients*. Positive definiteness of entropy production requires that $L_{i,i} \geq 0$ and by the local detailed balance condition, one gets Onsager's principle $L_{i,j} = L_{j,i} \geq 0$ [107]. Many well-known relations, such as Ohm's, Fourier's and Fick's laws, indeed rely on the linear response. The cornerstone of the

linear response theory is the *fluctuation-dissipation theorem*, which states a general relationship between the response of a given system to an external disturbance and the internal fluctuation of the system in the absence of the disturbance. Perhaps the best known example of the fluctuation-dissipation theorem is the Einstein relation

$$D = \mu k_{\mathrm{B}} T,$$

where D is the diffusion coefficient at equilibrium and $\mu = v/F$ is the mobility, which is the drift velocity of the object, divided by the total force F affecting the system. This means, that $v \propto D$ for small forces, *i.e.* the equilibrium diffusion coefficient can be determined from nonequilibrium currents near equilibrium, which is often much easier than trying to evaluate D directly. By checking the linearity of the drift, one can also get an idea of how close to equilibrium the system is. The fluctuation-dissipation theorem is useful because it gives a relation between two quantities related to two essentially different processes, *e.g.* drift and fluctuations.

2.1.3 Graph representation

The function W in Eq. (2.2), which consist of allowed transitions between microstates, can be also understood as a graph: If $W(i, j) > 0$, there is a connection (*edge*) between states (*vertices*) i and j. The process defined by W then becomes equivalent to a random walk on a graph [16, 117, 95]. The topology and the complexity of the graph depends on the details of the system. A time-dependent set of vertices connected by edges is called a *path* and its time-independent counterpart a *sequence*. For an ergodic system, the graph consists of a single strongly connected component, *i.e.* there exists a sequence between any two vertices in the graph. Sequences with the same starting and ending vertices are called *cycles*, and they have a special importance in the theory of nonequilibrium systems. For equilibrium systems, it follows from Eq. (2.2) that for every cycle C one has

$$\prod_{\langle i,j\rangle \in C} \frac{W(i,j)}{W(j,i)} = 1,$$

where $\langle i, j\rangle$ is a directed edge in the configuration graph. A system with this property is said to have a *balanced dynamics*. This condition does not generally result in Eq. (2.2). For non-equilibrium systems, the right-hand side of the above equation is replaced by $\exp(A(C))$ for some cycles, where the *affinity* (or a macroscopic force) $A(C)$ of the cycle measures the deviation from equilibrium and is generally non-zero. Cycles with non-zero affinities are sometimes called 'irreversible rate loops'. In his seminal paper in 1970s, Schnakenberg formulated a theory of macroscopic observables as circulations of local forces, and identified the total entropy production of a thermodynamic system using cycles and their affinities [165]. It is currently unclear, whether there exists an intuitively accessible and simple relationship between current

circulations and non-zero affinities [33]. It has been found, that circulations give rise to the stochastic resonance effect [142]. One of the major differences between equilibrium and nonequilibrium systems is, that, for an equilibrium system, the steady state distribution P_{eq} does not depend on the topology of the graph, *i.e.* for an ergodic system, the distribution remains the same for different placements of edges between vertices. However, for transport properties, the topology of the graph is important for both kind of systems.

2.1.4 The ratchet effect

The properties of nonequilibrium systems depend on how they are driven out of equilibrium. In this work we are especially interested in systems under thermal random motion with the presence of time-dependent forces, whose time-averaged force remains zero, but yet there exists net transport of mass. The transport arises as a subtle interplay between nonlinearities in the system and broken symmetries. This type of noise induced transport is generally known as a *ratchet effect* [148] and it is different from the usual predictable mechanical transport, that follows directly from the gradients of the forces. Due to fluctuations, the time-evolution of state variables, such as the position of an object, are not directly coupled to the time-evolution of potentials, and large deviations from an average trajectory can occur. State variables of microscopic systems in noisy environment are therefore said to be loosely coupled with potentials, whereas a macroscopic apparatus always displays tight coupling.

For biological systems, ratchet effect poses one of the mechanisms how they manage to keep themselves in ordered states even while surrounded by significant thermal noise and environmental fluctuations. In the inorganic and macroscopic world, transport always take place along a gradient of the potential, such as gravitation, electric field, chemical imbalance and temperature differences. This is not how transport is achieved for most biological systems. For example, thermal gradients are essentially impossible to maintain over small distances, hence the thermal gradients necessary to drive significant motion are not realistic. With the ratchet effect, directed motion is possible without long-range gradients [11, 85, 4, 182].

The ratchet effect discussed here takes place when the following conditions are met: (1) the system is spatially periodic, (2) there is some asymmetry in the potentials, and (3) the system is out of equilibrium. We will next distinguish between the main types of ratchets. For this, it is more convenient to consider a single overdamped[1] Brownian particle in a periodic one-dimensional potential $V(x + L, t) = V(x, t)$, where L is the spatial period of the potential. The main classification of ratchets remains the same

[1]For overdamped particles the effect of inertia is neglected, *i.e.* an approximation $\ddot{x}(t) \approx 0$ is applied.

for discrete systems and non-Gaussian noises. The equation of motion for a Brownian particle, also known as the Langevin equation, in a medium is

$$\eta\dot{x} = -\frac{\mathrm{d}}{\mathrm{d}x}V(x,t) + F + y(t) + \varepsilon(t),$$

where η is a friction coefficient, F is a constant load-force, $y(t)$ is a time-dependent force and $\varepsilon(t)$ is a random motion (noise). The most studied and familiar type of noise is the Gaussian one (*i.e.* white noise), for which $\langle\varepsilon(t)\varepsilon(s)\rangle = 2\eta k_\mathrm{B}T\delta(s-t)$ and $2\eta k_\mathrm{B}T = D$ is identified as a diffusion coefficient.[2] The potential V is expected to originate from the medium, whereas F and y result from external fields.

Based on the choice of V, two distinct types of ratchets can be defined: *fluctuating potential ratchet* with $V(x,t) = V(x)\,[1 + W(t)]$ and *traveling potential ratchet* with $V(x,t) = V(x - W(t))$. In the first one, the amplitude of the potential and in the second one the location fluctuates. For the first type, two especially interesting and widely used potential types can be identified:

- On-off ratchet: $V(x,t) \in \{V(x), 0\}$, $F = y(t) = 0$.
- Rocking ratchet: $V(x,t) = V(x)$ and $\langle F + y(t)\rangle_t = 0$

The ratchet effect occurs when $d\langle x\rangle/dt \neq 0$ for $\langle -dV(x,t)/dx + F + y(t)\rangle = 0$, *i.e.* there is a net drift in the presence of a vanishing mean force.

For the ratchet effect to take place, the magnitude of potentials V, y and F are typically of same magnitude as the thermal energy $k_\mathrm{B}T$. For zero temperature, the ratchet effect vanishes. *Current inversions*, which means that the transport direction turns around, are found to be rather common and can usually be generated by particle interactions and tuning of variables (*e.g.* diffusion constant, friction, potential shape and period) [148, 106, 196, 32, 38, 31, 26, 109, 100]. Since the systems utilizing the ratchet effect work under nonequilibrium conditions, they are exactly solvable only in simplest cases. Some exact results can, however, be often derived at different limits, such as very small/large potentials and slowly/fast changing potentials, for which the results from the equilibrium statistical mechanics can be utilized in some form.

The first major contribution towards the studies of the ratchet effect was by Smoluchowski in his Gedankenexperiment in 1912, regarding to the absence of directed transport in a system consisting only a single heat bath [174]. The next important step was taken by Feynman using the famous 'ratchet and pawl' model, for which the quantitative analysis was published in 1962 and which showed, that that external work is required for the machine to perform useful work [62].[3] However, it was the works by

[2] For this reason, the term *Brownian motor* is often used for objects that utilize the ratchet effect.

[3] See Ref. [89] for an exactly solvable discrete counterpart of the 'ratchet and pawl' model.

Ajdari, Prost, Magnasco *et al.* in early 1990's, that provided the inspiration for a whole new wave of great theoretical and experimental activity, and progress within the statistical physics community [141, 118]. Another root of Brownian motor theory origins from the intracellular transport research, specifically the biochemistry of molecular motors and molecular pumps [186]. Most studies, especially the theoretical ones, have concentrated on one dimensional systems and white thermal noise. More recently, two-dimensional systems, complicated potentials, colored noises and non-point-like objects have been considered [54, 97, 68, 121, 140, 22, 14, 169, 190, 59, 187, 60, 149, 187]. The ratchet effect has been also studied in other contexts, such as the game theory, where the so-called *Parrondo's paradox* is a discrete counterpart to the Brownian particle version [133].

2.2 The Master equation

In this section we derive, motivate and discuss properties of master equations which form the mathematical framework of this work. Master equations describe the time-evolution of a system, that can be modeled as being in exactly one of countable number of states at any given time, such that the switching between the states is treated probabilistically. A system governed by the master equations can be interpreted as *random walks* and are therefore often called jump processes.

Despite the simplicity of the master equation, it has been a subject for decades of theoretical research and countless applications. Typical examples of usage in physics are lattice models (*e.g.* simple exclusion and zero-range processes) and Fermi-Golden rule in quantum mechanics. Theoretical research of nonequilibrium systems have been mostly done within the context of master equations, resulting in *e.g.* fluctuation and pumping theorems. A large portion of theoretical and numerical research of master equations have been done particularly in the area of chemistry, where they are used to model chemical reactions (*e.g.* reaction networks). The popularity of master equations is also explained by their close relation to the Fokker-Planck equation and different types of random walks, in both discrete and continuous space and time.[4]

2.2.1 Derivation

In the following, a derivation of master equations is given, starting from a generic random process. More comprehensive and mathematically rigorous derivations can be

[4]For example, the Fokker-Planck equation gives the distribution for a particle governed by the Langevin equation [152]. On the other hand, these two can be recovered from the appropriate discrete random walks at the limit of infinitesimal spatial and/or temporal steps.

found in several textbooks such as [129, 73, 66].

Consider a stochastic process $Y(t)$ in continuous time and space. According to the Bayes' rule, the following identity holds for the joint probability:

$$P(y_1, t_1; y_2, t_2) = P(y_1, t_1)P(y_2, t_2|y_1, t_1),$$

where $P(y_2, t_2|y_1, t_1)$ is the conditional probability and $y_i := Y(t_i)$. Now, if for all successive times $t_1 < t_2 < \cdots < t_n$ the condition

$$\begin{aligned} P(y_1, t_1; y_2, t_2; \ldots; y_n, t_n) &= P(y_1, t_1)P(y_2, t_2; \ldots; y_n, t_n|y_1, t_1) \\ &= P(y_1, t_1)P(y_n, t_n|y_{n-1}, t_{n-1}) \ldots P(y_2, t_2|y_1, t_1), \end{aligned}$$

holds, then the process $Y(t)$ is called a *Markov process*. Such process is completely determined if one knows $P(y, t)$ and $P(y_2, t_2|y_1, t_1)$, *i.e.* the probability to be in the given state in a given time, and the probability for a transition to another state from the previous [177]. The future state of the process depends only on the present state and not on the past history. For the case $n = 3$ and integrating the equation above, one receives the identity

$$P(y_3, t_3; y_1, t_1) = \int P(y_3, t_3|y_2, t_2)P(y_2, t_2|y_1, t_1)dy_2, \tag{2.3}$$

which is known as the Chapman-Kolmogorov equation for Markov processes. A Markov process is fully determined by $P(y, t)$ and $P(y_2, t_2|y_1, t_1)$, but these functions cannot be chosen arbitrarily. Two properties are required: Non-negative and properly normalized functions $P(y, t)$ and $P(y_2, t_2|y_1, t_1)$ satisfying Eq. (2.3) and

$$P(y_2, t_2) = \int P(y_1, t_1)P(y_2, t_2|y_1, t_1)dy_1$$

uniquely define a Markov process.

The conditional transition probability can be expanded in time such that

$$P(y_2, t_1 + \delta t|y_1, t_1) = \delta(y_1 - y_2)\left[1 - A(y_1)\delta t\right] + \delta t H(y_2|y_1) + O(\delta t^2), \tag{2.4}$$

where $H(y_2, y_1) \geq 0$ is the transition probability per unit time from y_1 to y_2. The coefficient $1 - A(y_1)\delta t$ is the probability that no transition takes place during δt. Normalization requires that

$$A(y_1) = \int H(y_2|y_1)dy_1.$$

Substituting this into (2.3) and taking the limit $\delta t \to 0$ leads to the differential form of the Chapman-Kolmogorov equation,

$$\frac{dP(y, t|y_0, t_0)}{dt} = \int \left[H(y|y')P(y', t'|y_0, t_0) - H(y'|y)P(y, t|y_0, t_0)\right] dy',$$

which is known as the master equation. For a system with a discrete state space, which is the case considered in this work, master equations have a form

$$\frac{dP_y(t)}{dt} = \sum_{y' \neq y} \left[H_{y,y'} P_{y'}(t) - H_{y',y} P_y(t) \right], \tag{2.5}$$

where the function H includes all states of the system with $H_{y',y} > 0$ for allowed transitions between states and zero to others. This type of a process is also called as a *continuous-time Markov chain*. The expected transition time from state y to state y' is given by $1/H_{y',y}$. Therefore, the average lifetime of state y is simply $1/\sum_{y' \neq y} H_{y',y}$. Alternatively, master equations can be written in the form

$$\frac{dP_y(t)}{dt} = \sum_{y' \neq y} \left[J_{y,y'}(t) - J_{y',y}(t) \right],$$

where $J_{y,y'}(t) := H_{y,y'} P_{y'}(t)$ is the probability flow from state y' to state y.

Because H creates the dynamics for the process, it is called a *stochastic generator* of the Markov chain. Particularly in physics, it is also known as a Liouville operator or a stochastic Hamiltonian. Although the underlying process is random, the time-evolution of the probability is deterministic. Random realizations (paths) of the process can be sampled with Monte Carlo methods, whereas the probability distribution can be numerically computed with differential equation solvers. These methods are discussed in detail in Chapter 5.

Finally we note that, from the Markov property, it follows that the waiting time distributions of jumps are exponentially distributed. This can be also seen by starting from the so called *generalized master equation*, which includes arbitrary time-dependent memory kernels. By assuming exponential waiting times, the memory kernels then reduces to constants, which are identified as rates $H_{y,y'}$, leading to Eq. (2.5). See Refs. [96, 57] for additional details of this connection.

As an example, at the end of this subsection, let us consider a homogeneous continuous-time random walk on one-dimensional infinite lattice. At time $t = 0$, the random walker is at the origin, *i.e.* $n(t = 0) = 0$, and the walker moves to left or right neighbor lattice site with a finite rate $\gamma > 0$. Master equation for this process is

$$\frac{dP_n(t)}{dt} = \gamma P_{n-1}(t) + \gamma P_{n+1}(t) - 2\gamma P_n(t),$$

where $P_n(t)$ is the probability for $n(t)$. To solve this, we note that since jump times and directions are clearly two independent processes, the solution of this process has

the form

$$P_n(t) = \sum_{i=0}^{\infty} \widehat{P}_i(t)\widetilde{P}_i(n),$$

where $\widehat{P}_i(t)$ is the probability for i events until time t and $\widetilde{P}_i(n)$ is the probability to end up at point n with i jumps. The first is the Poisson distribution, while the latter is given by the Bernoulli distribution shifted to the origin. Plugging them in, the complete solution reads

$$P_n(t) = \sum_{i=0}^{\infty} \frac{(\gamma t)^i \exp(-t\gamma)}{n!} \frac{1}{2^i} \frac{i!}{\left(\frac{i-n}{2}\right)! \left(\frac{i+n}{2}\right)!} = \exp(-t\gamma) I_n(\gamma t),$$

where $I_n(\gamma t)$ is a modified Bessel function. For large spatial and temporal scales, this process is analogous to Brownian motion on real axis. For more than one rate, the problem becomes much more complicated, since the above two processes are no longer separable. The models studied in this work (see Sections 3.3 and 3.4) can be viewed as extensions of this simple model, with much more complicated state-space with non-homogeneous and time-dependent rates, hence only the numerical solution methods can be applied.

2.2.2 Transition rates

The master equation is only useful if one knows the transition rates of the process. For a physical model, there are basically two ways to get them. The first way is to calculate them from some 'microscopic' model. The other is to derive them from experimental or simulation data. If master equations are used to model a thermodynamic system, the elements of H must be chosen such that the equilibrium conditions (2.1), (2.2) and ergodicity, discussed in Section 2.1, are fulfilled. There is no guarantee that these conditions are fulfilled if the rates are taken directly from an experiment or some microscopic simulation. In this work, we only consider models for which these conditions hold.

Conditions (2.1) and (2.2) do not specify the transition rates uniquely, but only their ratios. Despite the large number of studies with discrete nonequilibrium models, the importance of choosing the rates $H_{i,j}$ has not got much attention. However, this choice becomes very important when studying transport in complicated potentials. The usual choices for the rates are [84, 92]

$$H_{i,j}/\Gamma = \begin{cases} \min\left\{1, e^{(E_j - E_i)/k_B T}\right\} & \text{(Metropolis)} \\ e^{(E_j - E_i)/2k_B T} & \text{(exponential)} \\ \left[1 + e^{(E_i - E_j)/k_B T}\right]^{-1} & \text{(Kawasaki),} \end{cases}$$

where the constant $\Gamma > 0$ sets the time-scale. All three definitions lead to Boltzmann distribution in equilibrium and fulfill local detailed balance (2.2), but generate the different kinds of dynamics.

Being fast and simple, the Metropolis form is usually the first choice for the rates. Especially when studying the ratchet effect, it can be a poor choice since it does not take into account the slope of the downhill moves (rate being limited to Γ), that can be important for the dynamics. This is also the case for the Kawasaki form, since it is basically just a smoothened Metropolis function. Differences between the above three rate types are demonstrated in Section 6.1 for the repton model. The selection of suitable rates must be made on experimental or other system-specific grounds.

2.2.3 Properties and representations

In this Section we consider some important general properties of the master equation set. As noted before, we consider only systems with a finite number of states.[5]

Matrix form and eigenstates

Setting $H_{y,y} = -\sum_{y'} H_{y',y}$, master equations of the form (2.5) can be written in a compact matrix form

$$\frac{dP(t)}{dt} = H(t)P(t), \tag{2.6}$$

where the probabilities of states are given by components of vector $P(t)$. In the literature, matrix H is sometimes called a Q-matrix. It has following properties:

- If H is nonsymmetric, its left and right eigenvector sets $\langle\psi_i|$ and $|\varphi_i\rangle$ are different but have the same eigenvalues λ_i. Eigenvector sets are non-orthogonal, *i.e.* $\langle\varphi_i|\varphi_j\rangle \neq 0$ for $i \neq j$ (and similarly for $\langle\psi_i|$), but create a bi-orthogonal set $\langle\psi_i|\varphi_j\rangle = 0$ for all $i \neq j$.
- H is negative semidefinite, *i.e.* its eigenvalues are less than or equal to zero.
- There exists at least one eigenstate with an eigenvalue zero. If H is irreducible, there is exactly one eigenstate corresponding to eigenvalue zero, meaning that the steady state is unique.
- Non-zero eigenvalues can contain an imaginary part, in which case they come in complex-conjugate pairs.

[5] Many of the properties covered in this Section also hold for countably infinite number of states, but then many mathematical complications related to uniqueness and normalization arise.

The right eigenstate corresponding to the eigenvalue zero is the most important one, since it is the *steady state* solution of time-independent H. The steady state is a time-homogeneous probability distribution which describes the system in the long-time limit. The corresponding left eigenstate can be used to compute expected values of observables (see below).

Above properties essentially follow from elementary linear algebra and the following form of the Perron-Frobenius theorem: If a square matrix A is non-negative and irreducible, then

1. A has a positive real eigenvalue $\tilde{\lambda}$ which is equal to its spectral radius, *i.e.* $\tilde{\lambda} = \max_k |\lambda_k(A)|$, where $\lambda_k(A)$ denotes the k^{th} eigenvalue of A.
2. $\tilde{\lambda}$ corresponds to an eigenvector with all its entries being real and positive.
3. $\tilde{\lambda}$ is a simple eigenvalue of A.

This theorem applies to H through its time-development operator (discussed later) with the properties given above [94, 65].

The non-symmetry property of H turns out to be problematic for both theoretical and numerical analysis [69]. This is especially true in the absence of detailed balance.[6] Complex eigenvalues result in oscillations in time-dependent states and can be related to the stochastic resonance effect [142, 143]. Since the columns of the matrix H sum to zero, the rank of the matrix is always one less than the dimension of the matrix, *i.e.* the matrix H is singular. However, this poses no problem, since we also have normalization conditions, which ensures the uniqueness of the linear and eigenvalue problems related to H.[7]

The matrix H has right and left vectors corresponding to the same eigenvalues, *i.e.* $H|\varphi_y\rangle = \lambda_y|\varphi_y\rangle$ and $\langle\psi_y|H = \langle\psi_y|\lambda_y$. Using normalization $\langle\psi_i|\varphi_j\rangle = \delta_{i,j}$, the formal solution of (2.6) is given by $|P(t)\rangle = \exp\left(\int_{s=0}^{t} H(s)ds\right)|P(0)\rangle$, where $|P(0)\rangle$ is the initial state. This time-dependent state $|P(t)\rangle$ is a transient state. For a time-independent H, this can be expressed using the eigenvectors

$$|P(t)\rangle = \sum_y \langle\psi_y|P(0)\rangle e^{\lambda_y t}|\varphi_y\rangle,$$

which is known as the eigenfunction expansion.

[6] With detailed balance, the matrix H can be diagonalized using the equilibrium steady state P^{eq} with a transformed symmetric matrix $\widehat{H}_{i,j} = \left(P_j^{\text{eq}}/P_i^{\text{eq}}\right)^{1/2} H_{i,j}$

[7] For example, when solving problems $Hx = 0$ and $Hx = b$, one can replace one row of H with ones and use normalization conditions.

If an observable of interest can be put into a matrix form, *i.e.* it only depends on the probability distribution, its expected value can be computed using

$$\langle O(t)\rangle = \sum_i O_i P_i(t) = \langle \psi_0|O|P(t)\rangle, \tag{2.7}$$

where O is the operator of the observable and $\langle\psi_0|$ is the left eigenstate corresponding to the eigenvalue zero such that $\langle\psi_0|P(t)\rangle = 1$ holds. To compute long-time averages, the steady state distribution for $|P(t)\rangle$ is used, which is either time-independent or periodic in time. Note that, if the chosen basis is the natural basis, which is usually the best choice, the operator O is a diagonal matrix and one can also compute $\langle O(t)\rangle = \mathrm{Tr}(OP(t))$. Similarly, the variance $\langle O\rangle^2 - \langle O^2\rangle$ describing the fluctuation, can be computed using the operator with squared elements.

Operator formalism

For some stochastic systems, H can be naturally build with local operators. For such operator formalism to be efficient, a compact, fixed lattice representation is required. By compactness, we mean that the matrix H is irreducible, hence there are no empty rows or columns corresponding to null states when using the natural basis.[8] In physics, such models are often one or two dimensional simple models of particle motion. Typical examples are simple exclusion processes (1D), zero-range processes (1D), Hubbard model (1D) and Ising model (1D and 2D). In the operator formalism, the stochastic generator has a general form

$$H = \sum_{I\in\mathcal{L}} \left[E(I) - D(I)\right],$$

where the index set I goes through a fixed finite lattice $\mathcal{L}$, and operators E and D include off-diagonal (*i.e.* interactions) and diagonal elements. Operators E and D contain second quantization type local operators constructed with a tensor product. The repton model presented in Section 3.3 has a compact operator representation, whereas the model for single-layer metal islands presented in Section 3.4 has not. This has a large impact on numerical computations with the matrix methods´(see Chapter 4). The operator representation is a necessity for some computational methods, such as DMRG (see Section 4.1.1 and Appendix A).

As an example, let us consider an open Totally Asymmetric Simple Exclusion Process (TASEP), which is a well-known one-dimensional nonequilibrium particle model with fermionic occupation rules and nearest-neighbor exclusion-type interactions [33]. Particles enter the lattice from the left with the rate α and escape from the right with the rate β, while particles in the bulk have rate 1. See the illustration in Fig. 2.1. For this model, the operators become

[8] For an example of a non-compact representation with null states, see the DMRG topic in Section 4.1.1, where the outer-coordinate representation of the repton model is discussed.

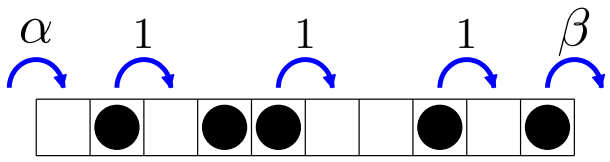

Figure 2.1: An Illustration of the open TASEP model with 10 sites ($L = 10$). For the current configuration, there are five allowed particle transitions available.

$$\begin{aligned} H_{\text{TASEP}} &= \sum_{i=1,L} \left[E(i) - D(i)\right] + \sum_{i=1}^{L-1} \left[E(i,i+1) - D(i,i+1)\right] \\ &= \alpha \left(a_1^\dagger - n_1^0\right) + \beta \left(a_L - n_L^1\right) + \sum_{i=1}^{L-1} \left[a_i a_{i+1}^\dagger - n_i^1 n_{i+1}^0\right], \end{aligned}$$

where L is the length of the lattice, operators a_i and $a_i^\dagger$ annihilate and create a particle at the lattice site i, and n_i^0 and n_i^1 are the occupation operators corresponding to an occupied (1) and empty (0) site. The operators are of the form $X_j := \left[\prod_{i=1}^{j-1} \mathbb{1}_2 \otimes\right] X \left[\prod_{i=j+1}^{L} \otimes \mathbb{1}_2\right]$, where the operator X has dimension 2×2. Note that the dimension of the local operators does not correspond to the dimensionality of the lattice. For example, if the particle exclusion restriction of the TASEP model is lifted, the system become a zero-range process, for which the dimension of local operators is infinite (*i.e.* the number of particles at a site is unlimited).

Random processes in discrete time

For some applications, such as simulations, it is more natural and easy to consider random processes in discrete time. Dealing with discrete-time process is usually easier both theoretically and numerically. We now consider the connection between continuous and discrete-time Markov chains. For a more comprehensive discussion of the subject, we refer to [129, 177].

Consider a finite-state discrete stochastic system whose time-development is given by

$$P_y(t+1) = \sum_{y' \neq y} W_{y,y'}(t) P_{y'}(t),$$

where $W_{y,y'}(t)$ is the probability for a transition from y' to y at time t, and $\sum_i W_{i,j}(t) = 1$ for all j.[9] This type of a process, in which a step only depends on the previous step, is known as a Markov chain. Using the matrix form, this can be written as $P(t+1) = W(t)P(t)$. The operator $W(t)$ is then called a transfer matrix or a stochastic matrix.

[9]Since time is used here only for 'bookkeeping', any positive increment instead of 1 can be chosen

Given a continuous-time Markov process defined by a stochastic generator H, one can easily construct a corresponding discrete-time process with matrix W by re-scaling the elements of H such that

$$W_{i,j} = \begin{cases} H_{i,j} / \sum_k H_{k,j} & \text{if } i \neq j \\ 0 & \text{if } i = j \text{ or } H_{i,j} = 0. \end{cases}$$

The sequences produced by the discrete-time process W have the same probability distribution as those produced by H. Also, since W is just a re-scaled version of H, they both produce the same steady state. The waiting times between transitions are determined by the exponential distribution with the corresponding rates being the diagonal elements of H (*i.e.* total escape rates). Knowing both the sequence and the waiting times between transitions, gives the paths of the process H. This is indeed how continuous-time Monte Carlo method operates (see Section 5.3). To construct a matrix W with a chosen time-step $\Delta t > 0$, there exists unique time-development operator such that $W = \exp\left(\int_{s=0}^{t} H(s)ds\right)$.[10]

Going another way around, *i.e.* from a general W to H, is not meaningful, since the discrete process W may not have a continuous-time representation and even if it has, W already contains more information than H. Also, if the process W has a continuous-time representation, it does not need to be Markovian. Therefore, by simply taking a matrix logarithm of an arbitrary W produces a matrix with both positive and negative complex elements.[11] However, if W has no self-loops, *i.e.* its diagonal values are zero, we can formally create H in the following way. Consider a discrete-time process given by a transition matrix $\widehat{W} = \epsilon W + (1-\epsilon)\mathbb{1}$, where $0 < \epsilon < 1$. Such process is known as a *lazy random walk*, because for small ϵ it has a large probability to stay in the current state. The time-evolution of this process is given by $P(t+\epsilon) = \widehat{W}P(t)$. At the limit $\epsilon \to 0$ this gives $dP(t)/dt = (W - \mathbb{1})\,P(t)$, where $W - \mathbb{1}$ is a continuous-time Markovian random process with the same steady state. However, the time-evolution of this process is not equivalent to that of the discrete time process W for which the time-step is not infinitesimal.

Despite the close mathematical similarity, there is a fundamental difference between continuous and discrete-time random processes. With a discrete-time process, one can even model a completely deterministic motion, whereas master equations always model a random process. In many situations, the discrete-time process is more suitable, such as in studies of machines, games, queues, internet and traffic [145, 81]. Since the number of transitions is always precisely known for the discrete-time system, study of transition paths becomes much easier.[12]

[10] Note that for time-dependent H, operators must retain the proper ordering, *i.e.* $\exp(H_1)\exp(H_2) = \exp(H_2)\exp(H_1) = \exp(H_1 + H_2)$ only if H_1 and H_2 commute.

[11] For a logarithm to produce a valid H, matrix W must have additional properties, see *e.g.* Ref. [39]

[12] For example, see Ref. [51], where fluctuation theorems are studied using a discrete-time model.

Sequences of the discrete process

Let us consider a system described by Eq. (2.5) with time-independent rates. From Eq. (2.4) we find that the probability for a system to remain in a given state x at times $[0,t]$ and then jump into a next reachable state y between time $[t,t+dt]$ is[13]

$$P(y',t|y,0)dt = H_{y',y}\exp(-tK_y)dt,$$

where $H_{y',y}$ is the transition rate and $K_y := \sum_{y'\neq y} H_{y',y}$ is the total escape rate from the state y.

Now consider n subsequent transitions at times $t_1 < t_2 < \cdots < t_n$. Such time-dependent transition series are called paths or trajectories. The path without time-stamps is called a sequence. When given an initial state $x(0)$ at time $t=0$ and time $T>0$, there are two distributions related to a sequence occurring within the time-window $[0,T]$: (1) the probability $f\left[x_1,x_2,\ldots,x_n|x_0,T\right]$ that a path is completed in time $t_n \leq T$ such that the system stays in a final state x_n for a time $T-t_n$ and (2) the probability density $g\left[x_1,x_2,\ldots,x_n|x_0,T\right]$ that a path is completed exactly in a given time T without waiting at the final state, *i.e.* the final transition to state x_n occurs exactly at T. Denoting $k_i := H_{x_i,x_{i-1}}$ and $K_i := \sum_{j\neq i} H_{x_j,x_{i-1}}$, the latter of these distributions can be derived [179, 161] and it is given by

$$g\left[x_1,x_2,\ldots,x_n|x_0,T\right] = k_1k_2\ldots k_n \sum_{i=1}^{n'} \frac{(-1)^{r_i-1}}{(r_i-1)!}\frac{\partial^{r_i-1}}{\partial K_i^{r_i-1}}\left[\frac{e^{-K_iT}}{\prod_{j\neq i}(K_j-K_i)^{r_j}}\right],$$

where n' is the number of distinct escape rates and r_i the count for an escape rate K_i, such that $r_i,\ n' \in [1,n]$ and $\sum_i^{n'} r_i = n$. This weight can be also written as $g(t_1+t_2+\cdots+t_n=T)$, which is a probability consisting of n independent random variables. This distribution results from integrating over all transition times t_i with $i=1,2,\ldots,n-1$, which can be done straightforwardly in the Laplace space. Using this result, probability f can be computed by integrating g [179]

$$\begin{aligned} f\left[x_1,x_2,\ldots,x_n|x_0,T\right] &= \int_{s=0}^{T} g\left[x_1,x_2,\ldots,x_n|x_0,s\right] e^{-K_{n+1}(T-s)}ds \\ &= k_1k_2\ldots k_n \sum_{i=1}^{\tilde{n}} \frac{(-1)^{r_i-1}}{(r_i-1)!}\frac{\partial^{r_i-1}}{\partial K_i^{r_i-1}}\left[\frac{e^{-K_iT}}{\prod_{j\neq i}(K_j-K_i)^{r_j}}\right], \end{aligned}$$

where $r_i,\ \tilde{n} \in [1,n+1]$, *i.e.* the summation now includes also the escape rate K_{n+1} of the final state. The exponential function contributes to the waiting time at the final state x_n until T.

[13] $P(y',t|y,0)dt = H_{y',y}dt\left[1-K_yt/n+o(t/n)\right]^n = H_{y',y}dt\exp\left(\sum_{k=0}^{n-1}\left[-K_yt/n+o(t/n)\right]\right)$, now let $n\to\infty$.

As an example, let us consider the homogeneous Poisson process for which $k \equiv K_i$ for all i, and $x_i = i$ is the number of discrete events. We have then $n' = 1$ and $r_1 = n$ and, by using the equation above, we get

$$g\left[x_1, x_2, \ldots, x_n | x_0, T\right] = \frac{k^n T^{n-1} e^{-kT}}{(n-1)!},$$

which is a well-known Erlang distribution. For the probability f we then get

$$f\left[x_1, x_2, \ldots, x_n | x_0, T\right] = \int_{s=0}^{T} \frac{k^n s^{n-1} e^{-ks}}{(n-1)!} e^{-k(T-s)} ds = \frac{k^n T^n e^{-kT}}{n!}.$$

Now let us consider cycles (*i.e.* $x_n = x_0$) in a general Markov process. The weight of a cycle should include three aspects: (1) The probability to be in some of the cycle states (a starting point), (2) the probability for a complete cycle to occur, and (3) the expected time for the completion of the cycle. Because of the Markov property, these probabilities are independent of each other and the result is a product of the three. The mean waiting time for a cycle is given by $\int_{s=0}^{\infty} s g\left[x_1, x_2, \ldots, x_n | x_0, s\right] ds$, which is simply the sum of the individual waiting times $\sum_{i=1}^{n} 1/K_i$. Although this result is intuitively evident, it is not straightforward to see from a complicated formula of g, which requires ordering of the terms. This means that there is no need to compute g (or f) to find mean cycle completion time. The probability to be in one of the cycle states is simply $P_{x_1} + P_{x_2} + \cdots + P_{x_n}$. Clearly the cycle probability remains the same despite the starting point of the cycle. Finally the probability that the cycle is completed is given by $\prod_{i=1}^{n} k_i/K_i$, *i.e.* at each state the process must pick the correct transition over others. With these three combined, we define a cycle weight

$$w(C) = \frac{\left(\sum_{i \in C} P_i\right) \prod_{i \in C} \frac{k_i}{K_i}}{\sum_{i \in C} \frac{1}{K_i}} = \frac{\left(\sum_{i \in C} P_i\right) \prod_{i \in C} k_i}{\sum_{i \in C} \prod_{j \in C, j \neq i} K_j}. \tag{2.8}$$

The dimension of this weight is inverse of time, so it could be called a cycle rate. This weight defines a type of a measure that one can use to compare cycles. For example, by multiplying $w(C)$ with a total center-of-mass displacement during the cycle, one receives a new weight corresponding to average transport velocity over the cycle. For nonequilibrium systems, $w(C)$ depends on the direction of the cycle and the ratio $w(C)/w(\overline{C}) = \prod_{i \in C} k_i/\overline{k}_i$, where $\overline{k}_i$ indicates the corresponding inverse rates for the inverse cycle $\overline{C}$, differs from the unity. Using this cycle weight, one may compare cycles and, more importantly, find the ones that correspond to the largest (or smallest) cycle weight.

3 Models

In this Chapter, we describe the observables and models on which we shall concentrate in this Thesis. We start by defining the underlying lattice and the types of the potential. After this, the observables of interest are defined. Finally, the models for linear polymers and single-layer atomic islands are defined.

3.1 External potentials

In order to study long-time center-of-mass transport, models studied in this work are placed on infinite one or two dimensional lattices. Without loss of generality, we fix the lattice constant (*i.e.* the spacing between nearest-neighbor sites) to 1. For a periodic potential, it is equivalent to study a model confined in a single period of the potential and apply periodic boundary conditions. For a one dimensional periodic potential, this means $V(x+L) = V(x)$, where $L > 0$ is the *spatial period*. In higher dimensions there, might be several period lengths depending on the potential and the geometry of the lattice. The stochastic generator H only needs to include potential states within a single period. If the potential is homogeneous in space (*e.g.* only external fields exists), one can take $L = 1$.

The assumption of infinite lattice is a good approximation for real systems if the medium is much larger than the period length and the size of the moving object of interest. This is indeed the case with most microscopic systems, where the moving objects are in molecular or atomic scale. Then one can limit the study to steady states of the periodic systems and neglect boundary effects.[1] This approximation is essential to keep the size of the state space of the system reasonable. Therefore in majority of theoretical studies of transport in microscopic systems, such as Brownian/molecular motors and the ratchet effect, periodic boundary conditions are assumed [148].

In this work, we consider two types of external potentials: (1) non-homogeneous potentials that are periodic in space and time, for which we apply notation $V(x,t)$, and (2) spatially homogeneous time-dependent fields, which we denote by $E(t)$. For V, we consider flashing and traveling potentials (see Section 2.1.4), and for E, we consider both static and time-dependent potentials. Potentials are temporally varied by

[1] However, boundary effects are important when studying transport in two and three dimensions with confined space, such as tubes [2].

switching cyclically between two different potentials. This switching process is either instantaneous or smooth in time. We shall consider both stochastic and deterministic switching in the instantaneous case.

3.1.1 Deterministically time-dependent potentials

When the temporal variation of the potential is periodically deterministic, the generator has the property $H(t) = H(t+\tau)$, where $\tau > 0$ is the temporal period. For the special case of instant switching, rates $H_{y',y}(t)$ are piecewise constant functions in time and the stochastic generator is given by

$$H_{y,y'}(t) = \begin{cases} H^1_{y,y'}\,, & t \in [0, \tau_1) \\ H^2_{y,y'}\,, & t \in [\tau_1, \tau_1 + \tau_2) \\ \quad\vdots & \\ H^S_{y,y'}\,, & t \in \left[\sum_{s=1}^{S-1} \tau_s, \tau\right), \end{cases} \tag{3.1}$$

where, for $s = 1, \ldots, S$, the matrix H^s is the time-independent stochastic generator in the potential V_s (all having the same spatial period) and the lifetime of the potential is τ_s, with the total period being $\tau = \sum_{s=1}^{S} \tau_s$. This type of potential switching, where the order of the potentials is fixed, is called cyclic (*i.e.* $V_1 \to V_2 \to \ldots V_S \to V_1$). In this work, we call these instantaneous types of time-dependent potentials as *deterministic potentials* (in Article II these are known as *Type 2* potentials). A special case of this is the on-off potential with $S = 2$, $V_2 \equiv 0$ and $V_1 \neq 0$, which is the working principle of the flashing ratchet defined in Section 2.1.4.

In addition to non-continuous switching, we also consider the following smoothly varying potential $V(x,t) = V_1(x,t)\sin^2(\pi t/\tau) + (1 - \sin^2(\pi t/\tau))V_2(x,t)$. In this scheme, potentials V_1 and V_2 alternate smoothly and symmetrically, such that the time averaged potential is simply $(V_1 + V_2)/2$. We call this a *smoothly varying potential* (in Article II this is known as *Type 3* potential).

3.1.2 Stochastically time-dependent potentials

Instead of periods τ_i being fixed for the instant switching scheme (3.1), they could also be random variables. If the distribution of random periods τ_i is not an exponential distribution, *i.e.* switching is non-Markovian, the time-evolution is governed by a generalized master equation [96], which includes memory-effects and is hard to solve even numerically. For Markovian switching, *i.e.* when the waiting time distribution is exponential, potentials can be directly included into the master equations without

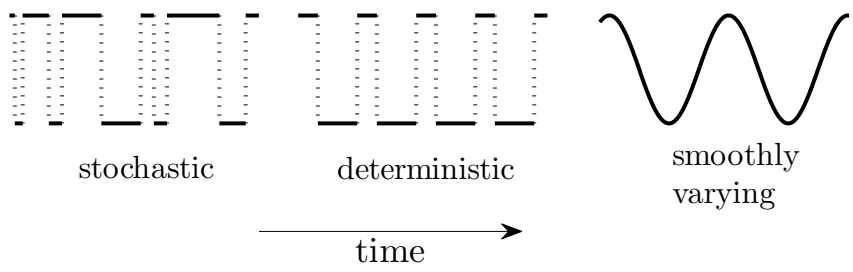

Figure 3.1: An illustration of the time-evolution of $\max_x [V(x,t)]$ for three types of potentials in the case $S = 2$.

need for generalized master equations. Then the problem turns into solving an augmented set of master equations for the probabilities $P_{y,s}(t)$, where s is the state of the potential. The augmented stochastic generator H remains independent of time and the system is directly solvable via solving the eigenstate corresponding to the steady state (see Section 2.2.3). In addition to being computationally easy to handle, Markovian switching is a good approximation for many naturally occurring potentials. For example, the ATP-ADP energy cycle in cells is essentially Markovian. Because of these properties, Markovian time-dependent potentials are applied in majority of the ratchet effect studies [148]. In this work, we shall call potentials with Markov type temporal periods and instantaneous switching, as *stochastic potentials* (in Article II these are known as *Type 1* potentials).

For the Markov type cyclic switching, the augmented stochastic generator corresponding to the deterministic one in Eq. (3.1) is

$$\frac{dP_{s,y}(t)}{dt} = \sum_{y' \neq y} \left[H^s_{y,y'} P_{s,y'}(t) - H^s_{y',y} P_{s,y}(t) \right] + \frac{1}{\tau_{s-1}} P_{s-1,y}(t) - \frac{1}{\tau_s} P_{s,y}(t),$$

where τ_s is the expected lifetime for a potential s, and the periodicity $\tau_0 = \tau_S$ is applied. Since the time periods are random, one may expect that the average response of the system as a function of τ becomes smoother, because of mixing of time-scales. When compared to deterministic potential, there is more variation in paths, which requires more iterations when determining expectation values with the Monte Carlo method. See Fig. 3.1 for an illustration of all three time-dependency schemes for the case $S = 2$.

3.1.3 Simple limits of the temporal period

When studying time-dependent potentials, it is useful to first consider simple limits of the temporal period τ. Let us first consider the case $\tau \to 0$, such that $\tau_i > 0$ for all

$1 \leq i \leq S$. In this case, the very rapidly changing potential becomes an effective *mean-field potential*, and the dynamics is generated by the mean-field stochastic generator $\widehat{H}$. For deterministic potentials that vary smoothly in time, the mean-field operator has elements

$$\widehat{H}_{y',y} = \frac{1}{\tau}\int_0^\tau H_{y',y}(t)dt.$$

For instantaneous type deterministic and stochastic potentials, elements reduces into $\widehat{H}_{y',y} = \sum_s \tau_i H^s_{y',y}/\tau$, where τ_i/τ's are the weight factors. Long-time expected values can be computed using the steady state of the generator $\widehat{H}$. Although this limit is mathematically well defined, from the physical point of view it is artificial, because for real systems, there is a finite response time for changing the potential state (*e.g.* charge re-distribution to build up an electric field) and for an object to respond (*e.g.* inertia). If these effect are taken into account, it means that no net transport is expected to occur at the limit of very fast switching.

Now assume that τ is very large.[2] For instantaneous type deterministic and stochastic potentials, the system converges (arbitrary close) towards the steady state, before the potential is switched again (*e.g.* 'on' or 'off' for a flashing ratchet), and the time spend in the transient state becomes negligible. For smoothly varying potentials, the system remains very close to equilibrium at all times. The expected values of observables approach their adiabatic values, that, for smoothly varying potentials, are computed with

$$\langle O\rangle = \frac{1}{\tau}\int_0^\tau \langle O(t)\rangle_{\rm ss} dt,$$

where $\langle O(t)\rangle_{\rm ss}$ is computed using the steady state of the operator $H(t)$. For instantaneous type deterministic and stochastic potentials, the computation again reduces into $\langle O\rangle = \sum_s \tau_s \langle O\rangle_s/\tau$, where $\langle O\rangle_s$ is the expected value of the measurement operator computed in the steady state of the generator H^s.

When it comes to transport, the special interest lies in the situation with non-zero net transport for finite values of τ, while it disappears at $\tau \to \infty$. For instantaneous type deterministic and stochastic potentials, the transport for large τ is then governed by the relaxation behavior occurring at the switching of the potential. Let $d_{j,i}$ denote the expected travel distance of the center-of-mass within the potential j, using the steady state of the potential i as an initial state and then letting the system fully relax. For cyclic switching, summing over all $d_{j,i}$'s then gives the total expected travel distance within one complete period τ. Travel distance during one cycle is given by $d = \sum_{i=1}^S d_{i,i+1}$. Because of the finite relaxation times for all real systems, d can be already computed by considering time-scales of the order of the largest relaxation times in the system. Therefore, for very slow switching, the velocity can be approximated by the adiabatic velocity $v_{\rm ad} = d/\tau$. For complex systems, even the sign of $v_{\rm ad}$ is

[2]For instantaneous type deterministic and stochastic potentials, also all τ_s's for $s = 1, \ldots, S$ are assumed large separately. If ratios τ_s/τ's are kept fixed, this will inevitably happen when τ gets large.

generally unknown beforehand. This is often the situation when studying the ratchet effect and will be studied further in Chapter 6. For a smoothly varying potential, the situation is somewhat more complicated, since the potential is constantly changing. If one assumes that the system remains all the time arbitrary close to equilibrium, the velocity is always zero and so one also gets $d = 0$. However, for certain types of potentials, there exists so called reversible transport and one can obtain a non-zero d even while doing the computation at equilibrium [131].

3.2 Observables

In addition to probabilities $P_y(t)$ themselves, the most interesting information lies in different types of observables. In this work, we are mainly interested in transport properties, namely the velocity and diffusion properties. For objects that are deformable (*i.e.* not point-like), such as polymers and atomic islands, other interesting observables are the size and shape of the object.

From theoretical point of view, the two types of observables are different: transport-related observables depend on the paths taken by the stochastic system (*e.g.* the velocity and diffusion) and other observables depend only on the probabilities $P_y(t)$ (*e.g.* shape and size measurements). In addition to transport properties, for example energy consumption and entropy production of the system belong to the first category. Path dependent observables are more complicated to compute, since they cannot be measured directly from probabilities. Probability-dependent observables are easier to compute, but the construction of their measurement operators can still be complicated, especially when using the recursion method (see Section 4.1.1).

3.2.1 Velocity and diffusion coefficient

The transport properties of the object are computed from the time-dependent center-of-mass distance vector $x(t)$. For the steady state, the velocity v and the effective diffusion coefficient D_{eff} are defined as

$$v = \lim_{t\to\infty} \frac{\langle x(t)\rangle}{t}$$
$$D_{\text{eff}} = \frac{1}{2d} \lim_{t\to\infty} \frac{1}{t} \left[\langle x^2(t)\rangle - \langle x(t)\rangle^2\right],$$

where d is the dimension of the system. These definitions are usually applied when using the Monte Carlo method. Derivative forms of the previous are

$$v = \lim_{t\to\infty} \frac{1}{\tau} \int_t^{t+\tau} \frac{d\langle x(s)\rangle}{ds} ds$$
$$D_{\text{eff}} = \frac{1}{2d} \lim_{t\to\infty} \frac{1}{\tau} \int_t^{t+\tau} \left[\frac{d\langle x^2(s)\rangle}{ds} - 2\langle x(s)\rangle \frac{d\langle x(s)\rangle}{ds} \right] ds,$$

which are useful for systems with temporally periodic deterministic potentials, especially when using the master equation method. Equivalence of these two definitions can be easily shown by differentiating the first formulae or using integration by parts to the latter one. In practice, it is enough to take a large enough t such that the steady state is reached within required numerical accuracy. We also define the Peclet number

$$\text{Pe} = \frac{|v\,\ell|}{D_{\text{eff}}},$$

where ℓ is the length scale of interest of the transport, such as the size of the object or the spatial period of the potential. The Peclet number is a dimensionless measure of the transport coherence. For perfectly deterministic transport, one has $D_{\text{eff}} = 0$ and thus the Peclet number diverges, which means that the transport is completely coherent without any fluctuations.

3.2.2 Energetic efficiency

Keeping up a nonequilibrium state requires energy. Especially for non-artificial molecular motors working in the cells, the efficiency is essential because of the limited energy available [11]. It is also an interesting aspect for artificial motors. However, the definition of the efficiency is complicated for microscale systems. In the literature, several kinds of definitions of the efficiency have been proposed for Brownian motors, which are not directly comparable against each other [148, 185, 132, 45, 189, 180]. We are not aware of any work in which several measures of efficiency would have been systematically compared on the same model. Here we adopt the basic thermodynamic definition based on the work done against an opposing force F, *i.e.* the output power of the motor is given by vF, where v is the average velocity. The input power W_{in} comes from externally induced potential state changes, which force the traveling objects in a higher energy state depending on its position with respect to the potential. This approach is different from the other proposed scheme, where the object gains constant amounts of energy by, *e.g.* ATP hydrolysis, regardless of the location. We assume that the energy becomes dissipated into the environment, when the object returns to a lower energy state, *i.e.* this energy is not reduced from the input energy.

For cyclically changing potentials, we define the steady state input power as

$$W_{\text{in}} = \begin{cases} \sum_{s=1}^{S} \sum_y \max\left[0, E_y^{s+1} - E_y^s\right] \tau_s^{-1} P_{s,y} & \text{stochastic} \\ \frac{1}{\tau} \sum_{s=1}^{S} \sum_y \max\left[0, E_y^{s+1} - E_y^s\right] P_y(\sum_{k=1}^{s} \tau_k) & \text{deterministic} \\ \frac{1}{\tau} \sum_y \int_{t=0}^{\tau} \max\left[0, \frac{dE_y(t)}{dt}\right] P_y(t) dt & \text{smoothly varying,} \end{cases}$$

where E_y^s is the total energy of the microstate y in the potential s, and similarly $E_y(t)$ is the total energy at time t. The efficiency is defined by $\eta = vF/W_{\text{in}}$. This definition is applied to compute energetic efficiency of the flashing ratchet transport (see Section 6.5).

It has been found, that some real-life molecular motors can exhibit very large efficiencies, *e.g.* around 60% for Kinesin and up to 90% for F_1-ATP [56]. When compared to these, the efficiency of the flashing ratchet model is very low for single particles (see *e.g.* Ref. [132]), but it can be greatly increased for some many particle systems [169, 190]. Despite the size of the machine, the trade-off must be made between the energetic efficiency and the speed; increasing the first, typically decreases the latter. Indeed, the reversible ratchets that operate near equilibrium exchibit efficiencies near 100% while being extemely slow [131].[3]

Besides the efficiency, we are also interested in the stopping force F_{stop} which, when applied, causes the long time velocity go to zero. The larger F_{stop} is, the stronger the molecular motor is. For example, it has been found in Ref. [54] that for polymers working as Brownian motors in the flashing ratchet, F_{stop} depends on the length of the polymer by increasing as the polymer gets longer.

3.2.3 Shape deformations

For systems containing deformable objects, the observables related to the size and shape may carry interesting information. This is especially true if their shape deformations are directly connected to the transport properties, *i.e.* objects move by changing their size and shape instead of sliding. To compute these observables, some effort must be made to create operators for them, or measure them from the simulations. When using the master equation method, expectation values and their fluctuations can be computed as explained in Section 2.2.3 as these types of observables do not depend on paths. Both steady state and transient expected values are of interest. In Chapters 6 and 7, we study the shape deformations of polymers and atomic islands.

[3]For a reversible ratchet, both v and W_{in} approach zero at the adiabatic limit such that their fraction remains non-zero.

3.2.4 Relaxation time

When a physical system is pushed out from its steady state, it takes some time before the system can return into the steady state. Responses to the perturbations are never immediate. Given two events or measurements of the system temporally close to each other, there is always some amount of correlation between them. The average time required to return back to steady state after perturbation, or to correlations to wear off, is called the *relaxation time*. A system can contain several relaxation times, related to different processes and observables. The longest of these times is called the *leading relaxation time*. Roughly speaking, the leading relaxation time defines the maximum timescale needed for the process to 'forget' its initial state and to become uncorrelated.

For stochastic processes the relaxation time is defined for distributions in the sense how fast they decay, *i.e.* $|P(t) - P_{\mathrm{ss}}| \to 0$, where P_{ss} is the steady state. Especially in mathematics, this is also called *mixing*. For master equations, the relaxation times are given directly by the eigenvalues λ_i of the stochastic generator H (see *e.g.* [113, 117]). This can be seen from the transient solution (2.6). The real parts of λ_i are always negative and the relaxation times are defined by $1/|\mathrm{Re}(\lambda_i)|$. The leading relaxation time is therefore given by the inverse of the largest non-zero eigenvalue, *i.e.* the spectral gap between the first and the second eigenvalue. If H includes both the potential with some spatial length (*i.e.* $L > 1$) and an object with internal states, the relaxation times describe both internal and spatial relaxation.[4]

The leading relaxation time is the property of the master equation set and is independent of the initial state, hence it is not directly related to the relaxation time found in experiments or simulations where one usually measures the relaxation of some macroscopic observables, such as the shape and size of deformable objects [36]. Instead, it is related to the computational effort of finding a steady state using numerical methods, such as integration and iterative eigenstate solvers (see Chapter 5). As the leading relaxation time increases (*i.e.* the second eigenvalue approaches zero), the search for the steady state becomes more time-consuming and error-prone.

3.3 The Rubinstein-Duke model

Reptation theory describes the rheological behavior of linear polymers in conditions where the density of obstacles such as other polymers or pores of the medium is very high. In such conditions only the polymer heads are able to move into previously unoccupied space, thus creating a 'tube' for the polymer to move back and forth.

[4] This situation arises, for example, for the repton model studied in Chapter 6 with periods $L = 3$ and $L = 6$.

The polymer motion under these conditions is called reptation. In the first theoretical study of the reptation in 1970s, de Gennes predicted scaling laws for the dependence on the polymer length L for viscosity (*i.e.* the tube renewal time) scaling as $\sim L^3$ and the diffusion constant scaling as $\sim L^{-2}$ [67]. These assumptions were later confirmed with experimental and computational methods [104, 116]. One of the most notable computational models for reptation was proposed by Rubinstein in 1987 [156]. In his model, the network of obstacles is modeled by a lattice and, by assuming that the correlation length between the polymer segments is smaller than the distance between the lattice sites, the problem can be discretized to a simple particle hopping model. In 1989 Duke extended this model by allowing it to include an external field [55], thus giving birth to the Rubinstein-Duke (RD) model. Soon after this, theoretical research of the model started to flourish. The main interest has been in the scaling of the diffusion coefficient and the relaxation time as a function of polymer size, and also the behavior under static fields (see Ref. [110] for a review of results and models). The original RD model can be easily extended by adding external potentials and modifying the rules. Our aim is to study the RD and its modification in non-homogeneous time-dependent potentials. Technical details and the stochastic generator of the RD model are described next.

3.3.1 The stochastic generator

In the RD model, the polymer is divided into N units, called reptons, which occupy the sites of a regular 1-3 dimensional lattice. The number of reptons that each site can accommodate is unlimited and self-avoidance effects are neglected. Each configuration is projected onto an axis along the diagonal of the unit cell and it is identified by the relative coordinates $y_i = x_{i+1} - x_i$ of neighboring reptons along the chain, where x_i indicates the projected coordinate of the i^{th} repton. The relative coordinates can take three values $y_i \in \{-1, 0, 1\}$ and there are thus in total 3^{N-1} different configurations for a chain with N reptons. See Fig. 3.2 for an illustation of this mapping procedure. When two or more reptons accumulate at the same lattice site, they form part of a stored length, which can then diffuse along the tube. In terms of relative coordinates a segment of stored length corresponds to $y_i = 0$ and therefore allowed moves are interchanges of 0's and 1's, *i.e.* for adjacent reptons $(y_i, y_{i+1}) = (0, \pm 1) \leftrightarrow (\pm 1, 0)$. On the other hand, the end reptons of the chain can stretch $0 \to \pm 1$ or retract $\pm 1 \to 0$ to the site occupied by the neighboring repton. The dimension of the medium (before the projection), enters the RD model by modifying the transition rates of the head reptons. This is the standard RD model.

In order to study the effect of the intrinsic transition rules of the reptons in time-dependent potentials, we will compare the results for the RD model with the results of a non-reptating polymer allowing the breaking of the tube. With the above definition,

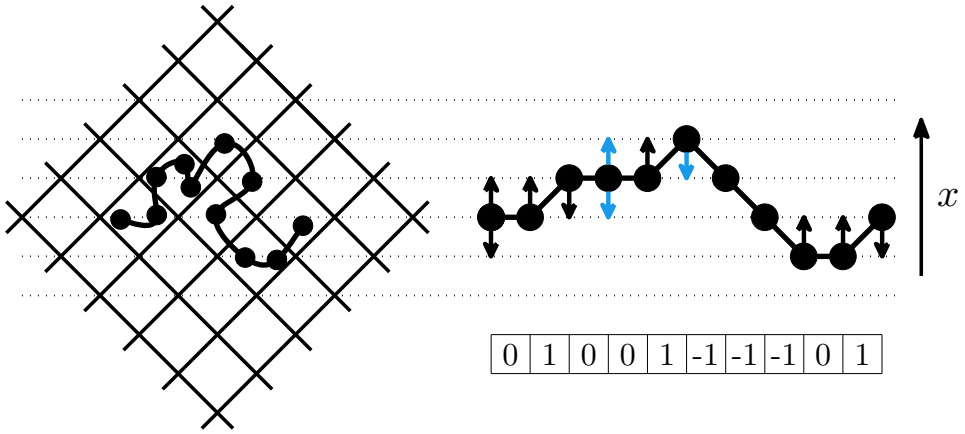

Figure 3.2: An illustration of the Rubinstein-Duke model (right) as a projection of the reptation in two-dimensions (left). In the Rubinstein-Duke model, black arrows indicate reptation moves, whereas the moves with blue arrows are for the relaxed model (see text).

moves with $(0,0) \leftrightarrow (\pm 1, \mp 1)$ are also allowed. We call this relaxed model the *free-motion model* (FM model). Dynamics of the FM model is similar to that of the classical Rouse polymer model, where the polymers are not restricted into tube and can also move freely sideways [154]. In Fig. 3.2, black arrows indicate allowed moves for both models, whereas the moves with blue arrows are only allowed in the FM model. The stochastic generators for the RD and FM models only differ such that there are more non-zero matrix elements for the FM model. Similar types of extensions and modifications of the RD model have been previously studied in different contexts [130, 53, 164]. In this work, we use a generic term *repton model* to include both RD and FM model.

Technically, the repton model is similar to a quantum mechanical open spin-1 chain, which consists of $N-1$ sites with three possible states ($+1$, 0 or -1) and interactions described above. Because of the nearest-neighbor interaction, the repton model has a compact and simple operator representation which enables a recursion method in building of the operators (see Section 4.1.1). Any operator in the repton model can be constructed using local 3×3 sized operators that operate on the individual bonds between reptons (*i.e.* values of y_i). In the space of the complete polymer, these local operators (X) have a tensor product form given by

$$X_i := \left[\prod_{k=1}^{i-1} \mathbb{1}_3 \otimes\right] X \left[\prod_{k=i+1}^{N-1} \otimes \mathbb{1}_3\right],$$

where N is the number of reptons. The dimension of X_i and the stochastic generator

itself is 3^{N-1}. To consider the polymer dynamics in a non-homogeneous medium with the potential $V(x) = V(x + L)$, in addition to the internal state of the potential, also the external state of the potential must be added to all operators. For this purpose, one *marker repton*, which gives the spatial location of the polymer with respect to potential, must be chosen. Although we are free to choose any repton [103], choosing one of the head reptons is most convenient. Choosing the left head repton, all operators then have the form $Y_l \otimes X_i$, where the $L \times L$-sized local operator Y_l works in the state-space of the potential and gives the spatial location. The state of the polymer has the representation

$$|\text{marker repton}\rangle \otimes |\text{polymer configuration}\rangle = |\Phi_l\rangle \otimes |\Psi_y\rangle,$$

where $|\Phi_l\rangle$ has dimension L and $|\Psi_y\rangle$ has dimension 3^{N-1}. The stochastic generator of the repton model in periodic potential can be cast in the form

$$H(t) = \sum_{l=1}^{L} \left[A_l(t) + \sum_y \left(B_{y,l}(t) + \sum_{i=1}^{N-2} M_{i,y,l}(t) \right) \right], \tag{3.2}$$

where the operators A and B are responsible for the dynamics of the heads and the operator M creates the dynamics for the bulk reptons. The reptons are assumed to carry charges which are affected by external potentials. When no external potentials exist, rates for all available transitions are set to 1. Existing external potentials modify the rates according to the Kramers rate theory (see Section 2.2.2). We consider models with both uniform and non-uniform repton charge distributions. The detailed definition of operators and their practical construction are given in Section 4.1.1.

3.3.2 Observables of interest

Properties of the RD model at equilibrium and in static field are well known. At equilibrium (*i.e.* no external potentials), the leading behavior for the diffusion coefficient is $D_N \approx [(2d + 1)N^2]^{-1}$, where d is the dimension of the medium, and for the tube reneval time (the relaxation time) $\tau \propto N^3$. The behavior of τ has been found to be sensitive to dimension d, since lowering d leads to larger exponent for the relaxation [25]. By allowing additional movements to standard RD model, the cross-over from the reptation towards Rouse dynamics with $D_N \propto N^{-1}$ and $\tau \propto N^2$ occur [53]. In large static fields, RD polymers create V-shaped *trap configurations*[5], which causes the velocity to decay exponentially towards zero as the driving field is increased [193, 102]. As the force affecting the polymer depends on the total charge of the polymer, the velocity for large polymers can become decreasing already in small fields. This slowing-down is

[5]Trap configuration are states which require lots of energy to escape from. Without escaping a trap configuration, the transport cannot occur.

a problem for the applicability of experimental techniques such as gel-electrophoresis, which is used to sort the DNA chains according to their length [172]. The phenomenon where polymers with different lengths move equally fast (or slow) in a field, is known as the 'band collapse' and when this occurs, polymers cannot be separated based on their length.

The situation is, however, completely different when the static field is replaced with a time-dependent non-homogeneous potential. The velocity and diffusion properties of such system are very hard to predict because of the complex temporal and spatial interaction between the polymer and the potential. The transport properties are therefore our main interest. Some of the previous work involving polymers and time-dependent fields have shown some interesting properties, such as current inversions [134, 54, 97]. Also experimental research has been conducted by considering separating of DNA by utilizing the ratchet effect [13].

Among other interesting observables are the Peclet number and energetic efficiency of the polymer transport. In order to study the correlation between the shape deformation of the polymer and center-of-mass velocity, we also define the following operators: the *zero-bond count* (number of 0-bonds), the *kink count* (number of $(+1,-1)$ or $(-1,+1)$ bond pairs), the *head-to-head length* (distance $|x_1 - x_N|$ between first and last repton) and the *total length* (maximum distance $\max_{i,j}(x_i - x_j)$ between any two reptons). The corresponding operator definitions and their recursive construction of these observables are found in Section 4.1.1. For example, for the configuration in Fig. 3.2 the values for of these operators would be 3 for zero-bonds, 1 for kinks, 0 for the head-to-head length and 3 for the total length. Separating the head-to-head and the total length is important since it provide a means of distinguishing between linear and bent (such as V and U shaped) conformation of the polymer.

3.3.3 Non-uniform charge distributions

The usual assumption in the studies concerning polymer transport is that the polymer is homogeneous, *i.e.* in discrete models all monomers are identical with the same charge and mass. We shall relax this assumption and study the effect of the non-uniform charges for the repton model. Previous works on the RD model have considered some aspects of this. In Ref. [25], a magnetophoresis model (*i.e.* one charged head repton) was considered, and in Ref. [52], it was shown that when it comes to the velocity, all charge distributions are equivalent in small fields (*i.e.* linear response regime).[6] In Ref. [150], it was noticed that the drift in constant field depends strongly on the posi-

[6]This is clear, since in the linear response regime only the total force affecting the object matter, and the diffusion coefficient is given by the Einstein relation. Similar equivalence does not hold for systems involving non-homogeneous potentials.

tion of the charged repton within the polymer, and in Ref. [102], non-homogeneously charged RD polymers in large fields were studied. A recent study of dimer kinetics in a periodic potential shows that if the connected particles are non-identical, directed drift can be generated even in a symmetric potential [68].

We want to find the optimal charge distributions for the RD and FM polymers which results in the largest possible drifts. The optimal charge distribution can be expected to give some (indirect) information about the polymer conformations and reptons that dominate the transport (*i.e.* have the largest impact on the velocity). Optimization of periodic potentials has been previously considered for single particle systems [18, 49, 199].

3.4 The model for single-layer metal islands

Diffusion of adsorbates is perhaps the most elementary transport process occurring on surfaces [86]. It is crucial for more complex surface phenomena, such as crystal growth, associative desorption, heterogeneous catalysis and chemical reactions. We are interested in the diffusion of metallic atom islands on a smooth surface. In the basic setup, the island consists of single layer of atoms lying on the surface of the bulk material consisting of similar atoms. Atoms move in hopping manner between the minima of the regular surface potential created by the bulk atoms and the island. Equilibrium properties of these type of systems are well known, as well as near-equilibrium properties under small electromigration forces[7] in the linear response regime [5]. Also some properties under strong forces have been studied with continuum models [137]. We are interested in the properties of single-layer atom islands under the effect of strong and time-dependent external forces, in particular, in the behavior of small islands with up to 20 atoms, where the discreteness and finite-size effects are strongly present and etropic effects are not yet dominant. We apply an idealized model of hopping atoms in the square lattice with nearest-neighbor energetics [123]. Technical details and the stochastic generator of this model are described next.

3.4.1 The stochastic generator

The model consists of two-dimensional atom islands on an unbounded square-lattice surface. In this set-up, each atom has up to four nearest and four next-nearest (diagonal) neighbors. To keep the islands unbroken, we require that each atom must be connected to the island with at least one diagonal neighbor. The dynamics is created

[7]Electromigration force is the force caused by collisions between the atoms of the island and field-driven electrons in the bulk.

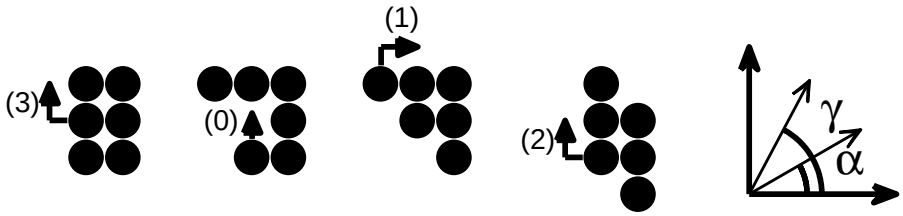

Figure 3.3: An illustration of the model with a 6-atom ($N = 6$) island going through 4 consecutive transitions and used notation for the angles γ and α (see text). Small arrows indicate the transitions and their corresponding values of the $\Delta_{f,i}$ parameter in Eq. (3.3).

by single atom hops in continuous time with rates given by a semi-empirical model parameterized by the embedded atom method [123]. Within this model, the changes in the binding energy for an atomic transition is computed from the change in the nearest neighbor atom count. Despite its simplicity, the energetics given by the model is in good agreement with molecular dynamical computations (see [98] for the most recent results). The transition rate $\Gamma_{i,f}$ from the initial state (i) to the final state (f) is given by

$$\Gamma_{f,i}(t) = \nu \exp\left(\frac{-E_S - \max\{0, E_B\Delta_{f,i}\} + E_{f,i}(t))}{k_{\mathrm{B}}T}\right), \tag{3.3}$$

where ν is an effective vibrational frequency, E_{S} is the energy barrier for the atom transition along the island edge, $E_{\mathrm{B}}\Delta_{f,i}$ ($\Delta_{f,i} = -3, \ldots, 3$) is the change in the binding energy with nearest neighbor bonds, and $E_{f,i}(t)$ gives the time-dependent contribution (positive or negative) to the transition rate by an external electromigration-type force and depends on the magnitudes and directions of the field and atom displacement. The model and its parameters are illustrated in Fig. 3.3.

For Cu on Cu(001) we use $E_{\mathrm{B}} = 0.260$ eV and $E_{\mathrm{S}} = 0.258$ eV [123]. We set ν and the lattice constant to 1. Since the barrier E_{S} appears in all transitions, it can be integrated in the prefactor by defining a new temperature-dependent prefactor $\widetilde{\nu} := \nu \exp(-E_S/k_{\mathrm{B}}T)$. Due to the large separation of energy barriers, there are at temperatures $T < 1000$ K four well-separated microscopic rate parameters in the system in zero field and up to six for large fields ($E \sim E_B$) in the direction of the main axes of the lattice. Depending on the direction of the field, the energetics gets more complicated as demonstrated in Fig. 3.4, where we have plotted all 16 unique rates $\Gamma_{f,i}$ that appear for the case $E > 0$ and $\alpha = 23°$. Although experimentally realizable electromigration forces in most cases are too small (order 10^{-5} eV [122, 153]) to cause significant non-linear effects alone, combined with other methods that can decrease energy barriers, such as strain, manipulation with scanning tunneling microscopy and electric fields [136, 78], non-linear effects are expected to emerge.

Although this simplified model is not microscopically accurate, it captures the key

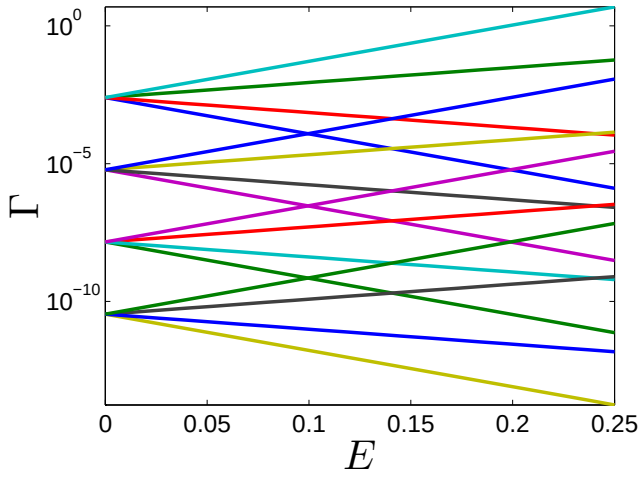

Figure 3.4: Separation of time-scales in terms of possible jump rates Γ for the island model as a function of the field strength at temperature $T = 500$ K for field direction $\alpha = 23°$ (see Fig. 3.3 for the definition of the angle α).

elements of the dynamics, respects the detailed balance condition (for $E_{f,i}(t) \equiv 0$) to avoid spurious currents and is straightforward to apply in computations. We want to apply a simplified model as we do not wish to study only a particular system but rather to investigate properties which should not depend on the finest details of the atom-atom interaction. Therefore, we use a simple kinetic model containing as few parameters as possible. Since experimentally realizable field amplitudes in electromigration are really small, transport properties of non-continuous islands have been previously studied only within the linear-response regime with very small fields ($E < 0.01$ eV).

As the detachment of atoms from the island is forbidden in our model, the number of atoms in the island remains a constant. This is a well-justified approximation for small fields (*i.e.* $E_{f,i} \ll E_B$) and temperatures far below the melting point of the metal (1358 K for Cu). Also, if the density of free surface atoms is such that evaporation and condensation are balanced, the island size could be kept constant on average also with unrestricted dynamics. When the detachment/attachment processes are rare compared to other processes, the properties of the variable size islands follow from those of the fixed size islands, because the island size remains fixed for long periods of time, thus allowing relaxation between events. In such cases, for example the mean velocity of the variable size island under a driving force is a combination of velocities of fixed size islands over a wide time scale. Only when the detachment/attachment processes become very frequent, which necessarily occurs at high temperatures and very strong fields, this commonly used picture of noninteracting islands with different sizes is no longer valid. On the basis of previous studies at (or near) equilibrium

(*e.g.* [167, 80]) and the results of Chapter 7, at least within temperatures below 800 K and $E < 0.1$ eV one can assume that the dynamics is not dominated by the detachment/attachment processes and island transport is mainly controlled by the periphery diffusion.

The velocity of the center-of-mass of the island is given by a vector $\vec{v} = (v_x, v_y)$ and $\vec{x} = (x, y)$ is the center-of-mass position at the surface using the main axes of the lattice. We define the measuring direction by angle γ, *i.e.* we measure $v = v_x \cos(\gamma) + v_y \sin(\gamma)$. The field is defined by the amplitude $E \geq 0$ and the angle α of the field direction, *i.e.* $\vec{E} = (E\cos(\alpha), E\sin(\alpha))$. The effective diffusion coefficient D_{eff} can be computed with a projected distance $x_\gamma = \cos(\gamma)x + \sin(\gamma)y$.

To illustrate atomic transitions and the effect of the field, consider a non-zero field with $\alpha = 90°$ such that $\vec{E} = (0, E)$) in Fig. 3.3. The energy barriers for the four transitions shown are decreased by E and similarly increased for the corresponding inverse transitions. For $\alpha = 45°$, the barrier of transition (1) is decreased by $2E/\sqrt{2}$ and that of transition (0) by $E/\sqrt{2}$. In what we shall call the *Monte Carlo* (MC) *model*, two independent separate jumps are required to go around a corner [processes (1)-(3)], whereas in the *Master Equation* (ME) *model* such transitions occur by direct diagonal jumps.

3.4.2 The reduced model

The number of configurations for two dimensional islands becomes huge even for small number of atoms. To be able to study islands up to $N = 12$, we reduce the number of island configurations by allowing only states that do not include configurations with only diagonally connected atoms or parts of the island. To facilitate going around the corner, which is necessary for long-range transport of the island, we allow direct diagonal jumps like those shown in Fig. 3.3 (numbers (1-3)). In the MC model, going around the corner is possible by two jumps. The energy barrier of the diagonal jump is approximated by a sum of the binding energy difference between the initial and the intermediate state and the energy difference caused by the field. Further reduction was made by disallowing vacancies (i.e. holes) inside the islands, which however only has a minor effect on the number of available states. This way we have defined the ME model.

These approximations cause only minor differences between MC and ME models in equilibrium ($E \equiv 0$), where the weights only depend on the total energy of the configuration, and the islands prefer compact rectangular shapes. For nonequilibrium states, major differences between the models are expected, especially for field amplitudes approaching the binding energy $E \sim E_B$. This is mainly because of the trap configurations and the diagonal jump approximation. The difference between the MC

and ME models depends on how important the corner states are for the dynamics.

The allowed island configurations are known as polyominoes (or lattice animals), and their counting and statistical properties are known at least up to $N < 47$ [90]. Since the practical limit for numerical master equation computations is about 10^6 states, the largest system studied in this work is the 12-atom island with 468837 states (505861 if vacancies are allowed). From now on, we call this reduced model the *ME model*, whereas the full model is called the *MC model*. For a comparison, only up to 8-atom islands could be treated by applying the ME method directly to the full MC model without any above reductions (see Section 4.1.2 for details). The ME model does no have the kind of compact operator representation as the repton model has, therefore we rely on an enumeration method in creating the stochastic generator H and other operators. This is covered in Section 4.1.2.

Neither the numerical master equation nor Monte Carlo method can be applied as such to study properties of the islands at very low temperatures. As the temperature decreases, the difference between the largest and the smallest rate increases, which eventually leads to a very stiff set of linear equations (*i.e.* H is badly scaled). This limits the minimum temperature for practical computations to be around 500 K. When computing the steady state (*i.e.* solve $Hx = 0$), the stability of computations can be somewhat improved by using a diagonal pre-conditioning matrix with entries $1/H_{i,i}$ (this works because H is weakly diagonally dominant). This decreases the lowest reachable temperature to be near 300 K for the velocity. However, this procedure was not generally found to improve computations of the effective diffusion coefficient that requires solving linear equations of the type $Hx = b$ (additional details in Section 4.2.1). In general, reaching low temperatures with stable numerics would require coarse graining techniques to reduce the separation of rates, and it is a possible continuation for this work.[8]

3.4.3 Observables of interest

Equilibrium properties of islands (and also voids) are well known [5, 198, 183, 80]. For example, the center-of-mass diffusion coefficient for large islands is proportional to $e^{-E_{\mathrm{eff}}/k_{\mathrm{B}}T}N^{-\alpha}$, where E_{eff} is an effective Arrhenius barrier and α is a scaling exponent. In most situations the most important diffusion mechanism is the periphery diffusion for which $\alpha = 3/2$ and $E_{\mathrm{eff}} \approx 0.75$ eV have been obtained. For small islands up to 20 atoms or so, many-body effects have a dominating role and there exist strong 'magic size' effects, hence the diffusion coefficient is strongly size dependent. For small driving forces, large islands become deformed and move with an oscillatory fashion

[8] This kind of idea has been applied in Ref. [163], where low temperature coarse graining is carried on by hand for islands $N = 3 \ldots 5$.

[122, 20, 157, 153].

Our main interest lies in the steady state velocity as a function of field direction α, amplitude E and temporal period τ. For time-dependent fields, island transport becomes also frequency dependent. Due to the interplay between island configurations and strong time-dependent forces, one could expect phenomena such as current inversion or increase to appear (see *e.g.* Ref. [134, 3]). Because of the square lattice geometry, the (001) surface is a good candidate for investigating the effects of rotated field, which would be less pronounced for *e.g.* the (111) surfaces. The relationship between transport properties and these parameters has not been systematically studied beyond linear response regime. We are also interested in shape deformations of the islands, such as the average thickness and length in the direction of an axis, the relaxation time and the effective Arrhenius barrier in strong fields.

4 Setting up the equations

In this and the following Chapter, we describe the numerical methods used in this work. The main emphasis is on the direct numerical solution of master equations, but also the Monte Carlo method is discussed. In this Chapter, we cover the construction of master equation sets and derivation of equations related to the observables. Solving these equations is discussed in the following Chapter. Explicit construction of the master equation set is necessary to find a numerical (or algebraic) solution using the linear algebra, whereas in the Monte Carlo method, master equations are formed implicitly during the computation.

4.1 Constructing the master equation sets

The first step of the numerical master equation method is to build and store the equations. Master equations and operators are written by using the sparse matrix representation. For small systems up to a dozen states or so, H can be build manually by hand. For large systems, their construction must be done using a program suitable for the given model. The construction methods basically fall into two categories (or their combination): The brute-force enumeration method and the recursive matrix method. In the brute-force method, all microstates are found (enumerated) and then the matrix H and operators are constructed by finding the allowed transitions between these states. Both of these steps are usually time-consuming and require efficient algorithms to minimize the computational cost. The enumeration method can always be applied, similarly as the Monte Carlo method can always be applied to solve expectation values. The island model requires this type of an approach. The recursive matrix method uses recursive approach by increasing the system size step by step, while building H and operators using efficient matrix operations (namely the multiplication). This method is typically very fast, since most of the computation time is spent doing matrix computations. However, this requires that H and all operators of interest have a compact operator representation (*i.e.* no null states, see Section 2.2.3), which enables enlargement of the system size by recursion. The repton model fulfills this requirement. In the following sections we go through these two approaches in detail for the repton and island models.

Building of large master equation sets of complex systems is an error-prone procedure. Whereas the problems with the numerical methods, such as an incomplete convergence

of eigenstates or numerical inaccuracies, are usually obvious, errors in the matrix H and the operators can be easily missed. Errors such as incorrect rates and transitions between states, *e.g.* if H has too many or few elements, can have a large effect on the transport properties. Therefore a few basic tests should be applied to ensure that the equations are indeed correct. In addition to most obvious tests, including a manual checking for the smallest systems and comparison of results against previously known ones, one should check that (1) the equilibrium distribution indeed has Boltzmann weights, (2) there are no local currents in equilibrium and (3) observables are consistent with respect to symmetries (if present). The detailed balance check is important, since local currents may be present even if the net current is zero. This situation typically arises when the rates are taken directly from incomplete experimental or simulation data, which can result in cycles with non-zero affinities in equilibrium (see Section 2.1.3). The last test applies to models where the parameters and observables have certain symmetry properties. For example, the velocity direction must be reversed when all the potentials are reversed. Also, if the system consists of identical particles, the observables should remain the same for all of them. [1]

4.1.1 Recursive method for the repton model

If the system has a compact operator representation and there is a straightforward way to construct a large system by enlarging the smaller one, one can utilize the recursive method to build H and operators related to the observables. The most typical examples of such systems are one dimensional spin chains (*e.g.* Heisenberg and Hubbard chains) and classical particle models (*e.g.* simple exclusion processes, zero-range process and Ising chain) where only the nearest-neighbor interactions are present. Next we describe in details the recursive method for the repton model, whose stochastic generator was discussed in Section 3.3.1.

The stochastic generator

In the repton model, every bond between reptons can be in three states; up (+1), down (-1) or flat (0). In the following, we shall call these states A, B and $\varnothing$. For these three states, we may introduce the local operators for measurement and changing of the bond state. Following the previous works (see *e.g.* [130]), we use the notation n_A, n_B and $n_\varnothing$ for the bond state measurement operators. Operators a and b are the annihilation operator for states A and B, turning the bond states into state $\varnothing$. Corresponding creation operators, which create bond states A and B from the state $\varnothing$, are $a^\dagger$ and $b^\dagger$. With these operators, the dynamics of the polymer can be defined. In natural basis, we define these operators with matrices with the following non-zero

[1] For example, consider a homogeneous repton model for which the head reptons are identical. Due to this symmetry, all measurements should be now invariant between the heads.

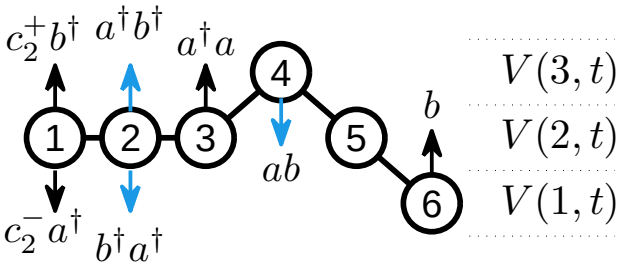

Figure 4.1: Illustration of the allowed transitions in RD (black arrows) and FM (black and blue arrows) models for a six repton polymer in one of its configurations in the potential $V(x,t)$. The letters a, b, c represent the operators corresponding to the moves and are defined in the text.

elements

$$[n_A]_{1,1} = [n_\varnothing]_{2,2} = [n_B]_{3,3} = 1$$
$$[a]_{2,1} = \left[a^\dagger\right]_{1,2} = [b]_{2,3} = \left[b^\dagger\right]_{3,2} = 1.$$

After adding the non-homogeneous periodic potential $V(x) = V(x+L)$ with $L > 1$ and the marker repton, the transition rates of all reptons depend on the position of the marker repton and all other bonds separating it from the marker. In the following, we choose the leftmost head repton as the marker repton. The dimension of the marker state is L, so the dimension of the total system of equations becomes $L \times 3^{N-1}$. For $l = 1, 2, \ldots, L$, the state measurement operator of the marker repton is n_l, and the dynamics is created with operators c_l^+ and c_l^-, which move the marker repton to the next and the previous location on the potential (using periodic boundary conditions, $L+1 \to 1$ and $0 \to L$). For these operators, we apply matrices with the following non-zero elements

$$\left[c_l^-\right]_{l-1,l} = 1 \text{ for } l \neq 1, \quad \left[c_l^+\right]_{l+1,l} = 1 \text{ for } l \neq L$$
$$\left[c_1^-\right]_{L,1} = \left[c_L^+\right]_{1,L} = [n_l]_{l,l} = 1.$$

In Fig. 4.1 we show one configuration of a 6-repton polymer with all allowed moves and their corresponding operators.

Transition rates are denoted by

$$D(q,i) = \exp\left[\left(V(i) - V(i+1)\right) q\right]$$
$$U(q,i) = \exp\left[\left(V(i) - V(i-1)\right) q\right],$$

indicating up (U) and down (D) moves of the reptons (see Fig. 3.2) with charge q. The effect of the field E can be included by adding qE and $-qE$ inside the exponential functions of D and U. We keep temperature fixed, hence the factor $1/k_\mathrm{B}T$ can

be absorbed into V and E. Rates are generally time-dependent, but to ease up to notation, we drop the t-dependency from now on. Using the above definitions, we can now define the following three operators that appear in Eq. (3.2) for the head (A and B) and bulk (M) reptons

$$\begin{aligned}A_l(q) = \{U(q,l) + D(q,l)\}\tilde{n}_{\varnothing,1,l} - U(q,l)\tilde{a}^\dagger_{1,l} - D(q,l)\tilde{b}^\dagger_{1,l} \\ + D(q,l)\tilde{n}_{A,1,l} - D(q,l)\tilde{a}_{1,l} + U(q,l)\tilde{n}_{B,1,l} - U(q,l)\tilde{b}_{1,l}\end{aligned}$$

$$\begin{aligned}B_{y,l}(q) = \{U(q,l+f(N-1,y)) + D(q,l+f(N-1,y))\}n_{\varnothing,N-1,y,l} \\ - U(q,l+f(N-1,y))a^\dagger_{N-1,y,l} - D(q,l+f(N-1,y))b^\dagger_{N-1,y,l} \\ + D(q,l+f(N-1,y))n_{A,N-1,y,l} - D(q,l+f(N-1,y))a_{N-1,y,l} \\ + U(q,l+f(N-1,y))n_{B,N-1,y,l} - U(q,l+f(N-1,y))b_{N-1,y,l}\end{aligned}$$

$$\begin{aligned}M_{i,y,l}(q) = U(q,l+f(i,y))(n_{A,i,y,l}n_{\varnothing,i+1,y,l}+n_{\varnothing,i,y,l}n_{B,i+1,y,l}-a_{i,y,l}a^\dagger_{i+1,y,l}-b^\dagger_{i,y,l}b_{i+1,y,l}) \\ + D(q,l+f(i,y))(n_{\varnothing,i,y,l}n_{A,i+1,y,l} + n_{B,i,y,l}n_{\varnothing,i+1,y,l} - a^\dagger_{i,y,l}a_{i+1,y,l} - b_{i,y,l}b^\dagger_{i+1,y,l}) \\ + \Omega U(q,l+f(i,y))(n_{A,i,y,l}n_{B,i+1,y,l} + n_{\varnothing,i,y,l}n_{\varnothing,i+1,y,l} - a_{i,y,l}b_{i+1,y,l} - b^\dagger_{i,y,l}a^\dagger_{i+1,y,l}) \\ + \Omega D(q,l+f(i,y))(n_{B,i,y,l}n_{A,i+1,y,l} + n_{\varnothing,i,y,l}n_{\varnothing,i+1,y,l} - b_{i,y,l}a_{i+1,y,l} - a^\dagger_{i,y,l}b^\dagger_{i+1,y,l}),\end{aligned}$$

where $\Omega = 0$ defines the standard Rubinstein-Duke repton model and $\Omega = 1$ defines the free motion model, and

$$\begin{aligned}\tilde{a}_{1,l} &= c_l^+ a_1 \quad \tilde{a}^\dagger_{1,l} = c_l^- a^\dagger_1 \\ \tilde{b}_{1,l} &= c_l^- b_1 \quad \tilde{b}^\dagger_{1,l} = c_l^+ b^\dagger_1 \\ \tilde{n}_{z,1,l} &= n_l n_{z,1} \\ x_{i,y,l} &= n_l \left(\prod_{j=1}^{i-1} n_{g(y,j),j}\right) x_i \\ n_{z,i,y,l} &= n_l \left(\prod_{j=1}^{i-1} n_{g(y,j),j}\right) n_{z,i}\end{aligned}$$

with $x \in \{a, b, a^\dagger, b^\dagger\}$, $z \in \{A, \varnothing, B\}$. The function $g(y,i) \in \{A, \varnothing, B\}$ gives the state of the i^{th} bond in the configuration y, and the function f

$$f(i,y) = \sum_{j=1}^{i} \langle \Psi_y | n_{A,i} - n_{B,i} | \Psi_y \rangle, \quad 1 \le i \le N-1 \tag{4.1}$$

gives the position of the repton $i+1$ in marker-centered coordinates. Here $|\Psi_y\rangle$ is the configuration vector for the state y (see Section 3.3.1), and in natural basis, it has

only one non-zero element. The detailed forms of the functions g and f depend on the selection of the state basis. In efficient recursive construction method, reptons can be added only such way that the new repton replaces the old marker repton (*i.e.* in Fig. 4.1 new reptons must be added on the left of repton labeled 1).

Macrostate operators

In this work we are interested in macrostate operator that measure the head-to-head length, the total length, and the number of number of zero-bonds and kinks. Macrostate operators are formed from (large) sets of microstates that correspond to the same value of the macrostate (*e.g.* there are many microstates corresponding to the same total length of the polymer). Using the notation above, the formal definitions for these observables for the N repton polymer are

$$\begin{aligned}
&y \in F^Z_{n_z} : \#\left\{1 \leq i < N; g(y,i) = \varnothing\right\} = n_z, \\
&y \in F^K_{n_k} : \#\left\{1 \leq i < N-1; g(y,i) = \mathrm{A/B} \wedge g(y,i+1) = \mathrm{B/A}\right\} = n_k, \\
&y \in F^H_{n_h} : |f(N-1,y)| = n_h, \\
&y \in F^G_{n_g} : \max_{k,l} \left[f(k,y) - f(l,y)\right] = n_g,\ k,l = 1,2,\ldots,N-1\,,
\end{aligned}$$

where $n_z, n_h, n_g = 0, 1, \ldots, N-1$ and $n_k = 0, 1, \ldots, N-2$. Put in words, the set $F^Z_{n_z}$ contains all such polymer configurations that contain n_z bond states of type $\varnothing$. The set $F^K_{n_k}$ contains all configurations that have n_k kinks in them. The set $F^H_{n_h}$ and $F^G_{n_g}$ contain all such configurations with head-to-head length n_h and total length n_g. Since the total length also includes the head-to-head length, one can verify that $\#F^G_i \geq \#F^H_i$ holds for all i. By using sets F and Eq. (2.7), the operators can be constructed and expected values of measured observables computed. The practical procedure to form operators is explained below.

Since the stochastic generator and the measurement operators used in this work are more complex than in the previous works on the RD model, we show in some detail the idea of the recursive operator construction in the current case. Let $\left\{O^i_1, \ldots, O^i_{n_i}\right\}$ be a set of macrostate operators and let $\left\{\omega^i_1, \ldots, \omega^i_{n_i}\right\}$ be some weights associated with them for a system with i sites. Operators for observables are then constructed as $O^i = \sum_{n=1}^{n_i} \omega_n O^i_n$. We assume that the set includes all the necessary operators that are required when adding a new site. Here *site* is a general term, which for example could mean single particle states for classical systems and spin states for quantum systems. Let us assume that the new sites are added on the right such that $|\text{new state}\rangle = |\text{old state}\rangle \otimes |\text{new site}\rangle$. The basic algorithm to add new sites (until N) goes as follows

1. Build an initial set of operator(s) O^1_n, where $n = 1, \ldots, n_1$.
2. For all $m = 2, 3, \ldots, N$ and $n = 1, \ldots, n_m$, build:

$$O_n^m = \sum_{(k,j)=K(n_{m-1},n)} O_k^{m-1} \otimes \widehat{n}_j$$

3. Build the full operator $O^N = \sum_{n=1}^{n_N} \omega_n O_n^N$,

where n_m is the total number of operator required for the size m system. The details, of how to construct a new set of state operators for the enlarged system by joining the states of the new site and the old operators, are hidden in the function $K(n_{m-1}, n)$ that determines the summation process. The complexity of this function and the number n_m of the required operators depends on the type of the operator. Practically it is the n_m that determines the computational effort needed to build large operators, since K is just a 'bookkeeping' function.

We next concentrate on the repton model for which *sites* mean bond states between the reptons. With some effort, one can determine n_m for the macrostate operators, and the results are as follows

- Zero-bonds: $n_m = m + 1$ (number of zero-bonds)
- Kinks: $n_m = \max[3, 3(m-1)]$ (number of kinks and state of the rightmost bond)
- Head-to-head length: $n_m = 2m + 1$ (signed distance between the heads)
- Total length: $n_m = (1-k)(3k-2m-7) \geq (1+m)(3+m)/3$, where $k = \left\lceil \frac{m+4}{3} \right\rceil$ (see example below)

The number of required operators is therefore $\propto m^2$ for the total length and $\propto m$ for others.

We now consider a concrete example for a total length operator, which is the most complex operator used in this paper. When one enlarges the size of this operator with new particles, one must keep track of the maximum distances of the rightmost repton from all the other reptons both above *and* below it. For example, in Fig. 4.1 these distances would be 2 (from repton no. 4) and 0 (no reptons below the rightmost repton). We define these as *up* (u) and *down* (d) distances, respectively. Total distance is then $d + u$.

In Fig. 4.2 we show all 9 microstates of the 3-repton polymer. Since there are five combinations for u and d distances, the macrostate operators $O^2_{(2,0)}, O^2_{(0,2)}, \ldots, O^2_{(0,1)}$ are formed with each of them including one or more microstates. This is shown in the figure with red numbers in the (d, u)-plane. When a new repton is added, a function K is used to combine old macrostate operators with state operators of

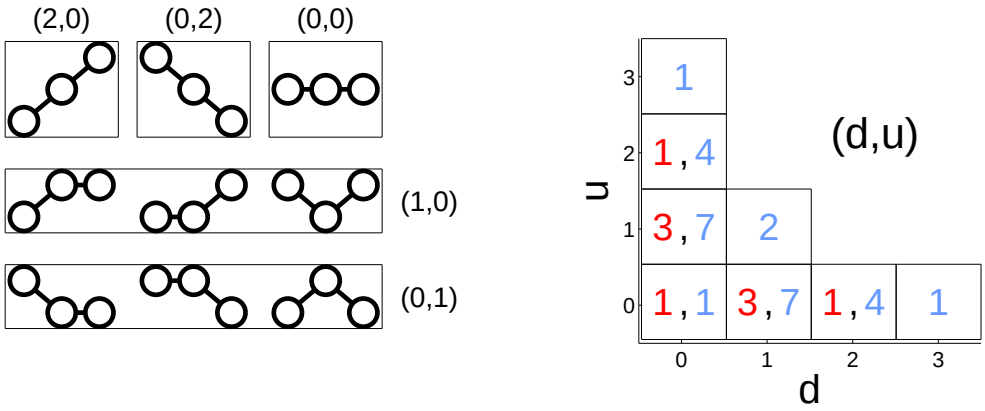

Figure 4.2: All 9 configurations (microstates) of the 3-repton polymer with 5 macrostate operators that are formed from them. The macrostates are indexed by the corresponding (d, u). As a new particle is added, there are new (d, u) combinations available and the number of macrostates is increased by three. The relation between the microstates and macrostates is illustrated in the (d, u)-plane, where the red (gray) and blue (light gray) numbers indicate the number of microstates for 3 and 4 repton polymers.

the new site ($\{n_A, n_\varnothing, n_B\}$), and hence the number of macrostate operators is increased by three. Examples of the required operations includes $O^3_{(2,0)} = O^2_{(1,0)} \otimes n_A$ and $O^3_{(1,1)} = O^2_{(2,0)} \otimes n_B$. After addition, there are 27 microstates in eight macrostate operators (blue numbers in the figure). Note that in the actual computations only the information about the d and u values is needed. Here the tracking of the microstates was done for illustration purposes only. As more reptons are added, the 'triangle' that presents available (d, u) states gets larger.

DMRG method for the repton model

For the models of the recursive type, there exists a computational method known as the Density Matrix Renormalization Group (DMRG) that can be applied to extend the master equation method to very large system sizes. The DMRG method was proposed by White in 1992 in his seminal paper [195] as a method to study large one-dimensional strongly correlated quantum mechanical systems. In the years that followed, this method was further developed and used in numerous studies. Most commonly DMRG is used to study one-dimensional quantum systems, such as Heisenberg and Hubbard models. With small modification, it can be also applied to classical stochastic models and it has been applied to study the RD model and simple exclusion processes [25, 130, 70]. In previous works of the RD model, only the case with a static field has been considered. In the following, we describe how to apply the DMRG method for the repton model including a periodic external potential. The universal parts of the DMRG method, which are not directly model-dependent, are described

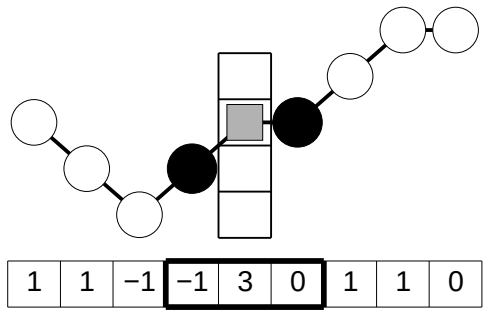

Figure 4.3: An illustration of the system structure used in the DMRG computations in the case of 9-repton polymer in the potential with $L = 4$. White reptons belong into the two reduced blocks, while the the reptons with black spheres remain unreduced. The repton marked with a gray rectangle, is the marker repton and it also remains unreduced. The position of the marker repton changes during sweeping.

in Appendix A.[2]

In our implementation, the construction of the repton model is illustrated in Fig. 4.3 for the case $N = 9$ and $L = 4$. The total system is constructed from the left, right and middle parts. Left and right parts (the reptons marked with spheres) contain the chain of the bond states (three possible states for each bond) starting from the middle 'marker' repton (the repton marked with a gray square), which has L possible states. For the left part, the bond state indicates the repton position compared to the nearest-neighbor repton at the right hand side, and for the right part it is the repton at the left hand side. This construction allows adding new reptons (*i.e.* bonds) at both sides of the marker repton (the repton marker with gray spheres). These new bonds are truncated in the DMRG procedure. The marker repton is added only when the stochastic generator of the complete system is needed, and it is never truncated.

When compared to the case with only a static field, inclusion of the non-homogeneous potential creates some complications. Since the state of the marker repton is not reduced, the dimension of the stochastic generator is increased by a factor L. One must also store L times more operators for the reduced left and right parts. In the extended model, a transition rate of the repton depends on the state of the marker repton and all other bonds between the repton and the marker (governed by the function f defined in Eq. (4.1)). The standard DMRG method is not designed for this type of situation, hence it is generally unclear how this affects to the computational cost and accuracy of the method. Also, the velocity and position along the potential

[2]For those who are not familiar with the DMRG method, I suggest reading the appendix before continuing.

can be only measured for the marker repton.[3]

After testing different constructions, potential types and parameters, we found that the symmetric block structure above leads to best results. For example, including the marker repton state in left or right block (or both), and truncating it, was found to produce very inaccurate results. In addition to above inner coordinate representation based on the bond states, we also considered the *outer coordinate representation* with the actual repton positions (*i.e.* all reptons are marker reptons). However, such representation is compact only for the case $L = 3$. For $L > 3$, there will be lots of null states related to the non-allowed polymer configurations (broken polymers), which makes this representation very inefficient because of the additional work needed to get rid off the null states during the computation. Also, the two-term interaction of the inner coordinate representation becomes three-term interaction when using outer coordinates. For the special case $L = 3$, this representation however was found to be somewhat more efficient in the DMRG computations by allowing more efficient truncation (smaller matrices).

To study time-dependent potential, one must either do numerical integration (deterministic and smoothly varying potentials) or add an additional potential state in the stochastic generator (stochastic potential). In our first effort, we tried the latter one, which turns the problem into solving the steady state using the time-independent DMRG method. We tried adding the potential state in various positions of the system, including the the edges and the middle. We also tried both truncating it or leaving it non-truncated, similar to the marker repton. Unfortunately, none of these approaches were successful due to the numerical inaccuracies and instabilities. Adding the potential state increases the dimension of the system and creates a complex global interaction, which was found to increase the computational cost beyond the practical limit. In our second approach, we used deterministic and smoothly varying potentials, for which the potential state is not included in the stochastic generator (see Section 3.1.1), but instead one uses time-dependent DMRG method to do numerical integration in time. This method was found to work quite well. However, since the integration is computationally very expensive, we were unable to reach the periodic steady state of large systems, and hence were forced to limit our studies into studying the relaxation process only. The results of these studies are presented in Section 6.2.

4.1.2 Enumeration method for the island model

If the system has no simple operator representation or short interaction distance, the recursive method cannot be applied to construct the stochastic generator and

[3]Since the polymer is unbroken, long-time transport properties do not depend on whether one measures directly the center-of-mass location (all reptons) or just one repton.

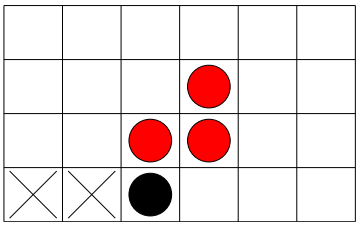

Figure 4.4: Enumeration lattice for a size 4 polyominoes (*i.e.* no corner connections). The site filled with a black sphere is always filled, whereas positions of red spheres visit every allowed configuration. Sites marked with crosses cannot be filled.

operators of interest. In such cases, a brute force type enumeration must be applied. In this method, all possible configurations are enumerated, which for large systems needs an efficient algorithm. Similarly as in the recursive case, typically such algorithm starts with a few particles and then the number of particles is increased until the given limit. An efficient algorithm only produces a new configuration with each iteration, never repeating the previous ones. For the reduced island model (see Section 3.4.2), the compact operator representation is not known and we apply enumeration method.

As explained in Section 3.4.2, island configurations in the reduced model are polyominoes. An efficient brute-force enumeration method for polyominoes was introduced by Redelmeier [147]. In this method, an enumeration lattice, as illustrated in Fig. 4.4 for the case $N = 4$, is used. One starts with a single filled site in a fixed position at the bottom of the lattice and fill other sites using the nearest neighbors. By keeping track of the previously filled sites, one can go through all possible combinations efficiently. Although the original algorithm only applies to configurations with only nearest neighbor connections (*i.e.* no corner connections), the next-nearest neighbor sites can be included by a minor modification of the original algorithm. The total number of island configurations, with and without holes and corner connections, is shown in Table 4.1 for islands up to 10 and 12 atoms. Since the maximum number of configurations is around 10^6 states for the numerical master equation method, states with corner connections must be omitted in order to study islands up to 12 atoms. Note that, if a stochastic type time-dependent potential is used, the dimension of the matrix is increased by a factor S (see Section 3.1.2). After the enumeration, the building of the stochastic generator and measurement operators begins. For this we use configuration projections.

The construction process of the stochastic generator and measurement operators consists of the following steps:

1. Enumerate all states using Redelmeier's method. For each state, save projections and other information required by measurement operators.

Table 4.1: Number of island configuration as a function of the atom count.

	with corners		no corners	
N	all	solid	all	solid
2	4	4	2	2
3	20	20	6	6
4	110	109	19	19
5	638	622	63	63
6	3832	3664	216	216
7	23592	22094	760	756
8	147941	135609	2725	2684
9	940982	843941	9910	9638
10	6053180	5310754	35446	34930
11	-	-	135268	127560
12	-	-	505861	468837

2. Construct the stochastic generator by comparing projections based on possible nearest-neighbor transitions

3. Determine reaction classes and measurement related information for transitions. Discard all illegal transitions that may occur.

4. Construct final matrices by substituting values, such as reaction rates Γ.

After the enumeration (step 1), elements of the stochastic generators are found by finding all allowed transitions between the configurations (step 2). This is the most time-consuming part of the computations, as in the general case, it scales as a square of the total number of states (comparing all configurations against each other). However, for the island model we can take advantage of that only single atom transitions are allowed (for general transitions, some pattern recognition algorithm would be required). Therefore we sort the states by their projection along coordinate axes and their diagonals, which greatly reduces the number of states that need to be compared against each other. See Fig. 4.5 for an illustration of the projections. After this, transitions can be classified by their reaction classes (see Section 3.4.1) and also measurement information computed (if not already done within step 1). We ended up with matrices that include rate classes and other information such as displacements (step 3). Steps 2 and 3 could be also done simultaneously. Resulting matrices are stored. Before numerically solving the master equations, the final matrix is created by putting the actual rates into the matrix (step 4). This final step is fast, since the matrices are very sparse. In principle, all parts of the matrix computations can be parallelized, for example by dividing the matrices in smaller parts.

Finally, we note that although the reduced island model has no compact operator representation, one can apply recursive method to count the number of different con-

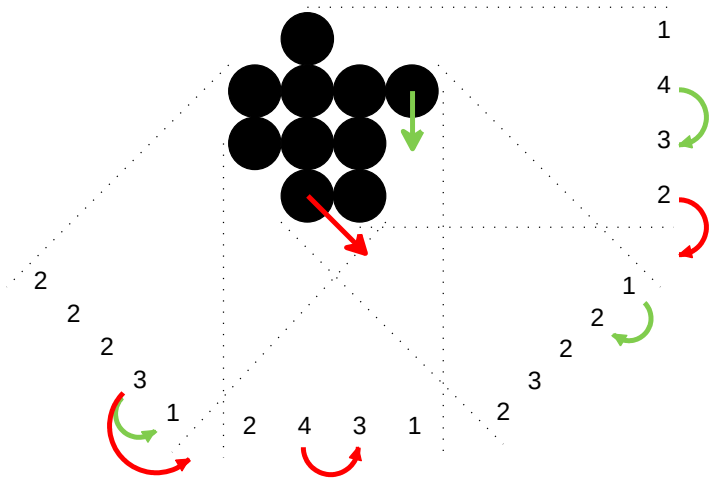

Figure 4.5: Four projections of a single island configuration with two example transitions for the reduced island model.

figurations. For this purpose, a transfer matrix method has been developed [90]. Similar method has been also used to count self-avoiding random walks. However, this method is very complicated and it cannot be directly applied to actually construct a stochastic generator. As we only need to enumerate states with no more than 12 atoms, the brute force method is fast enough for our needs.

At the end of this subsection, to get some idea of the structure of the stochastic generators for the repton and island models, in Fig. 4.6(a), we show the average number of transitions (edges) from a state (vertex), and in Fig. 4.6(b), the total dimension of H as a function of the number of reptons and atoms. For both models, we consider generators with internal configurations only, *i.e.* $L = S = 1$ (see Section 3.1). While the total number of states grows exponentially, the average number of allowed transitions for a state grows only linearly, being less than 12 even for the largest systems. Although the repton and the reduced island models correspond to very different types of physical systems, their H matrices have quite a similar structure. We found that their numerical properties are also quite similar when it comes to solving numerical linear algebra and integration problems, which most likely results from the similar structure of the matrices.

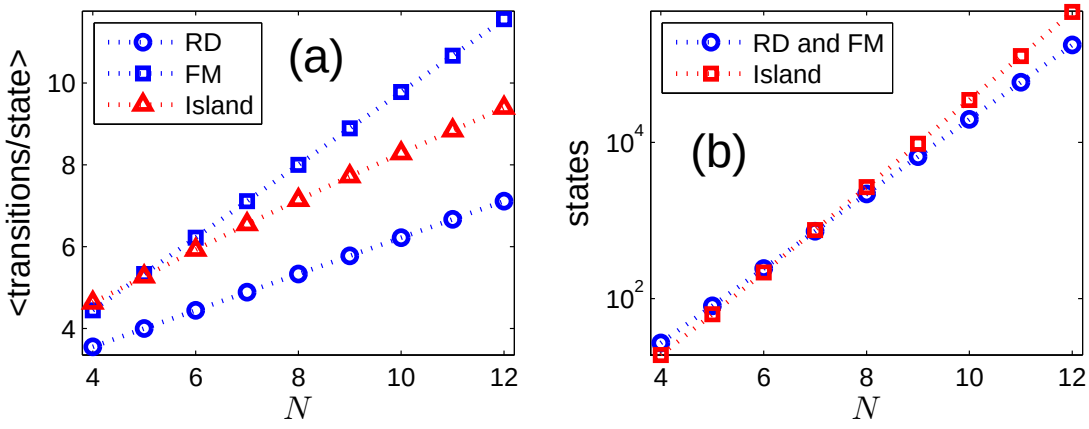

Figure 4.6: (a) Average number of transitions per state and (b) total number of states for the repton (including both the RD and FM model) and the reduced island model as a function of the number of reptons and atoms.

4.2 Expected values of path-dependent observables

As noted in Section 2.2.3, computing expected values of observables with an operator representation is straightforward. Unfortunately, many interesting observables do not have such representation, or at least it is not apparent because they depend on the paths of the stochastic process. The most important examples of such observables are the velocity v and the effective diffusion constant D_{eff}. In this Section, we describe how such observables can be computed.

To receive a more general picture, it is convenient to introduce the concept of a *counting process*. The counting process is a real valued stochastic process whose time-evolution is governed by another stochastic process, which in our case is a process defined by the stochastic generator H. The physical scenario described by a counting process is the measurement of some quantity by adding its increments whenever the underlying transition, that is associated with the increment, occurs. The required assumption is, that the measurement does not perturb the dynamics of the original process on which the measurement is performed. These two conditions define a counting process [76, 57]. In the case of v and D_{eff}, the counting process is the position of the center-of-mass.[4]

In the following, we derive the equations that can be solved numerically to find v and D_{eff}, but these techniques also work for other similar type of counting processes. Computation can be done either directly or using generating functions, leading to

[4]If the system is two or three dimensional, we consider the projected position of the center-of-mass along the chosen direction.

slightly different types of equations.

4.2.1 Direct method

In 1983, Derrida derived the analytical closed-form solution for the random walk in a periodic one-dimensional lattice with arbitrary rates [46]. Since then, the same methodology has been used to solve other simple random walk models. Although closed form expressions for the velocity and the diffusion coefficient can be computed only for simple systems, the technique can be applied to any system numerically. A similar methodology has also been used in the context of solving Fokker-Planck equations by discretization [188].

Let us consider a stochastic generator H and a counting process $x(t)$ defined by increments of an anti-symmetric matrix D, *i.e.* for all $H_{y,y'}$ the corresponding increment is $D_{y,y'}$, and if $H_{y,y'} = 0$, also the increment is zero. Now, it is possible that there are two (or even more) different $D_{y,y'}$ for a non-zero transition $H_{y,y'}$ when $y \neq y'$. In such case, one must either distinguish these different branches, *i.e.* work with tensors $D^i_{y,y'}$ and $H^i_{y,y'}$, or expand the state space such that branching disappears. For example, when studying center-of-mass transport, one may simply increase the period length L. Although the latter method makes the state space larger, it is often much more practical. Branching does not typically occur for complex particles systems, including the repton and island models, and especially when the number of configurations is large[5]. From now on, we will therefore assume that there is no branching or it has been eliminated.

In the case of transport properties, counter $x(t)$ is the position of the center-of-mass and $D_{y,y'}$ is the displacement in the chosen direction. By using the definitions given in Chapter 3.2.1, one then arrives into equations

$$v(t) = \sum_{y'} \sum_{y} D_{y',y} H_{y',y}(t) q_y(t) \tag{4.2}$$

$$D_{\text{eff}}(t) = \sum_{y} \sum_{y'} D_{y',y} H_{y',y}(t) s_y(t) + \frac{1}{2} \sum_{y} \sum_{y'} D^2_{y',y} H_{y',y}(t) q_y(t), \tag{4.3}$$

where s and q are auxiliary functions such that $\sum_y q_y = 1$ and $\sum_y s_y = 0$. The derivation of these equations is straightforward and is given in Appendix A.2. The

[5]For a simple example of branching, consider a single particle ASEP model with two sites ($L = 2$) and periodic boundary conditions. For the displacement counter, the total number of transitions between the two states is four, because there are always two possible directions for a particle to jump. This branching disappears with $L = 3$.

time-evolution of s and q is given by

$$\frac{dq_y(t)}{dt} = \sum_{y'} [H_{y,y'}(t)q_{y'}(t) - H_{y',y}(t)q_y(t)]$$
$$\frac{ds_y(t)}{dt} = \sum_{y'} [H_{y,y'}(t)s_{y'}(t) - H_{y',y}(t)s_y(t) + H_{y,y'}(t)D_{y,y'}q_{y'}(t)] - v(t)q_y(t).$$

In the matrix form, these can be written as

$$\begin{aligned} v(t) &= \langle 1|D \circ H(t)|q(t)\rangle \\ D_{\text{eff}}(t) &= \langle 1|D \circ H(t)|s(t)\rangle + \frac{1}{2}\langle 1|(D \circ D) \circ H(t)|q(t)\rangle, \\ \frac{d|q(t)\rangle}{dt} &= H(t)|q(t)\rangle \\ \frac{d|s(t)\rangle}{dt} &= H(t)|s(t)\rangle - D \circ H(t)|q(t)\rangle - v(t)|q(t)\rangle, \end{aligned}$$

where $\circ$ is the entry-wise matrix product. Since $s(t)$ depends on $v(t)$, vectors $q(t)$ and $s(t)$ must be solved simultaneously.

In the case of time-independent H, in the steady state with $\lim_{t\to\infty} q(t) = Q$ and $\lim_{t\to\infty} s(t) = S$, the derivatives become zero and the computation of v and D_{eff} require solving two linear problems

$$\begin{aligned} 0 &= H|Q\rangle \\ 0 &= H|S\rangle - D \circ H|Q\rangle - v|Q\rangle, \end{aligned}$$

where the first one is an eigenvalue problem, giving Q and the steady state velocity v. Using these, S can be then computed from the second linear problem. Because of the eigenvalue zero, the matrix H can be multiplied from the left with any pre-conditioning matrix, which can make the numerical solution easier. Note that pre-conditioning is possible only for the eigenvalue zero and cannot be applied, for example, when computing relaxation constants.

4.2.2 Generating function method

Instead of applying above direct method, one can also apply generating functions. This proves very useful especially for time-independent systems and this approach is applied widely in theoretical research of nonequilibrium systems [8, 47, 76]. As before, we consider the counting process $x(t)$ with increments $D_{y,y'}$. We now define a joint-distribution $P_y(x,t)$ for the system to be in state y and the counting process having

value x at time t. The normalization of $P_y(x,t)$ is given by

$$\sum_x P_y(x,t) = P_y(t) \qquad\qquad \sum_y P_y(t) = 1.$$

For this extended distribution, we define set of master equations

$$\frac{dP_y(x,t)}{dt} = \sum_{y' \neq y} \left[H_{y,y'} P_{y'}(x + D_{y,y'}, t) - H_{y',y} P_y(x,t) \right].$$

By summing over x, one recovers the original master equation. Let us now introduce the moment generating function for x,

$$F_y(\lambda, t) = \sum_x e^{\lambda x} P_y(x,t).$$

The moments of x are then given by

$$\langle x(t)^n \rangle = \frac{d}{d\lambda^n} \sum_y F_y(\lambda, t)|_{\lambda=0}.$$

Using the identity $\sum_z \sum_x e^{\lambda x} P_y(x+z,t) = \sum_z e^{\lambda z} F_y(\lambda,t)$ and the extended master equations, the time-development of F is

$$\begin{aligned}
\frac{dF_y(\lambda,t)}{dt} &= \sum_x e^{\lambda x} \sum_{y' \neq y} \left[H_{y,y'} P_{y'}(x + D_{y,y'}, t) - H_{y',y} P_y(x,t) \right] \\
&= \sum_{y' \neq y} \left[H_{y,y'} e^{-\lambda D_{y,y'}} \sum_x e^{\lambda (x + D_{y,y'})} P_{y'}(x + D_{y,y'}, t) - H_{y',y} \sum_x e^{\lambda x} P_y(x,t) \right] \\
&= \sum_{y' \neq y} \left[H_{y,y'} e^{-\lambda D_{y,y'}} F_{y'}(\lambda,t) - H_{y',y} F_y(\lambda,t) \right].
\end{aligned}$$

This can be expressed in the matrix form $dF_\lambda(t)/dt = H_\lambda(t) F_\lambda(t)$, where H_λ is called a modified or a twisted generating function. The largest eigenvalue of H_λ, for which we use notation $\Delta(\lambda)$, is now positive for all $\lambda \neq 0$ and therefore the norm of F is an increasing function of time. This can cause serious problems for numerical integration if λ and integration time are large. Instead of numerical integration, one can solve Laplace transformed $F_\lambda(s)$, which however requires taking a computationally expensive numerical inverse transform.

Let us now consider the time-independent H_λ. In this case, the long-time behavior of $F(\lambda,t)$ is dominated by $\Delta(\lambda)$ and we can approximate

$$\langle e^{\lambda x} \rangle = \sum_y F_y(x,t) \sim e^{t\Delta(\lambda)}.$$

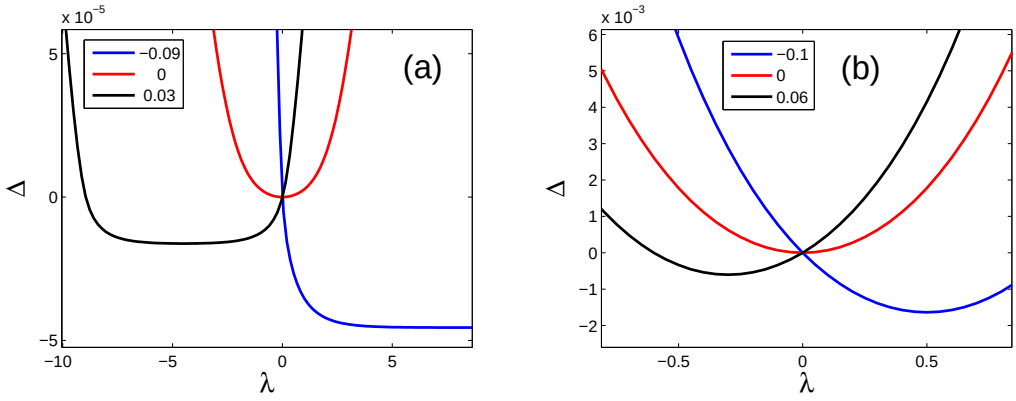

Figure 4.7: The largest eigenvalue Δ of the modified stochastic generator H_λ for (a) 9-atom reduced island model and (b) 10-repton RD model as a function of parameter λ for various static field amplitudes E. For the island model $\gamma = \alpha = 0°$ for the measurement and field directions and $T = 700$ K.

The initial state becomes negligible for large t. The long-time limits of cumulants can now be computed by differentiating Δ. First two moments are

$$\lim_{t\to\infty} \frac{1}{t}\langle x\rangle = \left.\frac{d\Delta(\lambda)}{d\lambda}\right|_{\lambda=0}$$
$$\lim_{t\to\infty} \frac{1}{t}\left[\langle x^2\rangle - \langle x\rangle^2\right] = \left.\frac{d^2\Delta(\lambda)}{d\lambda^2}\right|_{\lambda=0}.$$

For D being the displacement matrix for the center-of-mass, these are v and D_{eff}. Alternative derivations using direct Fourier transforms can be also used [181]. This approach turns out to be especially useful in solving simple systems analytically (see *e.g.* [163, 64]).

When compared to the direct method, computing the steady state velocity and the effective diffusion coefficient for a time-independent system is straightforward, since there is no need to solve a linear problem. However, this requires computation of several eigenvalues of H_λ using different λ's around $\lambda = 0$ and taking numerical derivatives. Also no pre-conditioning can be applied since eigenvalues are generally non-zero for all but $\lambda = 0$.

To demonstrate how the function $\Delta(\lambda)$ looks like near $\lambda = 0$ for a center-of-mass transport, in Fig. 4.7 we have plotted $\Delta(\lambda)$ for the (a) 9-atom reduced island model and (b) 10-repton RD model using three different field amplitudes E. The shape of the Δ curves correspond to the complexity between the rates and displacements. For the repton model, the field affects similarly for all rates, whereas for the island model the effect of the field depends also on the values of $D_{y,y'}$ (also the rates are more complicated).

Apart from the numerical issues, the main difference between the direct and the generating function method is that the latter provides all cumulants of the counting process, not just the first (*e.g.* v) and the second (*e.g.* D_{eff}). Although not very useful when studying only transport, higher cumulants might become useful for some systems, for example, when studying phase transitions (*e.g.* see a study of the TASEP model in Ref. [70]). However, because of numerical issues, we have found the direct method numerically more feasible in most cases. Finally, as noted in Section 2.1.2, one can also apply the linear response theory to compute D_{eff} at equilibrium. This involves computation of v in small static fields and doing a linear fit. Although this method does not allow determination of D_{eff} beyond the linear response, it can be used for a simple checking of the results given by the two methods or simulations.

5 Computational methods

In this Chapter, we consider the numerical methods to solve equations described in Section 4.2 and do numerical optimization over the model parameters and sequences, and we also describe the Monte Carlo method.

Since only handful of nonequilibrium systems can be solved analytically, numerical methods are essential in studying these systems. Typical exactly solvable models in statistical mechanics are one-dimensional and simple, examples being simple exclusion processes (including TASEP), the Potts model and the Ising model [119, 101, 178]. To solve master equations that cannot be solved analytically, there are three approaches depending on the number of equations (in parenthesis): The symbolic method (up to $\sim$10), the numerical method (up to $\sim 10^6$) and the numerical approximative Monte Carlo method (all sizes). For the first two, the limits are somewhat model dependent as some systems are much easier to solve than others. In the symbolic method, functional expression for the probability distribution and observables are found for example using software such as MATHEMATICA and MAPLE. Even for systems with a few master equations and parameters, the resulting expressions are usually lengthy and complicated, but a thorough analysis is them possible (*e.g.* see [163, 89, 162, 163, 175, 193]). As the number of equations gets beyond 10 or so, this approach becomes impossible due to computational cost. In the latter part of this Chapter, we concentrate on the last two approaches.

For small and medium sized systems, numerical solution of the master equations is possible. Although functional forms are unknown, numerical values for the probability distribution and observables can be computed, typically with a high floating point precision. In this work, we call this approach the *numerical master equation method*. This method also allows one to do numerical optimization with respect to cycles and continuous parameters, as we will see in this Chapter. The practical upper limit for the number of equations depends on the details of the model, such as how far the system is from equilibrium, and on the topology of the transition graph. Using current desktop computers and standard numerical and optimization methods, we have found that the practical upper limit of equations for the master equation method is roughly around 10^6. For larger systems, the computational cost (time and memory requirement) rapidly increases, thus making the method impractical. Since the computational complexity of methods in numerical linear algebra and graph analysis typically increases very rapidly as a function of the system size, simply increasing the computational power cannot push this upper limit much further. To study much

larger systems with the numerical master equation method, approximate methods, such as DMRG, must be applied.

For the Monte Carlo method, there is no upper limit for the number of equations, because master equations are not explicitly constructed. It can, in principle, be used for systems of arbitrary complexity. The upper limit for the systems size is set by the required accuracy, since increasing the system size usually leads to larger statistical error and increased computational cost. Since the numerical results obtained with the Monte Carlo method typically contain significant statistical error even for small systems, the accuracy is much worse compared to the numerical master equation method. This can make studying of certain elusive properties, such as drifts caused by the ratchet effect, and optimization practically impossible. The Monte Carlo method is discussed further at the end of this Chapter.

There is currently a large number of different numerical methods for each type of problem that is encountered when using the numerical master equation method. As discussed in Chapter 2, there are several fundamental differences between equilibrium and nonequilibrium systems. Similarly there are differences in how these systems can be solved numerically, especially when it comes to linear algebra. It is often impossible to know beforehand which method works best for a given model and parameters, hence testing of different methods is important when studying large systems. In this Chapter, in addition to summarizing the available methods, we also compare some of them for the repton and island models.

All data analysis and most of the computations in this work were done within MATLAB, either by using the scripting language with MEX-extensions [1] or using MATLAB only as a front-end for executables written in C++ and Java. Most numerical methods that we apply are built-in in MATLAB or are available via official Toolboxes. All computations in this Thesis were carried on with mid-range desktop PCs available in 2008-2011. Computation times vary from seconds to several days, depending on the problem type and the number of master equations. For example, solving steady states for the smallest systems (8 particles or less) takes only a few seconds, while numerical integration via DMRG of large systems can take weeks.

[1] MEX functions are compiled binaries that can be executed directly using the MATLAB environment.

5.1 Numerical linear algebra and integration methods

Now we turn into numerical solution methods of the equations appearing in Section 4.2. When studying steady states, the method of choice depends on whether the system is explicitly time-dependent or not. For a time-independent system (*i.e.* elements of H are constant), the problem is reduced to an eigenstate and linear problems, whereas in the general case, numerical integration is required. Unfortunately, since the stochastic generators of master equations represent a group of very different types of matrices, there are no tricks or methods that could make the numerical computations significantly easier. Only if the system has some additional properties, such as H having weakly connected components or a special structure (*e.g.* tridiagonal), some special techniques become available [63]. However, since this does not apply to most stochastic generators, or even those models studied in this work, we do not make any additional assumptions on the stochastic generator at this point.

5.1.1 Solving eigenstates and linear problems

It has become evident that to solve the steady state distribution, the leading relaxation time and fluctuations of path-dependent observables, one needs to solve eigenvalue and linear problems or integrate in time. For the eigenvalues and eigenstates, we only need those two corresponding to the smallest eigenvalues. The two linear algebraic problems are defined by $Ax = \lambda x$ and $Ax = b$, where x and b are vectors, A is a real square matrix and eigenvalue λ is real or complex. Since the first problem is equivalent to solving roots of high-order polynomials, only iterative solving methods can be applied. For the linear problem, the selection of methods is much broader and there are both direct and iterative methods. Direct solvers are typically designed for dense matrices and they work by factorizing the matrix into a product of simpler matrices whose inverse is easy to find (namely using the LU decomposition).[2] Both of these methodologies has its advantages. Direct methods tend to be generic, robust, predictable and efficient. But their scalability is limited as they require lots of memory and become too slow for large matrices. Iterative methods scale much better and require less memory, but are usually more fragile, less robust and, for the very small problems, slower than direct methods. For very large systems, direct methods are generally unusable, and we therefore concentrate on the iterative methods. In the following, we summarize the most important iterative methods in linear algebra. A more comprehensive listing and details of the methods can be found in many textbooks, such as [17, 71, 159, 160]. We

[2]Direct methods can be also applied for sparse matrices, but because this requires additional steps for re-ordering of matrix elements and determining suitable data structures, it is not usually efficient. See *e.g.* Ref. [43] for more details.

start by defining the Krylov subspace, which is the key concept behind almost every iterative method today.

Krylov subspace

Given a matrix A and a non-zero seed vector v, a *Krylov subspace* is defined by

$$K_k(A, v) = \text{span}(v, Av, A^2v, \ldots, A^{k-1}v),$$

where k is the size (dimension) of the subspace. Algorithms that operate, one way or another, on Krylov subspaces are called *Krylov subspace methods* and they are among the most advanced methods currently available. In these methods, instead of working with original matrices, the problem is projected on the Krylov subspace which results in significantly smaller matrices. As the problem size is reduced, one may apply direct methods, such as QR factorization[3], for solving eigenvalues and linear equation solvers to solve sub-problems.

Because the vectors A^iv are non-orthogonal and become linearly dependent when $k > n$, and also because the corresponding basis set of K_k tends to become badly conditioned for large k, methods relying on Krylov subspace frequently involve some orthogonalization scheme. For nonsymmetric matrices, this has lead to development of the Arnoldi iteration method, which can be used to construct an orthogonal basis for K_k. Krylov subspace methods usually have good convergence properties for extremal eigenvalues, a good numerical stability and the required storage space for algorithms is small [158].

Iterative solution of eigenvalues

The working principle of eigenvalue solvers is based on the power iteration. Starting at the random vector x_0, iteration of the form $x_1 = Ax_0, x_2 = Ax_1, \ldots$ converges towards the eigenstate with the largest absolute magnitude. Similarly, iteration with a shifted and inverted matrix $(A - \sigma I)^{-1}$ converges towards the eigenstate with the eigenvalue closest to σ of the original problem. However, this requires either solving the inverse matrix or a linear problem $(A - \sigma I)x_{i+1} = x_i$ at each iteration. The full spectrum of A can be solved iteratively using QR iteration. For large and sparse matrices these methods are however too inefficient and hence the Krylov subspace methods are used [160].

With the *Arnoldi iteration*, an orthonormal basis $v_1, v_2, \ldots, v_k$ can be constructed for $K_k(A, x_0)$ such that $V_k^T A V_k = H_k$, where the column vectors of V_k contain the basis and H_k is a Hessenberg matrix. Eigenvalues and states of H_k are known as *Ritz eigenvalues* and *Ritz states*. A number of the Ritz eigenvalues, typically a small fraction

[3]For a real matrix A, QR factorization is defined by $A = QR$, where Q is orthogonal and R an upper triangular matrix.

of k, will usually constitute good approximations of the corresponding eigenvalues of A and the quality of the approximation will usually improve as k increases. However, the number of iteration steps is unpredictable and can be very high with the basic Arnoldi algorithm. In 1992, Sorensen introduced the *implicitly restarted Arnoldi method* (IRAM) [176], which limits the dimension of the search space while maintaining the structure of the Krylov subspace. In this algorithm, one starts with k steps of Arnoldi iteration and then repeats the following four steps until convergence [112]: (1) sort Ritz eigenvalues into *wanted* and *unwanted* sets with sizes m and q (*i.e.* $k = m + q$), (2) do implicitly shifted QR iteration corresponding to unwanted eigenvalues, (3) reduce the Krylov subspace using polynomial filtering (the new dimension is m), (4) do q steps of Arnoldi iteration.

The computational complexity of IRAM depends on the structure and spectrum of matrix H (dimension N) and the choice of parameters k, m and q. With a naive analysis of the IRAM algorithm, the total number of floating point operations for a single IRAM step is $(c_N q + 10mp - 4q + 4q^2 + 2m^2)\,N + O(k^3)$, where c_N is the coefficient for a single matrix-vector multiplication [17]. For dense matrices $c_N = N$ and for sparse matrices c_N is a constant (much smaller than N), or a slowly increasing function of N. The overall complexity of the method is, however, unknown. IRAM can be considered as the state-of-the-art method to solve large nonsymmetric eigenvalue problems. Through ARPACK library, it is a part of many scientific computing applications, including MATLAB.[4]

Iterative solution of linear problems

Solving a linear system iteratively is somewhat more involved than solving eigenvalues and there are several different types of methods available. For weakly diagonally dominant matrices, it is known that the solution for $Ax = b$ can be found by simple iterative methods such as Gauss-Seidel and Jacobi methods [87]. However, for these type of *stationary methods*, *i.e.* where the iteration process remains independent from the previous iteration steps, convergence is slow for practical use, hence much faster *non-stationary* methods have been developed. In the following, we concentrate on these type of solvers. Here we only summarize the basic principles behind main types of iterative solvers.

When choosing an iterative method, one must choose between short recurrences[5] and the optimality of the solution. Currently, among the best iterative methods for solving a linear problem are the following Krylov subspace methods or their variants: *Conjugate Gradient* (CG), *Conjugate Gradient Squared* (CGS), *generalized minimum residual* (GMRES), *Bi-conjugate gradient* (Bi-CG), *Bi-conjugate gradient stabilized*

[4] See Ref. [82] for other freely available software for solving large sparse eigenvalue problems.

[5] This means that only the results of one foregoing step is needed for the next step and memory requirement is independent from the number of iterations

(Bi-CGSTAB) and *quasi-minimal residual* (QMR).

The general idea of solving $Ax = b$ iteratively, is to seek an approximative solution x_k from an affine subspace $x_0 + K_k$ by imposing the Petrov-Galerkin condition $b - Ax_k \perp L_k$, where both K_k and L_k are subspaces of size k and x_0 is an initial guess. For Krylov subspace methods, the subspace K_k is the Krylov subspace and different methods arise from different choices of the subspace L_k. In the first class of methods, one chooses $L_k = K_k$ or $L_k = AK_k$, which is the minimum-residual variation. These are often called *orthogonalization methods*. In the second class of methods, one chooses L_k as a Krylov subspace for A^T (transpose of A), which leads to *biorthogonalization methods*. Iterative methods can be divided roughly between the following three categories [192]:

1. Normal equation methods (*e.g.* CG and LSQR).
2. Biorthogonalization methods (*e.g.* Bi-CG, QMR, CGS and Bi-CGSTAB).
3. Orthogonalization methods (*e.g.* GMRES).

Normal equation methods are based on the fact that a matrix $A^T A$ is always symmetric and positive definite, hence one can solve problem $A^T Ax = A^T b$ with methods such as Conjugate Gradients (CG), which is considered to be the 'original' Krylov subspace method. However, when applied to the matrix $A^T A$, the convergence depends on the squared condition number and singular values of matrix A and one is required to do two twice as many matrix-vector multiplications. Because of these, the convergence is typically slow. The same goes also for derived methods, such as LSQR, which solves the problem in the least-squares sense. In the following we concentrate on two latter categories.

Biorthogonalization methods

Biorthogonalization methods are based on the bi-Lanczos algorithm which is a non-symmetric version of the Lanczos method. These type of methods are intrinsically non-orthogonal, which makes them harder to analyze theoretically and no optimality is guaranteed. The advantage is, that they use short three-term recurrence, which makes them memory-efficient.

In the bi-Lanczos algorithm one, constructs a similarity transformation $W_k^T A V_k = T_k$, where T_k is a tridiagonal matrix (from which the three-term recurrence essentially follows), matrix V_k is defined by the basis $v_0, \ldots, v_{k-1}$ of $K_k(A, v_0)$ and similarly matrix W_k by $w_0, \ldots, w_{k-1}$ for $K_k(A^T, w_0)$. Vectors $\{v_i\}$ and $\{w_i\}$ form a bi-orthonormal system, *i.e.* $\langle w_i | v_j \rangle = \delta_{i,j}$. The LU decomposition of the tridiagonal system $T_k = L_k U_k$ can be updated from iteration to iteration, which leads to a recursive update of

the solution vector. This variant of the bi-Lanczos method, which avoids to save all intermediate vectors, is known as the Bi-conjugate gradients method (Bi-CG).

The QMR method is closely related to the Bi-CG method. For a matrix R_k created from the residual vectors $r_0, r_1, \ldots, r_{k-1}$ with $r_i = b - Ax_i$, we can write the recurrence relations $AR_k = R_{k+1}\widehat{T}_i$, where $\widehat{T}_i$ is $(k+1) \times k$ tridiagonal matrix. This leads to a least squares problem $|b - Ax| = |V_{k+1}(\beta e_1 - \widehat{T}_k y)|$, where β is a constant given by the Bi-CG method. The optimal solution y is called the quasi-minimal residual approximation and it can be solved in straightforward manner. The method based on this approximation is the QMR method. Experiments suggest that the QMR method has a smoother convergence behavior than Bi-CG, but it is not essentially faster.

Each step of the Bi-CG and QMR algorithms requires a matrix-by-vector product with both A and A^T, where the latter only contributes by giving proper scalars required during the algorithm. However, one can also work without A^T by noting that the inner product of the residual vectors $r_i = b - Ax_i$ and $\widehat{r}_i = b - A^T\widehat{x}_i$ can be written as $\langle r_i|\widehat{r}_j\rangle = \langle P_i(A)r_0|P_j(A^T)\widehat{r}_0\rangle = \langle P_i(A)P_j(A)r_0|\widehat{r}_0\rangle = 0$ for $i < j$, where P_i is a polynomial of the degree i implicitly defined by the Bi-CG method. By doing so, explicit calculation of the vectors $\widehat{r}_i$ can be avoided, nor is there any multiplication with the matrix A^T. The resulting CGS method converges often faster than Bi-CG, but due to the squaring, build of rounding errors tend to occur and CGS usually shows a very irregular convergence behavior.

The BI-CGSTAB method is a variation of CGS, developed to remedy above numerical problems. Instead of squaring the Bi-CG polynomial, in the Bi-CGSTAB method one applies $r_i = Q_i(A)P_i(A)r_0$ using better i^{th} degree polynomials for Q_i, namely $Q_i(x) = (1 - \omega_1 x)\ldots(1 - \omega_i x)$ with suitable constants ω_j for $j = 1, \ldots, i$. In the Bi-CGSTAB method, ω_i's are chosen to achieve a steepest descent step in the residual direction by minimizing r_i. Further generalizations have been proposed to improve numerical stability, which has lead to variations of the method such as Bi-CGStab2 and Bi-CGSTAB(l) methods [173].

Orthogonalization methods

Orthogonalization methods are based on long recurrences and have certain optimality properties. The long recurrences imply that the amount of work per iteration and the required memory grow as the number of iterations increase. Therefore it becomes necessary to use restarts or to truncate vector recursions. The most notable method of this class is the GMRES method with its numerous variations.

In the basic GMRES method, the Arnoldi method is used to compute an orthonormal basis for the Krylov subspace $K_k(A, r_0)$. This results into upper $(k+1) \times k$ Hessenberg matrix $\widehat{H}_k$ satisfying $AV_k = V_{k+1}\widehat{H}_k$. Then the approximate solution $x_k = x_0 + z_k$ with $z_k \in K_k(A, r_0)$ minimizing the residual $|r_k| = |b - Ax_k| = \min_{z_k} |r_0 - Az_k|$ is found.

This optimization problem is solved using the identity $x_k = x_0 + V_k y_k$ and determining y_k from a resulting least squares problem. GMRES is a stable method with no breakdown, and due to the optimality, convergence is guaranteed. However, after some number of iterations, the method must be restarted to limit the size of the subspace. Restarting destroys the optimality and the related super-linear convergence. This problem has lead to proposal of several modifications of the original GMRES method, such as GGMRES and MGMRES [30].

For nonsymmetric matrices, it is often difficult to choose an iterative method. No single method is the best for all matrices and there are always examples in which one solver outperforms the other. Therefore, in practice, many solvers must be tried in order to find the best one for a given problem. In general QMR, CGS and Bi-CGSTAB are simple and reasonably fast for a large class of problems. If break down or bad convergence appear, GMRES method can be applied. Finally, LSQR always converges, but usually too slowly [184]. When the matrix transpose is available, which is always the case with the master equations, one suggested order of methods to apply is QMR, Bi-CGSTAB, CGS and lastly GMRES [17].

We have compared above methods for the repton and reduced island models by solving D_{eff} with the direct method described in Section 4.2.1 and using a stochastic potential. Computations were made using build-in functions of MATLAB. For the repton model, we consider the RD model with a 10-atom polymer in a $L = 3$ flashing ratchet, and for the island model we consider a 11-atom island in the electrophoretic ratchet. Parameters are kept similar to those used in Chapters 6 and 7. The corresponding sizes of H matrices are 708588 (RD) and 255120 (island). The parameters for the linear solvers are kept close to their typical default values as defined in MATLAB. The typical convergence behavior for different methods is shown in Fig. 5.1, measured with the residual norms and starting from the same random initial states. The computation times averaged over 20 independent runs are collected in Table 5.1.[6] The LSQR method was omitted from this table since it fails to converge within a reasonable time. For all the rest, computations were allowed to run until successful convergence (or failure). Results reveal, that the Bi-CGSTAB method is the best choice for these models with its combined performance in speed, stability and accuracy. The CGS method is equivalently fast, but as expected, it is more unstable, which can be seen from large fluctuations of the residual norm. The QMR method is stable, but slower than Bi-CGSTAB and CGS. However, the QMR method performs much better when solving periodic stationary states for a smoothly varying potential using the simple

[6] Computation time depends on the used hardware, therefore the values here are only valid for comparison against each other.

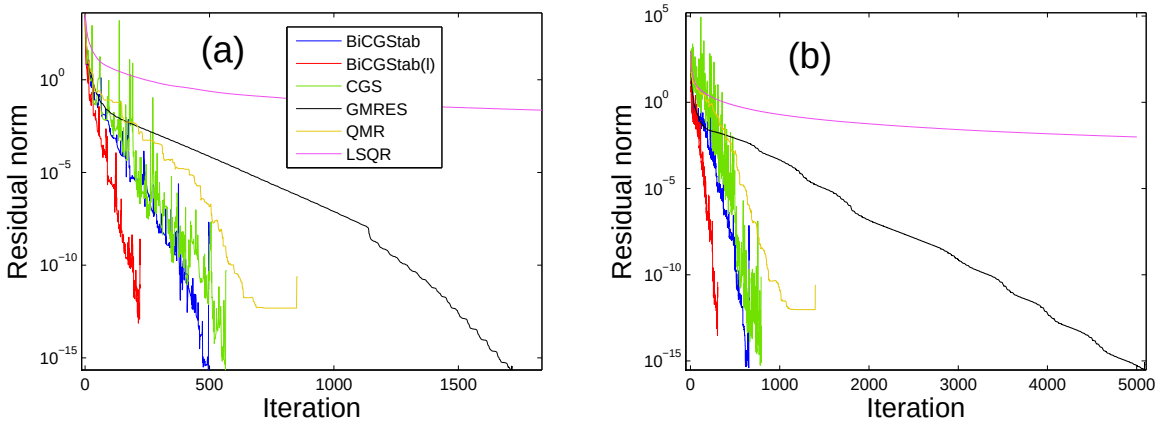

Figure 5.1: Comparison of different methods to solve the effective diffusion coefficient for (a) the RD model with $N = 10$ in a $L = 3$ stochastic flashing ratchet with $V_{\max} = 1$, and (b) the reduced island model with $N = 11$ in the electrophoretic ratchet with temperature 1000 K, field $E_1 = 0.05$ eV and time-symmetry $x = 1/4$.

Table 5.1: Computation times in seconds, averaged over 20 runs with random initial states.

Method	Rubinstein-Duke	Reduced island
Bi-CGSTAB	47.1	39.2
Bi-CGSTAB(l)	64.1	55.2
CGS	43.8	39.8
GMRES	503.0	731.3
QMR	77.5	76.3

multi-shooting scheme (see Section 5.1.2). The stability of the GMRES method is excellent, but it is very slow. It is notable that the results for repton and island models are very similar, although the models themselves are physically very different.

5.1.2 Numerical integration

For explicitly time-dependent stochastic generators or when studying transient states, numerical integration is needed. Starting with an initial state $P(t = 0)$, there are basically two ways to find $P(t)$: performing numerical matrix exponentiation or integrating the equations of motion.

The first way is to apply the matrix exponential [125]. Computing the time-development operator $O(t) := \exp(\int_{s=0}^{t} H(s)ds)$ directly requires the full spectrum of H, which is clearly out of reach for large matrices. Also the matrix $O(t)$ is always dense. Therefore matrix $O(t)$ cannot be evaluated for large systems. Instead of solving $O(t)$, one can

also use Krylov subspace projection to compute the product $O(t)P(0)$ based on the approximation $P(t) = \left[\exp(\int_{s=0}^{t} H(s)ds)\right] P(0) \approx p_k(\int_{s=0}^{t} H(s)ds)P(0)$, where p_k is a polynomial of degree k [170]. This type of method takes a full advantage of the sparsity and, as other Krylov subspace based methods, is usually fast and memory efficient. However, accuracy of this approximation varies and depends on the problem. Also, for the explicitly time-dependent stochastic generators, one must take additional effort to integrate $\int_{s=0}^{t} H(s)ds$.

The second method involves using general ordinary differential equation (ODE) integration algorithms, such as Euler and Runge-Kutta methods. These methods are simple, but since they are general ODE solvers, they do not take advantage of linear property of the problem. The basic working principle of these methods is alike; time is divided into small steps and the solution $P(t)$ is approached step by step starting from $P(0)$. For example, in Runge-Kutta methods, the state is updated with the scheme $P(t+h) = P(t) + \sum_{i=1}^{k} x_i v_i$, where v_i is a vector computed in the middle point of the interval $(t, t+h)$ using weights x_i. There are several ways to choose k, x_i and v_i (see *e.g.* [50]). One of the most widely used ones is the 4^{th} order Runge-Kutta (RK4) method with $k = 4$ and having even-spaced time intervals. To increase the efficiency, instead of keeping h as a constant, it can be varied during the computation in an adaptive manner. This requires an error-control scheme to choose a proper h. For RK4 method, this leads to so called adaptive Runge-Kutta 4-5 method, where 5th order ($k = 5$) result is compared against RK4 result, thus giving a scheme to choose a proper h.

Temporally periodic solutions

Next we consider solving a periodic *boundary value problem* of the type $P(t) = P(t+\tau)$, which is the time-dependent steady state. Formally this problem can be cast into time-independent form with

$$e^{H_{\text{eff}}\tau} = T\left\{e^{\int_{s=0}^{\tau} H(s)ds}\right\},$$

where T is the time ordering operator. In the long-time limit, the time-dependent solution with full integer cycles (*i.e.* $P(t) = \lim_{n\to\infty} P(t+n\tau)$) is given by the eigenstate corresponding to the eigenvalue 1 of the operator H_{eff}.[7] Unfortunately, H_{eff} can be explicitly computed only for very small or special types of driving protocols and systems [144]. However, one can apply ODE integration algorithms.

In addition to previous two methods for transient states, there are also numerical methods designed for boundary value problems [9]. For a boundary value problem, the solution can be computed by creating a mesh grid for the interval $[0, \tau]$ and then

[7] In mathematics periodic systems are typically studied using the Floquet theory, see Ref. [23] for its application for stochastic models.

finding a solution in each mesh point simultaneously. This is known as a *multiple-shooting* approach, whereas *single-shooting* has to be used if two previous methods are applied to find a periodic solution. The advantage of the single-shooting method is that it takes advantage of the speed and adaptivity of regular initial value ODE solvers. However, this method is more complicated and the memory requirement is much higher than by using the single-shooting method. The mesh grid must be dense if an accurate solution is required. In the special case of a smoothly varying function, such as $H(t)$ with a smoothly varying potential, a simple multiple-shooting scheme can be straightforwardly applied as follows. By using the first order discretization, one can approximate

$$H(t)P(t) \approx \frac{P(t+\Delta t) - P(t-\Delta t)}{2\Delta t},$$

with $\Delta t = \tau/m$ and m is the number of discretization steps. In the matrix form, this leads to a linear problem $\widetilde{H}\widetilde{P} = b$, where $\widetilde{H}$ includes $H(t)$ for all m time-steps and the discretization operator. The normalization is preserved by setting $b_i = 1 \; \forall \; i = Y, 2Y, \ldots, mY$, where Y is the dimension of $H(t)$. Although the size of the square matrix $\widetilde{H}$ is mY, it has a simple structure, and given a good initial state, the problem is not too hard to solve numerically.

To find a periodic solution, a good initial state is usually required to reduce the computation time, especially when using the single-shooting method. Without additional information, there are two good choices for an initial state: the distribution that corresponds to a steady state of $H(t)$ with a fixed time at interval $[0, \tau]$ and a combination of distributions for several times. The first choice works fine if τ is large compared to the leading relaxation time. If this is not the case, the second choice is better. A simple combined state is a linear combination $\sum_{i=1}^{N} x_i P_i^S / \sum_{i=1}^{N} x_i$, where P_i^S is the steady state of $H(t_i)$ and weights x_i can be chosen symmetrically or they can be optimized for the specific system. For example, when studying a system with two potential states (*i.e.* $S = 2$) and the deterministic scheme (see Section 3.1.1), one good initial state is $\left(\tau_1 P_1^S + \tau_2 P_2^S\right)/\tau$.

Verifying the periodicity of the steady state is easy when using the multiple-shoot method, for which the approximate error is usually readily provided by the method. For the single-shooting method, the converge can be verified for example by keeping track of the difference $|P(t) - P(t-\tau)|$. In addition to P itself, one should also keep track of the values of observables of interest to help decide when the adequate convergence is reached.[8]

[8] For example, adequate precision for a periodic steady state velocity v is typically obtained much sooner than for the effective diffusion coefficient D_{eff}.

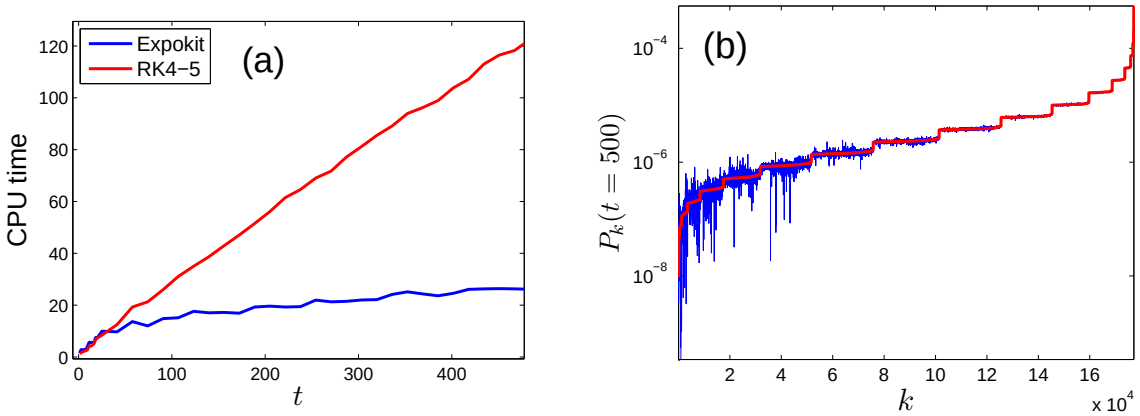

Figure 5.2: Comparison of the Krylov subspace based matrix exponential method (blue line) and Runge-Kutta 4-5 method (red line) for integration of distribution $P(t)$. (a) Computation time as a function of the integration time t for the island model. (b) Components of the solution $P(t = 500)$ for the RD model.

We end this Section by comparing the RK4-5 and Krylov subspace matrix exponential methods to solve the transient state $P(t)$, starting from a randomized initial state $P(0)$. Matlab's build-in implementation of RK4-5 is used, and for the exponential method, we use Expokit[9], which is also coded using MATLAB. For both methods, similar error tolerances are used, while keeping other method-dependent parameters close to their recommended defaults. We use the reduced island model in a static field and the RD model in a static ratchet potential (*i.e.* $S = 1$) with $L = 3$. We set $N = 11$ for both models. In Fig. 5.2(a), the computation time is shown as a function of the integration time t, averaged over 10 independent runs for the island model. The behavior for the RD model was found to be almost identical. As expected, the matrix exponential method is generally much faster than Runge-Kutta integration when t is large. Only with small values of t, the Runge-Kutta method is slightly faster, because there is no need to set up a Krylov subspace. However, the accuracy of the matrix exponential method is found to be poor for large t as the numerical error accumulates. This is demonstrated in Fig. 5.2(b) where we have plotted the snapshot of all components of $P(t = 500)$ in an increasing order for the RD model. In the Krylov subspace method, small components cannot be computed accurately, while the Runge-Kutta method provides accurate results for all components. Because of this, the matrix exponential method results in inaccurate values for the velocity. Therefore, we find Runge-Kutta method more suitable for solving transient and time-dependent steady states.

[9] `http://www.maths.uq.edu.au/expokit`

5.2 Optimization

The good numerical accuracy of the master equation method also makes it possible to perform numerical optimization. In this Section, we describe methods that can be applied to optimize scalar valued observables with respect to model parameters and sequences. This leads us to two separate and specialized fields of nonlinear constrained optimization of smooth functions and combinatorial optimization of cycles on graph.

5.2.1 Optimization with respect to cycles

Consider a system described by a stochastic generator H. As noted in Section 2.1.3, a nonequilibrium state results in a nonvanishing current on graph that represents the state space. Depending on the details of the model and on the way the driving forces are implemented, some cycles become statistically more important than the others. We are interested in cycles that become most important with respect to a given measure. Such cycles can give important insight for example on how the transport process proceeds microscopically. To compare cycles, one needs a measure and a computational method to determine the most important cycles. One type of a measure, based on the probability of the cycle, was considered in Section 2.2.3 (see Eq. (2.8)). In this Section, we introduce another one which is suited for very large graphs. We begin by introducing algorithms for cycle enumeration and mean cycle ratio optimization, which are both well-known problems in computational graph analysis [105]. In the following, only basic knowledge of the graph theory is expected (see *e.g.* Ref. [15]).

Cycle enumeration

The task of finding all simple (*i.e.* non-intersecting) cycles of the graph is known as *cycle enumeration*. All known methods for this problem use a brute-force approach. For directed graphs, there are two efficient methods by Johnson and Tarjan [91], both from the 1970's. These methods are based on the standard depth-first search and use backtracking and pruning, which significantly improve the efficiency of computation because there is re-counting of already found cycles. Not much progress has been made since these algorithms, and Johnson's algorithm is still considered to be the fastest one with an upper time bound of $O\left((n+m)(c+1)\right)$, where m is the number of edges, n is the number of vertices and c is the number of simple cycles [114]. Since the number of cycles has usually a factorial dependency on n and m, the running time of this algorithm becomes huge for large graphs. The worst case scenario occurs when the graph contains very long cycles, including one or several Hamiltonian cycles.[10] In such cases, the number of simple cycles is very large even for small graphs.

[10] Hamiltonian cycle is a simple cycle that includes all vertices of the graph.

Optimal cycle ratios

Consider a directed graph with n vertices and m edges. Each directed edge e is associated with two real numbers: a positive or negative weight $W_1(e)$ and a positive weight $W_2(e)$. Let us define two object functions,

$$\rho(C) = \frac{\sum_{e \in C} W_1(e)}{\sum_{e \in C} W_2(e)} \tag{5.1}$$

$$\gamma(C) = \frac{\sum_{e \in C} W_1(e)}{|C|}, \tag{5.2}$$

where C is a simple cycle and $|C|$ is the number of edges in the cycle C (*i.e.* cycle length). Using these, we define two combinatorial optimization problems: the *minimum cycle ratio* (MCR) ρ^* and the *minimum cycle mean* (MCM) γ^* with

$$\rho^* = \min_C \rho(C)$$
$$\gamma^* = \min_C \gamma(C),$$

where the minimization is performed over all simple cycles. Since the MCM problem is just a special case of the MCR problem, any algorithm that solves the latter can also solve the first. We concentrate on the MCR problem. The need to solve this type of problem originates from the classical *tramp steamer problem*, where the captain of the steamer wants to know what ports the steamer should visit, and in which order, in order to maximize his average daily profit. Traditionally W_1 and W_2 are therefore identified as a *cost* and a *transit time* [105].

The solution of the MCR problem can be associated with the sign changes of cycle weight computed with $\sum_{e \in C} \widehat{W}(e)$, where $\widehat{W}$ is a modified weight function. To see this, let us define a new edge weights $\widehat{W}(e) := W_1(e) - \rho W_2(e)$ where ρ is an arbitrary real number. Using these new weights, three situations appear for a given ρ [1]:

- A negative cycle exists: $\sum_{e \in C} \widehat{W}(e) < 0 \Leftrightarrow \rho > \rho(C) \geq \rho^*$
- No negative cycles: $\sum_{e \in C} \widehat{W}(e) > 0 \Leftrightarrow \rho < \rho^* \leq \rho(C)$
- Zero cycle: $\sum_{e \in C} \widehat{W}(e) = 0 \Leftrightarrow \rho^* = \rho(C)$

Starting with an arbitrary value of ρ and using a shortest path algorithm that can detect a negative cycles in the graph, and by iterating ρ, one can approach the precise value for which the last negative cycle disappears and thus find ρ^*. Negative cycles can be found for example by using the Floyd-Warshall algorithm [191].

Several algorithms have been proposed for an efficient numerical implementation of this general idea. A list and comparison of algorithms is given in Ref. [42]. It has been found that *Howard's algorithm* [83] is one of the fastest algorithms available [41, 42, 40]. Efficient implementation of this method can be found in the Boost C++ library.[11] There are two known lower bounds for the running time of this algorithm: its running time is at most $O(nmc)$, where c is the number of simple cycles, or its running time is at most $O(n^2 m(\max(W_1) - \min(W_1))/\epsilon)$, where ϵ is the required numerical precision of the algorithm [42]. However, these are only approximations and the exact complexity of Howard's method is not known. Since the second of these upper limits for the running time does not depend on the number of cycles, it is evident that this problem is much easier than the enumeration.[12]

Optimized cycles for nonequilibrium systems

It is evident that finding a cycle related to the largest measure via enumeration is computationally too expensive for all but very small graphs. There is no efficient way to find a simple cycle with a maximal (or minimal) weight using the measure of the type (2.8). Solving this problem exactly requires full enumeration, which is an impossible if the graph is large and has long cycles. Therefore we propose using a measures of the type (5.1) and (5.2), and use them to find cycles that are important for the transport. Because the circulations are directed, we also reduce the number of cycles by considering only directed graphs where the direction of the edges goes along the net probability flows.

We start by noting that if a system is closed and the probability is conserved, there must also be a cycle with circulation. The situation is analogous with electric flows in a closed circuit. For a time-independent steady state, this follows from noticing that for every vertex, one must have $0 = \sum_i [J_{y,i} - J_{i,y}]$ for all y. Similarly, for the periodic time-dependent steady state $P(t) = P(t+\tau)$ one has $0 = \int_{s=0}^{\tau} \sum_i [J_{y,i}(s) - J_{i,y}(s)]\, ds$ for all y. These conditions ensure that if there are net flows in the graph, there is at least one cycle in the directed probability flow graph.

Once the steady state distribution P^{S} of H is found, the net currents between the states can be computed as $J_{i,j} = P_i^{\mathrm{S}} H_{i,j} - P_j^{\mathrm{S}} H_{j,i} \;\forall\; i, j$. If P^{S} and H are time-dependent, we consider their expected values integrated over a single steady state temporal period. We then create a graph G such that if $J_{i,j} > 0$, there exists a directed edge $i \to j$ in G with a weight $J_{i,j}$. The choice $W_1(e) = J(e)$ and $W_2(e) = 1$ creates a MCM type measure in the sense 'net transition rate/edge', and the choice $W_1(e) \equiv 1$ and $W_2(e) = 1/J(e)$ creates a MCR type measure in the sense 'average net transition rate' for a cycle. Using the previously introduced notation, we define

[11] Boost C++ is an efficient peer-reviewed library of algorithms `http:\\www.boost.org`

[12] This is, of course, expected, since any cycle related optimization problem can be solved exactly by doing the full enumeration of cycles.

object functions

$$\gamma(C) = \frac{\sum_{e\in C} J(e)}{|C|} \tag{5.3}$$

$$\rho(C) = \frac{|C|}{\sum_{e\in C} 1/J(e)}. \tag{5.4}$$

These measures are always positive and have a dimension '1/time'. Having a simple linear form, the first measure is robust against the appearance of arbitrary small rates, whereas the second measure rapidly drops to zero if very small weights appear. Therefore the first measure is numerically more stable, whereas the second measure is intuitively more pleasing, since there is a heavy penalty for cycles with slow net flows. Both measures rely on net currents and therefore they only work for nonequilibrium states. Note that for irreversible transitions, such as those appearing in the TASEP model, the currents are directed by construction and both measures are well suitable also in such case. When compared to the measure $w(C)$ defined in Eq. (2.8), there are two differences. Firstly, the number of cycles is significantly reduced since the graph is directed, thus making the computations much easier. Secondly, in $w(C)$, the sampling is made over cycles (*i.e.* how often the cycle is realized during the process), whereas in above measures $\gamma(C)$ and $\rho(C)$, the sampling is made over the expected probability flows of individual transitions, which are then combined into a cycles by using the graph topology. Being unable to optimize the stochastic sequences using $w(C)$, we instead optimize the flows occurring in the corresponding master equations (which are deterministic). These problems are fundamentally different, but according to our numerical studies using small polymers and islands, the optimized paths typically turn out to be the same ones.

Measures (5.3) and (5.4) can be augmented with an additional weight function. For an observable defined with an edge weight function $f(e)$, we can take $W_1(e) = f(e)J(e)$ and $W_2(e) = f(e)$, leading to

$$\gamma(C)_f = \frac{\sum_{e\in C} f(e)J(e)}{|C|} \tag{5.5}$$

$$\rho(C)_f = \frac{\sum_{e\in C} f(e)}{\sum_{e\in C} 1/J(e)}. \tag{5.6}$$

Now let us consider the case, where the function f is given by center-of-mass displacements $D(e)$ of transitions. Then the dimension of the measures become 'distance/time' and they can have negative and positive values. We call cycles with maximal $\rho(C)$ and $\gamma(C)$ *dominating processes*, and cycles with maximal (or minimal) $\rho(C)_D$ and $\gamma(C)_D$ *dominating transport processes*.

Whether there is a difference between ρ and ρ_D, and γ and γ_D, depends on the details of the system. It may turn out, that γ and ρ only include transitions that are

not responsible for directed transport, but transitions of non-transporting diffusive motion only. Formally, this means that $\sum_{e\in C} D(e) = 0$ and in that case we call the process *non-transporting*, as the net transport for the cycle is zero. This is typical to ratchet transport, since the object spends most of its time near the minimum of the potential, being unable to move until the suitable state of the potential and internal state is reached. Therefore ρ_D and γ_D carry more interesting information about the transport, as they also take into account the displacements. If the cycle has a property $\sum_{e\in C} D(e) \neq 0$, we call it a *transporting process*. However, it is not guaranteed that the dominating process is a transporting process in either case.

To study dominating transport processes, it is sometimes useful to consider a reduced system instead of the full one. Such situations typically arise when temporal and/or spatial states of the potential are included in the master equations, but one is only interested in the internal dynamics of the transported objects (*e.g.* polymers and islands). Then one can sum over all non-interesting states of the master equation set to receive averaged J and D that correspond to a reduced system. For example, for the repton model with a stochastic potential with $S > 1$ and $L > 1$, averaging over all potential states reduces the dimension of these graphs from $SL3^{N-1}$ to 3^{N-1}. Dealing with the reduced graphs instead of full ones, also makes the optimization of γ and ρ easier.

Graph optimization based on measures (5.3)-(5.6) is straightforward and fast, and, in principle, can be done for all finite discrete stochastic nonequilibrium systems. This method is suitable in situations where the network is too large and complex to be studied 'manually' (see *e.g.* [35] for studies of small networks). Whether this analysis of dominating cycles is worth the effort, depends on the complexity of the system and the importance of the internal dynamics of the objects to the transport process. For complex many-particle systems, this analysis can reveal interesting details of the transport, as demonstrated in Sections 6.7 and 7.4. Interest of analyzing cycles has been also recently emerged in other fields, such as microbiology [99]. Also other approximate methods to determine dominant paths instead of cycles have emerged recently [61].

As an example of full enumeration, we apply Johnson's method to enumerate all directed cycles for a 5-atom island in a static field by using the reduced island model. In Fig. 5.3, we show the total number of cycles by their length for $E = 0.04$ eV. Depending on the field amplitude and direction, the total number of cycles is of order 10^9. Considering that there are only 63 vertices and around 170 edges in the corresponding directed graph J, the number of cycles is already huge and the computation takes several days. Majority of the cycles are long, and even Hamiltonian cycles are

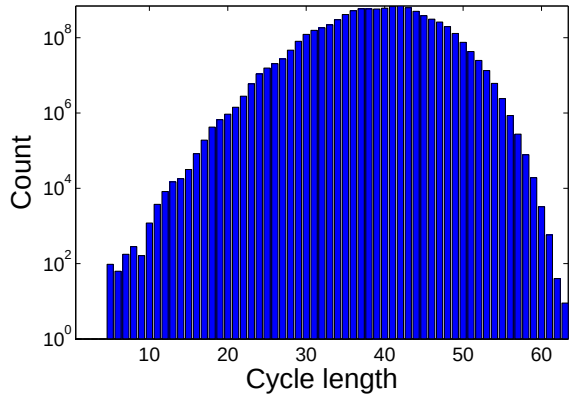

Figure 5.3: The number of directed cycles with different lengths for the 5-atom reduced island model with $E = 0.04$ eV, $T = 800$ K and $\gamma = \alpha = 0°$.

common. The shape of the distribution is found to be quite similar for both island and repton models. Because of the large number of cycles, full enumeration becomes practically impossible for systems over 100 states or even less.

5.2.2 Optimization with respect to continuous parameters

The master equation method allows fast and accurate computation of observables. This opens up an opportunity to apply optimization methods to model parameters. Although some parameters of interest might be discrete, from a computational perspective it is usually easier to consider continuous parameters. In this Section, we consider local optimization of scalar valued observables (denoted by the object function f) computed using master equations. Since the observables are determined by the master equation system, they are continuous and smooth with respect to the parameters.[13] We also review some of the most important optimization methods currently available. A more comprehensive listing and details of the methods can be found in many textbooks, such as [37, 74, 128].

First we must determine the type of optimization, in which the following three aspects are important. Firstly, since computing of observables involves solving eigenstates and/or integration, the object function is clearly non-linear. Secondly, since we do not know the functional form of the object function, we can't directly evaluate its derivatives. Thirdly, parameters of the model typically have some physical constraints they must obey, at least upper and lower bounds. Such constraints can be linear or non-linear. In addition to the known constraints, there are often so called 'hidden

[13] Although functional forms for observables cannot be generally computed, we know that they consists of basic arithmetic operations.

constraints' which are related to points in the feasible space where object function cannot be evaluated, because of technical reasons. Such a situation usually occurs if the master equation set scales badly (*i.e.* becomes stiff). We are thus dealing with a nonlinear constrained optimization problem.

For a nonlinear constrained optimization problem, there are two classes of methods available; derivative-based and derivative-free. In the former class, derivatives of the object function, computed either directly or approximated by finite-differences, are used to determine the optimality and search directions [74, 128]. The latter class of methods relies entirely on values of the object function, without using derivatives in any form. These methods do not generally require the object function to be smooth or even continuous, and they are also often designed to tolerate noisy object functions. Majority of the research effort has been devoted to derivative-based methods, whereas derivative-free methods have become of more interest only within the last decade [37]. Which of the methods works the best, depends on the problem at hand.

Problem formulation

The general constrained optimization problem is

$$\min_{x \in R^n} f(x) \quad \text{subject to} \quad \begin{cases} c_i(x) = 0 \ \forall \ i \in E \\ c_i(x) \geq 0 \ \forall \ i \in I \end{cases}, \tag{5.7}$$

where E and I are sets of indices for equality and inequality constraints, respectively. Alternatively, constraints can be written in somewhat more transparent form as

$$\vec{c}_{\text{in}}(x) \leq 0, \quad \vec{c}_{\text{eq}}(x) = 0, \quad Ax \leq b_{\text{in}}, \quad A_{\text{eq}}x = b_{\text{eq}}, \quad L \leq x \leq U,$$

where matrices A and A_{eq}, and vectors b_{in}, b_{eq}, L and U, create linear constraints, functions $\vec{c}_{\text{in}}$ and $\vec{c}_{\text{eq}}$ create non-linear constraints. If equality constraints are present, then depending on the size and rank of the matrix A_{eq}, the dimension of the state space can be often reduced by suitable basis transformation. The solution is approached iteratively by going through a large number of points in the feasible state-space, until the current iterate fulfills the optimality conditions. An iteration process requires solving the following sub-problems: (1) how to move to the next iteration point, (2) how to fulfill constraints, and (3) testing for the optimality of the solution.

Derivative-based methods

The traditional way of optimization relies on the derivatives of the object function. Since in our case the derivatives are unavailable, they must be estimated by finite differences. This usually works well if the object function is a well-behaved and does not contain noise. Two most widely used derivative-based methods for nonlinear constrained problems are *active set* and *interior point* methods, which differ in the way how the constraints are taken into account.

Moving to the next iteration, one uses either *line search* or *trust region* strategy. In the former, one chooses a unit vector p_k and a scalar $a > 0$ such that $x_k + ap_k$ gives an improved iterate. A popular way to choose p_k is the Newton method using the second-order Taylor series approximation $m_k(\epsilon) := f(x_k + \epsilon) \approx f(x_k) + \epsilon^T \nabla f(x_k) + \epsilon^T \nabla^2 f(x_k)\epsilon/2$. For a positive-definite second derivative, the Newton direction is found by solving $m_k(p) = 0$.[14] Instead of the pure Newton direction, computationally less heavy Quasi-Newton direction is typically applied, where instead of a true Hessian, an approximation is used and updated iteratively.[15] Once the direction has been fixed, the step distance a can be found by solving a one-dimensional minimization problem $\min_{a>0} f(x_k + ap_k)$.

In the trust region strategy, the information gathered about f is used to construct a simple model function $\widehat{f_k}$ which mimics f near the current point x_k. The region where $\widehat{f_k}$ is considered a good approximation of f, is the trust region. Within this region, the candidate step p_k is found by solving the subproblem $\min_{p_k} \widehat{f_k}(x_k + p_k)$, which is much easier for $\widehat{f_k}$ than f itself.[16] During the optimization, the trust region can be enlarged or shrunk as needed.

The local optimality of the solution can be determined from the first and second derivatives. However, most modern optimization methods are based on the so-called Karush-Kuhn-Tucker (KKT) conditions, which give first-order necessary optimality conditions for the Lagrangian function $L(x, \gamma) = f(x) - \sum_i \gamma_i c_i(x)$, where γ_i's are the Lagrange multipliers. The KKT approach to nonlinear optimization generalizes the method of Lagrange multipliers, which allows only equality constraints.

Active set method

Active set methods are based on the observation that, in general, it is much simpler to solve equality-constrained problems than to deal with inequalities. The conventional active set approach is divided into two phases; first f is ignored while a feasible point is found for the equality constraints, next f is minimized while feasibility is maintained. One starts by making a guess of the set W of constraints, that are satisfied as equalities at an optimal point. Using the Lagrangian, one then solves a problem in which the constraints in the active set W are imposed as equalities, and the constraints not in W are ignored. Then, one checks whether the resulting point satisfies the KKT conditions using Lagrangian multipliers. If so, a local optimum has been found, otherwise a new choice for the active set is made, and the process is repeated. The path of points never leaves the feasible region, but it can hit its boundaries. Particularly, active set strategy

[14] For non positive-definite case, the definition of p_k is modified to make it satisfy the descent condition while retaining the second-order information [128].

[15] One chooses the new Hessian approximation B_{k+1} which mimics the property $\nabla^2 f_k(x_{k+1} - x_k) \approx \nabla f_{k+1} - \nabla f_k$. The most popular formula updating B is a Broyden-Fletcher-Goldfarb-Shanno (BFGS) method.

[16] Unlike in the line search methods, the direction and distance are solved simultaneously.

is applied within Sequential Quadratic Programming (SQP) methods, which convert the nonlinear optimization problem into linear-constrained quadratic sub-problems. A detailed description of the SQP method can be found in Ref. [128].

Interior point method

In interior point method, the problem (5.7) is reformulated in the form

$$\min_{x,s} \left[f(x) - \mu \sum_i \ln(s_i) \right] \quad \text{subject to} \quad \begin{cases} \vec{c}_{\text{eq}}(x) = 0 \\ \vec{c}_{\text{in}}(x) - \vec{s} = 0 \\ \vec{s} > 0 \end{cases} ,$$

where the scalar μ is positive. The components s_i of the vector $\vec{s}$ are called slack variables. This new object function has smooth barriers at the limits of the feasible region. The path of generated points never leaves the feasible region and cannot hit its boundaries. This type of penalty barrier approach consists of finding approximate solutions to the barrier problem and reducing μ towards zero, from which the solution for the original problem is recovered. Further details can be found in Ref. [128].

Interior point and SQP methods are considered to be very powerful algorithms for large-scale nonlinear optimization problems. Active set approach typically requires a larger number of iteration steps, while a single iteration is computationally inexpensive. Interior point approach requires a smaller number of more expensive steps. For very large problems, interior point methods are often more efficient. However, when a good estimate of the solution is available (a 'warm start'), the active set approach may converge rapidly.

Derivative-free methods

The methods designed not to rely on derivatives or their approximations, are called derivative-free or direct search methods. The performance of derivative-free methods is not usually comparable to that of derivative-based methods in accuracy or in number of parameters to be optimized. The stopping criteria are also a challenge in absence of derivatives and when f includes noise. When compared to the derivative-based methods, derivative-free methods are reasonably straightforward to implement for any model and therefore they can be used as the method of first recourse. The requirements from a user are minimal and algorithms themselves require setting only a few parameters [37].

Here we only consider the most basic derivative-free method known as the *pattern search method* (also known as as the directional direct-search method). Pattern search methods are characterized by a series of exploratory moves that consider the behavior of the object function at a pattern of points. The exploratory moves consist of

a systematic strategy for visiting the points in the lattice in the immediate vicinity of the current iterate point. This is called polling. There are several different choices for creating a search mesh and performing the polling. For example, the mesh can be created by using the generalized pattern (GP), the generating set (GS) and the mesh adaptive direct (MADS) algorithm. Put in short, the GP method uses axis directed basis vectors, whereas GS can take into account the linear constraints in search directions. MADS is a further generalization of GS type algorithms by allowing even more flexible search directions. The number of basis vectors is either $N+1$ or $2N$, where N is the number of variables to be optimized. Polling can be complete or partial, which means that as soon as a better value for f is found, polling is stopped. The search grid is typically enlarged or shrunk during the run. Iteration is stopped when the tolerance for the object function or the minimum grid size is met. Constraints can be taken into account by adding penalty for constraint violations or using a hard barrier. However, handling of constraints is typically crude when compared against interior point and active set approaches.[17] Additional details of different methods and theory can be found in Ref. [37]. For a listing of freely available derivative-free optimization software see Ref. [151].

To compare active set, interior point and pattern search optimization methods, we have computed the optimal charge distribution and the optimal temporal flashing period for the non-homogeneous RD model, such that the velocity function $v(\mathbf{q},\tau) := v(q_1, q_2, \ldots, q_N, \tau)$ is maximized and minimized. Non-zero velocity is generated by a stochastically flashing ratchet with $S = 2$, $L = 3$ and $V_{\max} = 1$ (this potential is discussed in more details in Chapter 6). This constrained optimization problem is a rather complicated one in the sense, that there are several local maxima and minima and the parameter space includes two types of variables (charges and temporal period). There are $N+1$ variables to optimize. We consider a situation where the total charge is limited by an equality $\sum_i q_i = Q$ or an inequality $\sum_i q_i \leq Q$. The temporal period τ has only a lower bound $\tau = 0$, but for better numerical stability, we set limits $10^{-4} < \tau < 10^6$ (these are the 'hidden constraints' discussed previously). We use MATLAB implementations for all three methods (active set method is implemented in the SQP algorithm).[18] Randomized near-uniform (*i.e.* $q_i \approx 1 \;\forall\; i$) initial charge distributions are used. In this test, we set $N = 9$, which already requires several hours of computing.

Solving the problem several times using different methods, it becomes evident that the

[17] Constrained derivative-free optimization is still a subject of intense research and most derivative-free methods are currently designed only for unconstrained problems.

[18] All three methods are included in Optimization Toolbox (version 5.0) and the Global Optimization Toolbox (version 3.0).

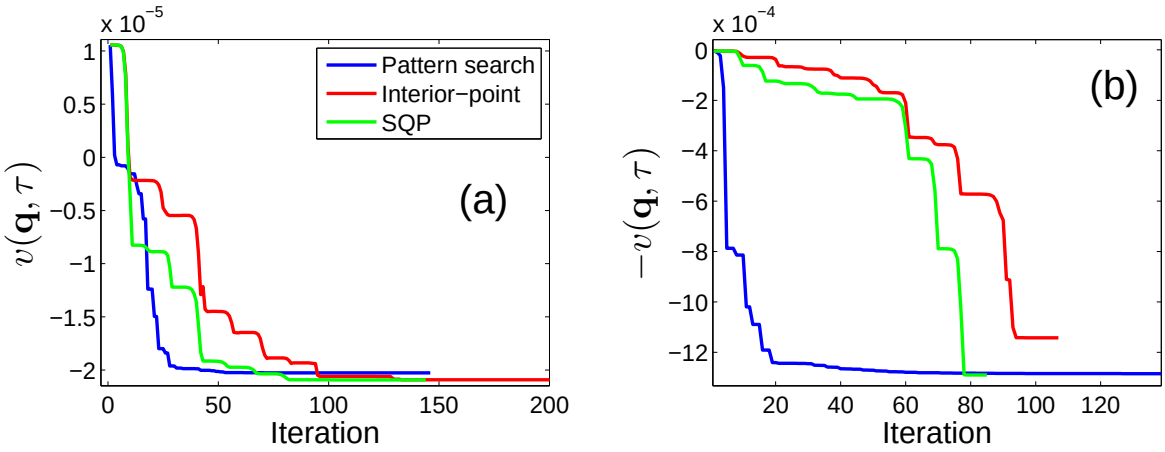

Figure 5.4: Example optimization runs of (a) the inverse and (b) the main velocity for the RD model, with $N = 9$ in a stochastic flashing ratchet, with $S = 2$, $L = 3$ and $V_{\max} = 1$. The same initial state is used for all three methods.

global maxima and minima are found at the boundary of the feasible space, *i.e.* we may use condition $\sum_{i=1}^{N} q_i = Q$. The problem involving the inequality is more complicated to solve and all three methods usually fail to find a good solution, especially SQP. This emphasizes the importance of a proper problem formulation before the optimization. In Fig. 5.4, a typical convergence behavior of the methods is shown. For the pattern search method, satisfactory results were reached using GS pattern with $2N$ basis vectors and a complete polling. Using other patterns or only $N+1$ basis vectors, often fails or leads to slower convergence. The velocity is shown as a function of the iteration number when optimizing the velocity in both (a) inverse and (b) main direction (the difference between these are explained in Section 6.3). The latter optimization turns out to be much more complicated, because of several very deep local minima created by accumulation of the charge on a single repton (this is expected, because of the exponential form of the rates). In Table 5.2, the computational times, the number of iterations and the number of function evaluations are shown as a median for 10 independent runs.

There is no explicit winner between the methods. The convergence of the pattern search method is rapid at the beginning, but then slows down. It fails to find the global minimum for the inverse direction, but finds it for the main direction, although with a slight violation of constraints. Choosing the proper polling pattern and type is essential, which requires testing many combinations. This method also needs lots of function evaluations. The SQP method converges well and reliably for both problems and requires less function evaluations. It is also most robust against changes of the initial state. However, it fails badly when using inequality constraints. The interior point method is reliable, but converges more slowly and requires lots of evaluations. As expected, both the SQP and the interior point method respect constraints well.

Table 5.2: Median results over 10 independent optimization runs with random initial states, using the interior point (IP), the pattern search (PS) and the SQP method.

	Inverse direction			Main direction		
	IP	PS	SQP	IP	PS	SQP
Time (10^{-2})	185	112	108	77	116	63
Iterations	232	139	132	108	209	82
Evaluations	2790	1580	1645	1223	1523	931
Value (10^4)	0.209	0.204	0.209	11.43	12.82	11.43

5.3 Monte Carlo method

Monte Carlo methods form the largest and the most important class of numerical methods used for solving statistical physics problems [126]. The idea of the method is not to compute probability distributions directly, but approximate those by averaging over a large number of sampled paths, that are generated using random numbers. The law of large numbers ensures that the expected values of observables approach those computed directly by solving master equations. The Monte Carlo method can be used for any type of systems and all observables. For discrete-time systems, classical Metropolis algorithm is often used to create the dynamics for simulations. For continuous-time systems a popular continuous-time Monte Carlo method was introduced by Bortz *et al.* in 1975 [21], and since then, several improvements have been made [28]. This method is known as the *kinetic Monte Carlo* or *N-fold* algorithm and it works by sampling sequences and waiting times separately (the theory behind this was discussed in Section 2.2.3).

In the N-fold algorithm, transitions (reactions) are divided in different classes according to their rate. During the simulation, one keeps up a list of all available reactions for the current state of the system. Time-steps and reactions occur randomly such that they correspond to the dynamics of the master equations. In this work, we implement the kinetic Monte Carlo method using the following algorithm (see Ref. [88]):

1. **Initialization**. Generate an initial state, create reaction lists and set elapsed time to zero.
2. **Time-step generation**. Increase the time by generating an exponentially distributed time-step using the total escape rate.
3. **Picking a reaction**. Randomly pick a reaction from the list and test check whether it is allowed. If the reaction is not allowed, go to step 6.
4. **Allowed reaction**. Make the transition into a new state and remove the reaction from the list.

5. **Adding new reactions**. Add new reactions that became available. Go to step 7.

6. **Forbidden reaction**. Remove the reaction from the list.

7. **Continuation**. If the ending criterion is met, end simulation. Otherwise go to step 2.

The only model-dependent parts of the algorithm are the initial state generation, adding and checking reactions. In our implementation, the reaction list is created using a linked list.[19] Technical details about each step can be found in Ref. [88].

The major downside of the Monte Carlo method is the low accuracy. Accurate results require lots of computation time and careful monitoring to ensure validity of the results. One must choose the number of independent iterations and simulation time carefully to get correct (steady state) sampling, while simultaneously trying to keep computational time as small as possible. If low quality or unsuitable random number generator is used, bad sampling may occur and the results will be unreliable. Computing certain types of observables, such as relaxation times, may be complicated. Since the data computed via Monte Carlo method is noisy, post-processing, including smoothing and (polynomial) fitting, is usually needed to extract information, such as maximum and minimum values and numerical derivatives.

Although the Monte Carlo method is straightforward, the efficient implementation for a specific model can be tricky. To get accurate results, finding and checking the reactions cannot be too time consuming, hence the usefulness of the method depends on the complexity of the model. If the model is very complicated, *e.g.* the interactions are long-ranged and there are lots of reactions, manipulating the data structures can become the bottleneck for the simulations.

Adding new reactions in the island model

The core part of the kinetic Monte Carlo algorithm is adding reactions to the reaction list. This is typically the most time-consuming part of the algorithm. For the island model, the search for new reaction takes place in the neighborhood of the hopping atom shown in Fig. 5.5. Moving a single atom affects 16 neighbor lattice sites and their atoms, by either allowing or blocking moves and/or changing energy barriers. For those sites numbered with 1-6, transitions can be created or blocked and the barriers changed. For sites numbered with 7-16, only the barriers might be changed for some of the transitions. It is easy to see, that increasing the interaction length would greatly increase the number of affected neighbor atoms, thus increasing the

[19] We also implemented a binary tree list, which, however, in most situations turned out to be less efficient for the island model.

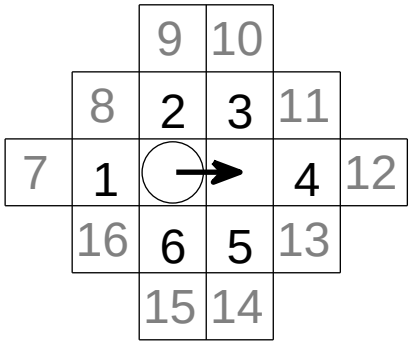

Figure 5.5: The local neighborhood that has to be checked in the kinetic Monte Carlo simulation after the transition of a single atom (sphere at the middle). For sites marked with gray, only the energy barriers of the already existing reactions can be affected and for the rest, new reactions are created or old ones disabled.

computational cost of the simulation. More technical details of the kinetic Monte Carlo simulations for the island model can be found in Ref. [79].

6 Results for the repton model

In this Chapter, we present selected results from Articles I and II for the repton model introduced in Section 3.3. Also some additional results not found in the Articles are presented in Section 6.2. The results shown in this Chapter are computed using the numerical master equation method. Since the repton model includes a large number of parameters, some of them must be fixed, primarily those that have a minimal qualitative impact on the results. In addition to the repton count N, other parameters in the models have the following interpretations:

- The environment $\leftrightarrow$ the potential $V(x,t) = V(x+L, t+\tau)$
- The medium $\leftrightarrow$ tube deformation Ω (0 for RD, 1 for FM)
- The polymer internal fine-structure $\leftrightarrow$ charges $q_1, \ldots, q_N$

The single most important parameter is the temporal period τ of the potential, which is also easily controlled in experimental set-ups. The parameter Ω models the porosity and viscosity of the medium by either restricting the polymer strictly into the reptation tube ($\Omega = 0$) or not ($\Omega = 1$). We set $L = 3$ for the spatial period (with the only exception made in Section 6.2), and use two potential states (*i.e.* $S = 2$). These choices allow both maximal N/L ratio and keeps matrix sizes feasible for the numerical matrix equation method. With these choices, a flashing ratchet is defined by setting $V_{\mathrm{on}}(1) = 0$, $V_{\mathrm{on}}(2) = V_{\max}/2$, $V_{\mathrm{on}}(3) = V_{\max}$, and $V_{\mathrm{off}}(x) = 0\ \forall x$, and the traveling potential is defined by $V_1(1) = V_2(2) = V_{\max}$ and zero for $V_1(2)$, $V_1(3)$, $V_2(1)$ and $V_2(3)$. These potentials are illustrated in Fig. 6.1. The maximum potential strength $V_{\max}$ has only a small effect on the results and is set to unity if not mentioned otherwise. The direction of the potentials is set up in such way, that the expected long-time 'main velocity' is positive and the long-time 'inverse velocity' (if present) is negative.[1] Potentials are changing in time in stochastic, deterministic or smoothly varying manner, as explained in Section 3.1.

[1]Note that in Article I the main velocity has a negative sign and the inverse velocity is positive, whereas in Article II is it other way around. Here we have made a compromise by plotting $-v$ and $-d$ in some figures.

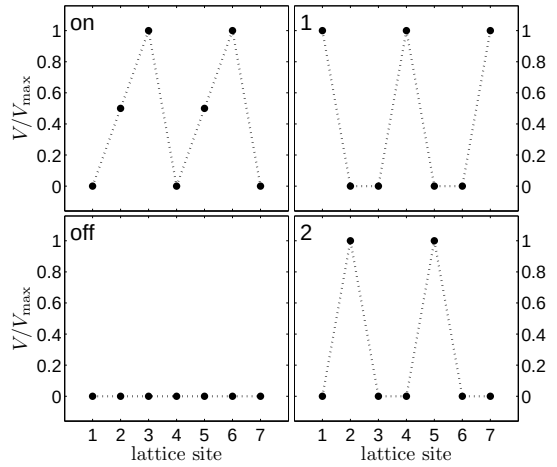

Figure 6.1: Sketch of a flashing non-symmetric ratchet (left columns) and the traveling symmetric ratchet (right columns) for $L = 3$ (two period lengths shown). In these potentials, the chosen main velocity direction is on the left.

6.1 Choosing the rates

As discussed in Section 2.2.2, the selection of rates is important for the nonequilibrium systems. To demonstrate this, in Fig. 6.2 we have plotted the steady state velocity and diffusion coefficient of the 8-repton RD polymer in a stochastic flashing ratchet and traveling potential. Although all three curves for flashing and traveling potentials share a similar shape, the scales are different and large differences can be seen in the limit where the temporal period $\tau \to 0$. Only exponential (in a flashing ratchet) and Metropolis (in a traveling potential) dynamics lead to zero drift in this limit, which is a physically expected situation (see Section 3.1.3) and is also consistent with the single Brownian particle models [12, 109, 155]. Therefore we choose these rates for the repton model.

6.2 Relaxation in a flashing ratchet

First we study the relaxation process of the repton model in a flashing ratchet potential depicted in the left column of Fig. 6.1. In Fig. 6.3, we have plotted the time-dependent velocities of 10-repton polymers during their relaxation, when the potential state is switched at $t = 0$ and the polymer is in equilibrium at $t < 0$ with zero average velocity $v(t < 0) = 0$. In Fig. 6.3(a), the uniformly charged RD and FM polymers are compared (the total charge $Q = 10$). The time-dependent total displacement of the

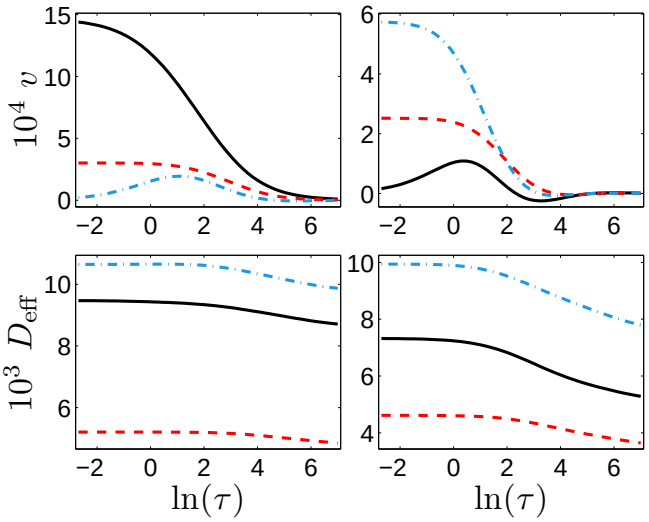

Figure 6.2: The effect of the jump rate scheme. The velocity and the diffusion coefficient of the 8-repton RD polymer as a function of the temporal period τ in a stochastic flashing ratchet with $L = 3$ and $V_{\max} = 1$ (left) and the traveling potential (right), with exponential (blue dash-dotted lines), Metropolis (black solid lines), and Kawasaki (red dashed lines) rates.

center-of-mass,

$$d(t) = \int_0^t [v_{\mathrm{on}\to\mathrm{off}}(s) + v_{\mathrm{off}\to\mathrm{on}}(s)]\, ds,$$

is shown in the inset figure. The asymptotic value $d := d(\infty)$ was previously discussed in Section 3.1.3. For rigid objects without internal configurations and without deformable shapes, clearly $v_{\mathrm{on}\to\mathrm{off}}(t) \equiv 0$ because there is no directed center-of-mass motion for $t > 0$. However, for other objects there is a non-zero relaxation time related to the internal configurations of the object, hence $v_{\mathrm{on}\to\mathrm{off}}(t)$ is generally non-zero. We call this relaxation a *rebound effect*. For the repton model in a flashing ratchet, it is found that $v_{\mathrm{on}\to\mathrm{off}}(t)$ has an opposite sign compared to $v_{\mathrm{off}\to\mathrm{on}}(t)$, which is considered as the main velocity. As noted in the beginning of this Chapter, we have chosen the directions such that $v_{\mathrm{off}\to\mathrm{on}}(t) > 0$ is expected.

The rebound effect is much stronger for the RD polymers, and with combined effect of the weaker main velocity, causes the current inversion, where the long-time velocity is negative (*i.e.* the polymer travels 'backwards'). For the FM model, the rebound effect is generally too weak to allow current inversion. One can also notice the much faster relaxation of the FM model. In Fig. 6.3(b) the effect of non-uniform charge distribution is shown for the RD model with total charge $Q = 6$.[2] All the charge put

[2]To study polymers with a single charged repton, the total charge cannot be too large, otherwise the master equation set becomes stiff.

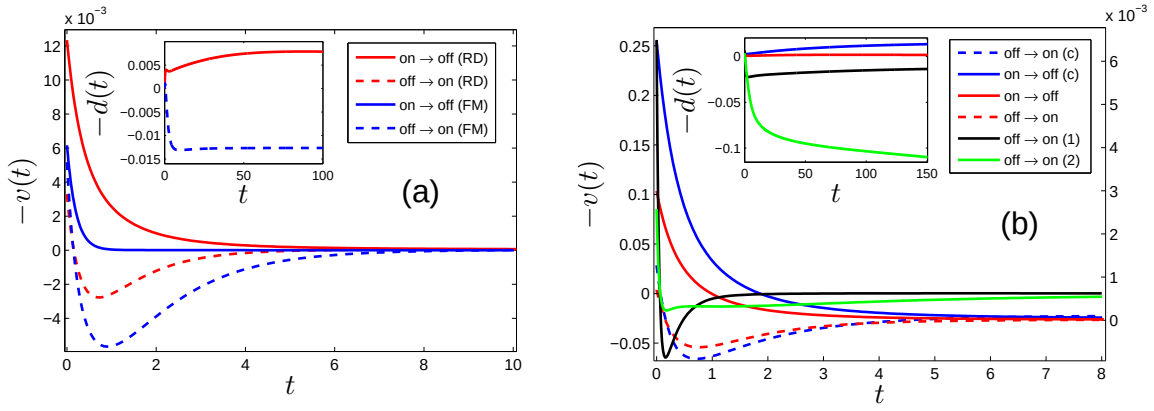

Figure 6.3: The velocity after the potential is switched at $t = 0$ for a deterministic flashing ratchet at the large τ limit. (a) RD (red lines) and FM (blue lines) polymers with homogeneous charge distributions and a total charge $Q = 10$. (b) RD polymers using a middle-centered (blue lines), homogeneous (red lines), the first repton (black line) and the second repton (green line) charge distributions with $Q = 6$. Note the different y-axis used for the black and green lines, because of the large scale difference. In both figures $N = 10$, $L = 3$ and $V_{\max} = 1$. The integrated total displacement is shown in inset figures.

into a single repton leads to a large drift towards positive direction, since the rebound effect is non-existing. This is because all internal states have an equal probability, hence there cannot be net velocity when the potential is turned off. Although the head-charged polymer (repton 1 or 6 in Fig. 4.1) is faster shortly after the potential is turned on, the polymer with the second repton charged (*i.e.* repton 2 or 5 in Fig. 4.1) produces a larger total displacement due to the longer relaxation process. On the other hand, the rebound effect can be maximized by concentrating the charge on the middle reptons. In this example, total charge was distributed according to percentages $[0, 5, 10, 15, 20, 20, 15, 10, 5, 0]$ for $q_1, \ldots, q_{10}$. The reason for such a distribution becomes evident later in Section 6.4.

In Fig. 6.4, similar data is shown for the case $L = 6$ so, that when the potential is turned on, its profile remains identical to the case $L = 3$, but the scale is doubled (*i.e.* lengths of the slopes are 4 and 2 steps). Now the rebound effect is not enough to cause current inversion for neither RD nor FM polymers. Despite the stronger rebound effect, using the middle-centered charge distribution actually leads to increased velocity in the main direction. This is caused by the very slowly decaying velocity into the main direction.

Next we take a closer look at the travel distance $d(t)$ of the center-of-mass during a single, very large time-period τ of a flashing ratchet. The results for (a) $L = 3$ and (b) $L = 6$ are shown in Fig. 6.5. For $N = 1, 2$, there are no bulk-reptons, so the mean travel distances of RD and FM polymers may differ for $N \geq 3$ only. For the $L = 3$, the calculation reveals that for long RD polymers ($N > 5$, a 'critical length') the rebound

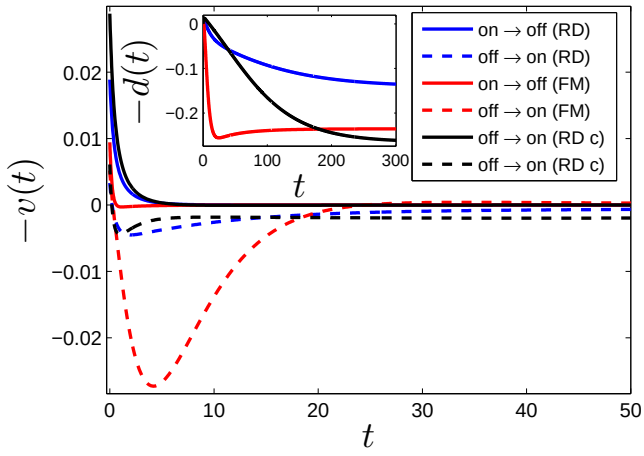

Figure 6.4: The velocity after the ratchet potential is switched at $t = 0$ for a deterministic flashing ratchet at the large τ limit. Blue and red lines are for the homogeneously charged RD and FM polymers, and black lines for the middle-centered charged RD polymer. The data is for $N = 10$, $L = 6$, $V_{\max} = 1$ and $Q = 10$.

effect wins (*i.e.* $d < 0$) and the polymer starts traveling backwards, while the single particle and all FM polymers are traveling to the expected positive main direction. The rebound effect is also present in FM polymers, but it is not strong enough to reverse the direction of the velocity.

For the case $L = 6$, polymers up to 11 reptons can be treated with exact numerics, whereas time-dependent DMRG is used for larger ones. The asymptotic limit $d(\infty)$ can be reach only with the exact numerics. The results for DMRG are limited up to $d(200)$ because of the high computational cost.[3] Time-steps of $\Delta t = 0.05 \ldots 0.07$ and error tolerance 10^{-9} were used. Unfortunately, the velocity is a very slowly decaying function for the 'off-on' process and a notable difference between $d(200)$ and $d(\infty)$ remain. From the behavior of $d(t)$, one can however assume that $d(t = \infty)$ remains always smaller than $d(t)$ with finite values of t and large RD polymers. Based on this and our Monte Carlo simulations for large τ's (data not presented here), we may conclude that the current inversion does not occur for uniformly charged RD polymers in the case $L = 6$. Similar results were also found for $L = 4$ and $L = 5$, hence the case $L = 3$ seems a special case for the RD model. Using non-uniform charge distribution, d becomes closer to zero, but still remains positive for $L = 6$. However, since optimal charge distributions are not known for large RD polymers and d approaches zero as the polymer gets larger, current inversion still cannot be completely ruled out for very large polymers $N > 25$ with optimal charge configurations. One could also try to reinforce the rebound effect by adding longer-range interactions (*e.g.* stiffness) between reptons which might also lead to current inversion for $L > 3$.

[3]These results required already more than a month of uninterrupted parallel computing to finish.

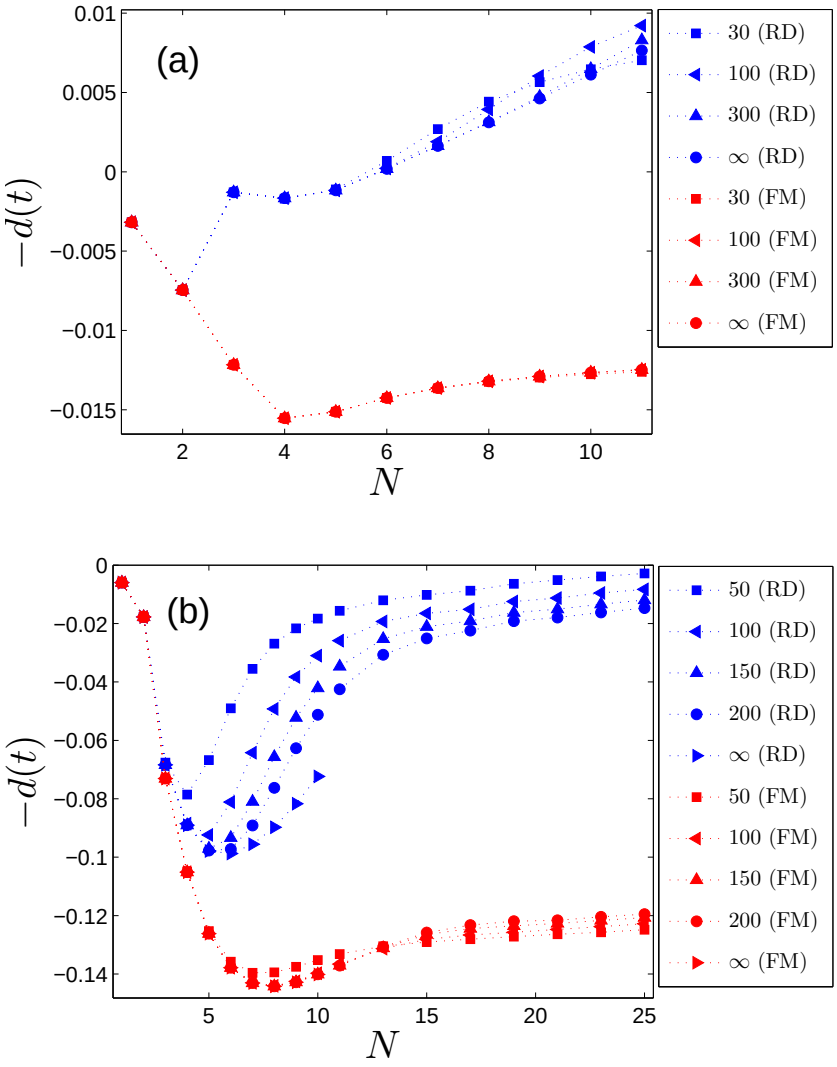

Figure 6.5: (a) Expected travel distances $d(t)$ of the RD polymers (blue lines) and FM polymers (red lines) in a deterministic flashing ratchet ($L = 3$ and $V_{\max} = 1$) as a function of the polymer length in single time-period at asymptotic limit (*i.e.* the steady state is reached before the switching). Different t's are indicated with different marker types. (b) The similar data for $L = 6$. Polymers up to $N = 11$ were computed with exact numerics and larger ones with time-dependent DMRG. The asymptotic limit $d(t = \infty)$ is reached only using exact numerics.

6.3 Velocity and diffusion in the steady state

6.3.1 Flashing ratchet

We fix the symmetry parameter $x = \tau_{\text{off}}/\tau$ to $x = 1/4,\ 1/2,\ 3/4$ and examine the τ dependence of the steady state velocity v and the Peclet number $\text{Pe} = |v|/D_{\text{eff}}$ in stochastic potentials. The results in Fig. 6.6 reveal a complex behavior of the velocity. The overall form of the curves is as expected: the velocity and the Peclet number have some (local) maxima around $\ln(\tau) \approx 0$. For small τ, the single particle remains the fastest in all cases excluding $x = 1/2$ for FM polymers, where it is the slowest one. However, as τ gets larger, longer polymers eventually become faster, which is caused by their longer relaxation time (short polymers have already reached their steady state). This can be clearly seen from Figs. 6.6(b) and (c), but it also takes place in figure (a) to some extent. Similar behavior of coupled particles being faster than single ones and also having current inversions were also reported in Ref. [100]. Although the relaxation times are quite different, the maxima of the velocity fall close to $\ln(\tau) \approx 1$ for all polymer lengths and the position of the maximum Peclet number is almost constant. The velocity sign change occurs for some polymers when τ is very large or when τ is small and $x > 1/2$.

The behavior of the Peclet number is very clear and similar in every case: the larger the polymer, the larger the Peclet number. Thus the transport of longer polymers is more coherent than that of shorter ones. Similar behavior was found in a continuum model consisting of elastically coupled Brownian particles [187]. By comparing the values of the Peclet number between polymer types, we see no significant differences between the curves. There is a slight difference for large values of τ, where the Peclet number remains larger for FM polymers. This holds with every choice of parameters, excluding the possible current inversion points (*e.g.* the interval $\ln(\tau) = -1 \ldots 0$ in Fig. 6.6(c)).

Next we compare the differences of the three potential time-dependency schemes (stochastic, deterministic and smoothly varying) in a flashing ratchet potential, for which the differences are more distinct. In Fig. 6.7 we have plotted v and the Peclet number of $N = 5$ and $N = 9$ (similar behavior is observed for other values of N) RD and FM polymers as a function of τ for all three time-dependency schemes. Some clear differences between the schemes can be seen. The maxima for the velocity and the Peclet numbers are reached for smaller τ for the stochastic scheme than for two others. The deterministic scheme has the largest v and the smoothly varying the smallest, and the same goes for Pe. However, this order changes for the inverse velocity, where deterministic and smoothly varying schemes are equally good. The time-dependency scheme turns out to have an effect on the current inversion phenomena, since the smoothly varying scheme is able to invert all RD polymers with $N > 2$, whereas

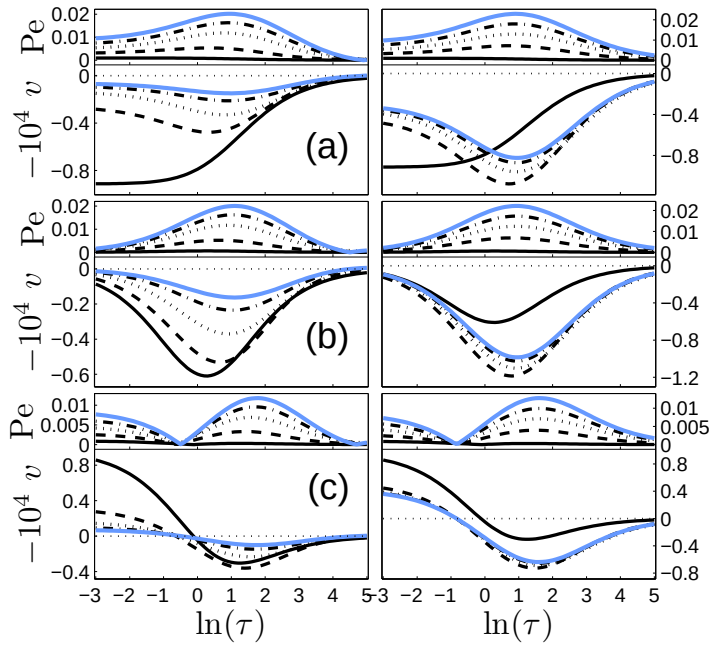

Figure 6.6: Velocity and Peclet numbers of the RD polymers (left column) and FM polymers (right column) in a flashing ratchet ($L = 3$, $V_{\max} = 1$) with $N = 1$ (solid black), $N = 3$ (dash), $N = 5$ (dot), $N = 7$ (dash-dot), $N = 9$ (solid blue). The value of the symmetry parameter $x = \tau_{\text{off}}/\tau$ is (a) $x = 1/4$, (b) $x = 1/2$ and (c) $x = 3/4$.

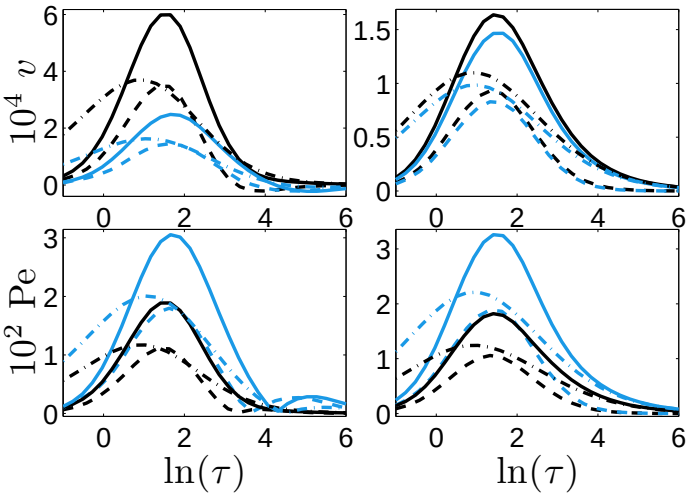

Figure 6.7: Velocity and Peclet number for 5 (blue lines) and 9-repton (black lines) RD (left) and FM polymers (right), for deterministic (solid lines), smoothly varying (dashed lines), and stochastic (dash-dotted lines) schemes.

stochastic and deterministic only those with $N > 5$. Despite this, the differences between deterministic and smoothly varying are small (deterministic being slightly 'better').

6.3.2 Traveling potential

Next we study transport in the stochastic traveling potential depicted in the right column of Fig. 6.8. For this potential the symmetry parameter is $x = \tau_1/\tau$. A Similar velocity and diffusion behavior as previously reported in Ref. [109, 26] for a single particle is expected. In Fig. 6.8, we show v as a function of x with three different τ's (Fig. 6.8(a)-(c)): $\tau \to 0$, $\ln(\tau) = 3$ and $\ln(\tau) = 7$. The behavior for the single particle is as expected; the velocity is antisymmetric with respect to $x = 1/2$ and goes to zero at $x = 0,\ 1/2,\ 1$. With longer polymers the velocity changes sign non-trivially for large τ (Fig. 6.8(c)) for both polymer types. This result is unexpected. An example of the behavior of the diffusion coefficient is shown in Fig. 6.8(d) for $N = 9$ and different τ's. D_{eff} always reaches its maximum at $x = 1/2$ and decreases as the system goes to a static potential state at $x = 0$ and 1.

Next we fix $x = 1/4$ and examine the τ dependence in detail. In Fig. 6.9, we have plotted v and the Peclet number for $\ln(\tau) = -4 \ldots 7.5$. As $N > 2$, current inversions can be seen around $\ln(\tau) \approx 2$ for both polymer types. As before, the single particle remains the fastest for small τ, but eventually the velocity curves begin to intersect

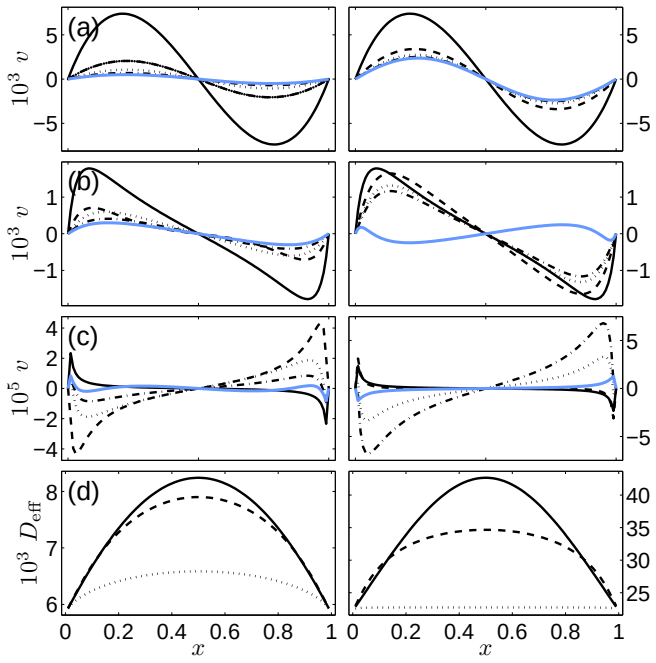

Figure 6.8: Velocity and Peclet numbers of the RD polymers (left column) and FM polymers (right column) in the traveling potentials ($L = 3$, $V_{\max} = 1$). (a-c): velocity as a function of the symmetry parameter $x = \tau_1/\tau$ with $\tau \to 0$ (a), $\tau = \exp(3)$ (b) and $\tau = \exp(7)$ (c) with $N = 1$ (solid black), $N = 3$ (dash), $N = 5$ (dot), $N = 7$ (dash-dot), $N = 9$ (solid blue). (d): the effective diffusion coefficient for $N = 9$ with $\tau \to 0$ (solid), $\tau = \exp(3)$ (dash) and $\tau = \exp(7)$ (dot).

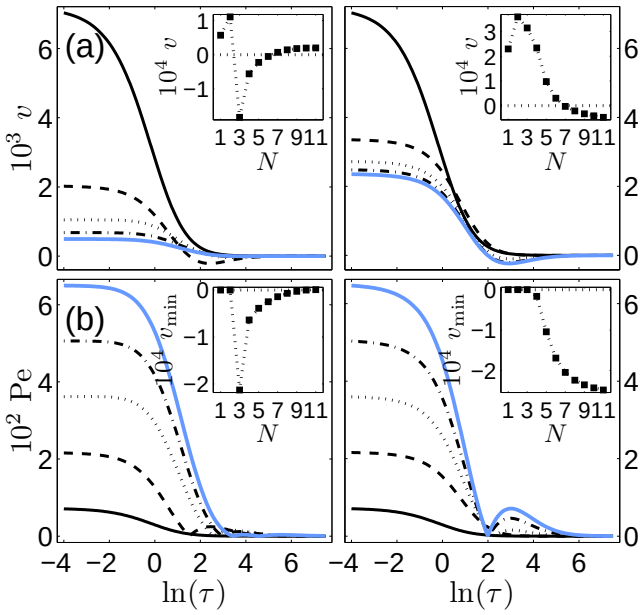

Figure 6.9: Velocity and Peclet numbers of the RD polymers (left column) and FM polymers (right column) in the traveling potential ($L = 3$, $V_{\max} = 1$) as a function of the mean time-period τ with the symmetry parameter $x = \tau_1/\tau$ and $N = 1$ (solid black), $N = 3$ (dash), $N = 5$ (dot), $N = 7$ (dash-dot) and $N = 9$ (solid blue). For the left inset of (a) $\ln(\tau) = 2.85$ and $\ln(\tau) = 2.05$ for the right inset.

as τ gets larger and the single particle is not always the fastest (see *e.g.* the $N = 3$ FM polymer in Fig. 6.9(a), right column). The behavior of the Peclet number is as before: Longer polymers have more coherent transport, excluding the possible current inversion points and their neighborhood. With small values of τ, the Peclet number is also the same for both polymer types, but because of unequal velocities for moderate and large values of τ, also differences exist.

The insets of Fig. 6.9 show the velocity as a function of $N = 1 \ldots 11$ in detail. We have chosen $\ln(\tau) = 2.85$ for RD polymers and $\ln(\tau) = 2.05$ for FM polymers. With these choices, the current inversion occurs between $N = 6$ and 7 for both models. In the insets of Fig. 6.9(b) we have plotted the overall velocity minimal values in the interval $\ln(\tau) = -4 \ldots 7.5$ as a function of N. The distinction between the polymer types is very clear. FM polymers travel increasingly fast backwards whereas RD polymers eventually stop moving as N gets larger. The current inversion of the RD polymers $N \geq 10$ would require a smaller fixed x.

The magnitude of the velocity, typically between 10^{-5} and 10^{-3}, is comparable with the velocity caused by a flashing ratchet. The Peclet number values of the polymer motion remain small ($\ll 0.1$) for both potential types, indicating very low coherence of transport.

6.4 Non-uniform charge distributions

We now consider non-uniform charge distributions where the charges of the reptons differ. As already seen for the relaxation studies, changing the charge distribution has a dramatic effect on the velocity. To set up the optimization problem, we define constraints $\sum_{i=1}^{N} q_i = Q$, $q_i \geq 0$ and $\tau \geq 0$. The objective function is the velocity $v(q_1, q_2, \ldots, q_N, \tau)$. Some additional technical details and comparison of methods were discussed in Section 5.2.2.

Using the SQP method, extensive computations were carried out to find the charge configurations with the largest possible velocity in main (forward) and inverse (backward) transport directions and Pe for various polymers and parameters. It was found that changes in the velocity are so large that one can safely limit to maximizing v alone, since in this case Pe is dominated by the velocity. In the following, some of the optimization results are presented for the 8-repton polymers with $Q = 8$ in the stochastic potentials with $V_{\max} = 1$ and $L = 3$. The data for the basic model with an uniform charge distribution (*i.e.* $q_i = 1 \,\forall\, i$) is also shown for comparison. Note that since reptons are equal in the sense that their charge is allowed to vary between $[0, Q]$, a non-symmetric distribution is equal with its mirror-symmetric counterpart with respect the center bond (or repton, if N is odd). In the figures, only one of such distributions is shown. For symmetric charge configurations, such as uniform and middle-centered, the solution is unique.

In Fig. 6.10, the properties of the RD polymer in a flashing ratchet are plotted as a function of τ with configurations that give maximum velocities in positive (main) and negative (inverse) directions, and the corresponding optimization results are called either positive or negative. We found that the velocity in the positive direction is always maximized by putting all charge near either of the heads, but charging the head reptons does not necessarily lead to the largest current. This holds for both RD and FM polymers for all studied polymer lengths up to $N = 13$ at least. In this situation, only one repton feels the potential and very large transition rates are generated by the exponential function. This one repton then forces the whole polymer to advance. As discussed in Section 6.2, there is no rebound effect when only one repton is charged.

The optimal charge distributions in the negative direction are more interesting, since no large accumulation of the charge is seen, and the charge is distributed over several reptons. A symmetric distribution means that neither of the heads is leading and the heads are forced to compete with each other. This would be very inefficient in constant-field transport. Depending on the value of $V_{\max}$, other slightly different local optimal distributions are found. In Section 6.2, it was demonstrated that the rebound effect is strong for the RD polymers with a middle-centered charge distribution.

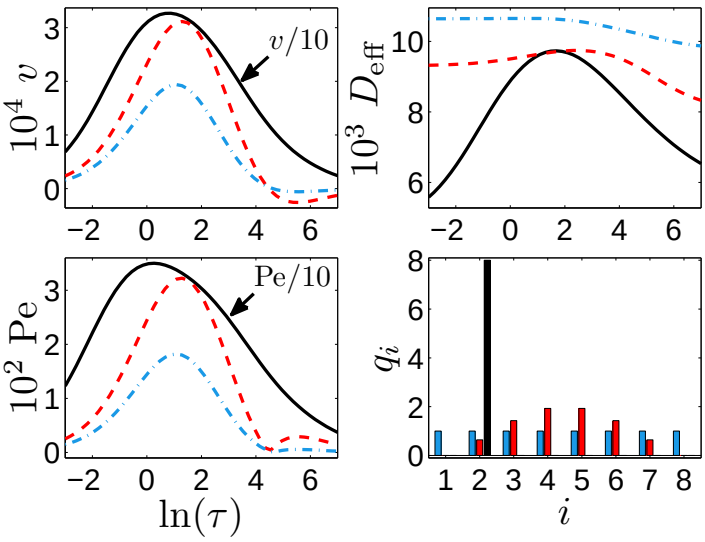

Figure 6.10: Velocity, diffusion coefficient and Peclet number for the 8-repton RD polymer in a flashing ratchet with uniform (blue dash-dotted lines), negatively optimized (red dashed lines), and positively optimized (black solid lines) charge distributions as a function of the temporal period τ. The histogram shows the charge distribution along the polymer for each case in the same order. In the leftmost figures v and Pe for the positively optimized case have been scaled by an additional factor 1/10.

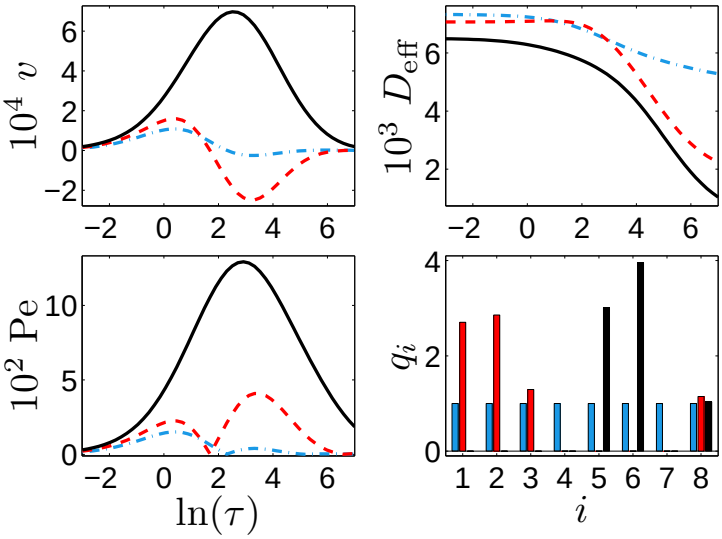

Figure 6.11: Velocity, diffusion coefficient and Peclet number for the 8-repton RD polymer in the traveling potential with uniform (blue dash-dotted lines), negatively optimized (red dashed lines), and positively optimized (black solid lines) charge distributions. The histogram shows the charge distribution for each case in the same order.

In Figs. 6.11 and 6.12, we show the same analysis for the traveling potential. For RD polymers, the optimal distributions have no 'clear' or symmetric structure. As in the case of a flashing ratchet, the negatively optimized polymers are actually faster than uniformly charged polymers in both direction.

In conclusion, the charge distribution has a large effect on the polymer transport velocity and coherence on the flashing and traveling potentials. Since the velocities generated by the ratchet effect are generally very small and difficult to observe, this could be of interest from the point of view of applications.

6.5 Efficiency of the transport in a flashing ratchet

In Figs. 6.13 and 6.14, we show the maximum efficiency $\eta_{\max} = \max(\eta(\tau))$ of the RD and FM polymers as a function of a load force $F = \sum_{i=1}^{N} Eq_i$, where E is the field strength, with flashing ratchets and traveling potentials of the stochastic and deterministic type. The points where $\eta_{\max}(F) = 0$ for $F > 0$ define the stopping forces F_{stop}. Insets of the figures show the same data scaled with $F^* = F/F_{\mathrm{stop}}$ and $\eta^*_{\max} = \eta_{\max}(F^*)/\max \eta_{\max}(F^*)$ for each polymer size, which reveal the shapes of the curves.

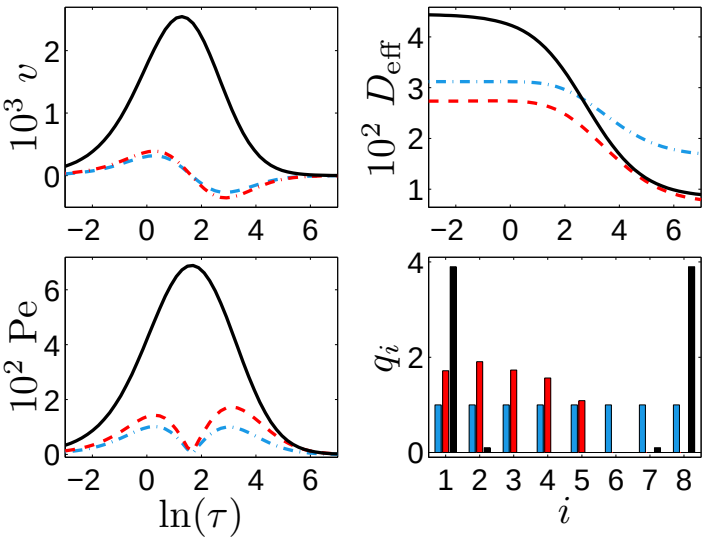

Figure 6.12: Velocity, diffusion coefficient and Peclet number for the 8-repton FM polymer in the traveling potential with uniform (blue dash-dotted lines), negatively optimized (red dashed lines), and positively optimized (black solid lines) charge distributions. The histogram shows the charge distribution for each case in the same order.

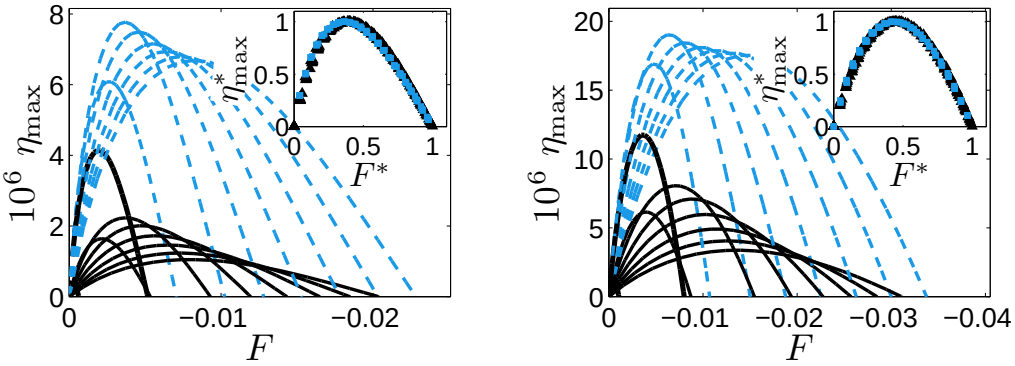

Figure 6.13: Maximum efficiency for RD (black solid lines) and FM (blue dashed lines) polymers as a function of the load force F with $N = 1...9$ in stochastic (left) and deterministic (right) flashing ratchets. In each case, the rightmost curve is for $N = 9$ and the bold lines (the less interesting special cases $N = 1, 2$) are shared for both RD and FM polymers. Insets: Rescaled data $\eta^*_{\rm max}$ as a function of F^*, with black triangles for RD polymers and blue squares for FM polymers.

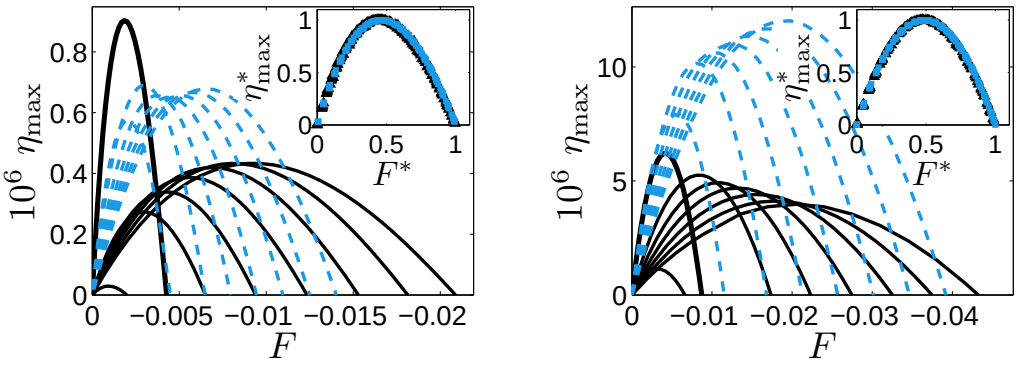

Figure 6.14: Maximum efficiency for RD (black solid) and FM (blue dashed) polymers as a function of the load force F with $N = 2...9$ in stochastic (left) and deterministic (right) traveling potentials. In each case, the rightmost curve is for $N = 9$ and the bold lines (the less interesting special case $N = 2$) are shared for both RD and FM polymers. Insets: Rescaled data $\eta^*_{\max}$ as a function of F^*, with black triangles for RD polymers and blue squares for FM polymers.

We notice that for the FM polymers the efficiency is generally larger and they can maintain their velocity in an opposing field better than the RD polymers in a ratchet. When plotted as a function of E, there is a constant stopping field for all $N > 3$ FM polymers in both potentials with values around $-0.0026/-0.0016$ for stochastic and $-0.0038/-0.0043$ for deterministic ratchet/traveling potentials. This results from the fact that the reptons of the FM polymer are less correlated than those of the RD polymer and reptons in a FM polymer thus behave more independently . For a ratchet, the deterministic scheme is found to be 2-4 times more efficient and can withstand almost a double load force when compared with the stochastic. The stopping force is larger for FM polymers. For the traveling potential, differences are more drastic, as for the deterministic scheme the stopping force is about two times and the efficiency almost one order of magnitude larger when compared to the stochastic scheme. Rescaled curves reveal that despite the large differences in scales, shape of the curves are almost identical for all polymer lengths and both types.

The numerical values of the efficiency are very small. This is a generally known trait especially for flashing ratchet models [132], but it also results from the choice of the rates, since the velocity plays dominating role in efficiency. By using the optimized values for $V_{\max}$, x, and $\mathbf{q}$, the efficiency could be increased by a couple orders of magnitude. Results show that F_{stop} increases as a function of N, which is in agreement with some previous work [54, 169]. The efficiency $\eta_{\max}$, however, decreases as the polymer gets longer for all other but a stochastic traveling ratchet, which is surprising.

6.6 Time-evolution of observables

To gain better insight in the internal dynamics of the polymer, we now turn to the expected values of the four observables Z (zero-bond), G (total length), K (kinks) and H (head-to-head distance) for the RD polymer. In Figs. 6.15 and 6.16 we have plotted the steady state time-evolution of the observables against each other with the 8-repton RD polymer in a deterministic ratchet and traveling potentials with several values of τ. The previously found optimized charge distributions are used. Note that these distributions are only *approximately* optimal for the deterministic potentials, but this approximation is found to be very good. For small τ, the observables are near their mean-field values (large spots in the figures), which are independent of t. For very large τ, the curves 'freeze' (bold lines) since the steady states are reached before the potential is switched.

For a ratchet, the maximum positive velocity (black lines) is a result of small changes in the polymer average shape, which is caused by the fact that only a single near-head repton is charged and the rest of the polymer is in pure random motion. The maximum negative velocity (red lines), however, is a result of more complex processes, which cause much more variation in the average shape, even more than for a polymer with uniformly distributed charges (blue lines) with all the reptons charged.[4] There is almost one-to-one correlation between $G-H$ pair (as expected), which results that the phase trajectories for the $G-Z$ and $H-Z$ pairs are almost indistinguishable, and therefore the pairs $G-H$ and $G-Z$ are not presented here. The connections between other pairs are more involved, especially between $H-K$ and $G-K$. For them, the current inversion is seen as a deformation of loops between $K-Z$, $H-K$ and $G-K$ pairs for uniform and negatively optimized polymers (no current inversion for positively optimized polymer).

For the traveling potential, the curves are more distinguished from each other and are more complicated. There are fast deformations in the curves as the time goes on. There is a clear similarity between Figs. 6.15 and 6.16. Positively optimized polymers have the smallest spread in the observables and negatively optimized the largest. This is similar behavior as seen for a flashing ratchet, albeit the potential and the charge distributions are very different. The results show that there is a clear connection between the average polymer velocity magnitude and direction, and shape deformations. Deformations during ratcheting for one's part depend strongly on the charge distributions.

In Figs. 6.17 and 6.18 we have plotted the relaxation as a function of time of the observables in a flashing ratchet and the traveling potential for the 8-repton RD

[4] In Article II, there is a misprint with the red and blue color codes, as they should be other way around. The color coding given here, is the correct one.

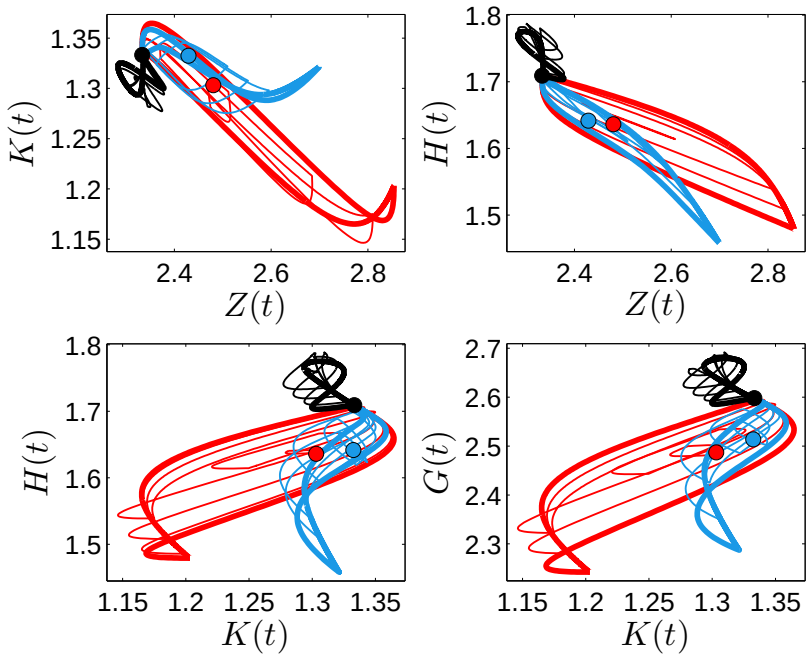

Figure 6.15: Time evolution of the 8-repton RD polymer observables in a deterministic flashing ratchet with uniform (blue lines), positively optimized (black lines) and negatively optimized (red lines) charge distributions. In each case, the big spots correspond to the (mean-field) limit $\tau \to 0$, the bold curves show the $\tau \to \infty$ limit and the other curves the behavior for a few selected finite values of τ.

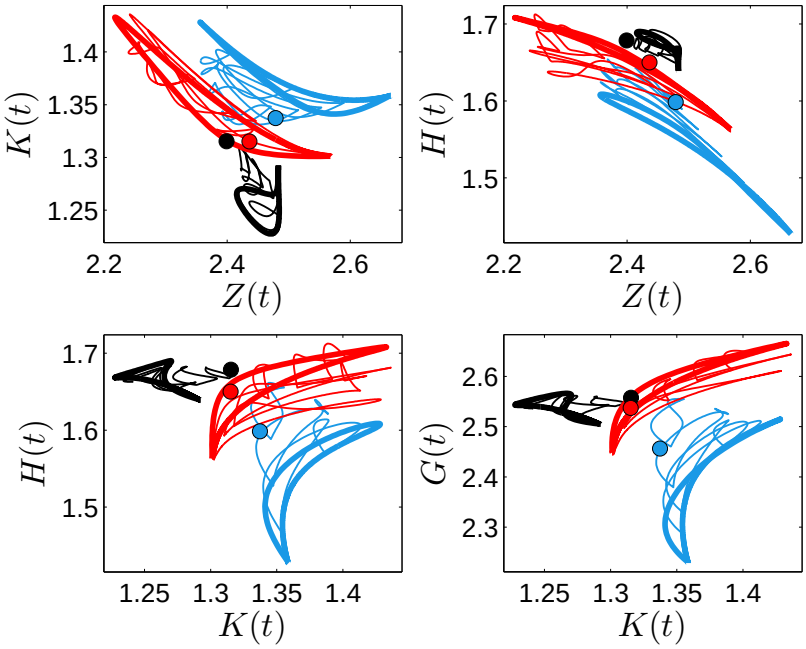

Figure 6.16: Time evolution of the 8-repton RD polymer observables in the deterministic traveling potential with uniform (blue lines), positively optimized (black lines) and negatively optimized (red lines) charge distributions. In each case, the big spots correspond to the (mean-field) limit $\tau \to 0$, the bold curves show the $\tau \to \infty$ limit and the other curves the behavior for a few selected finite values of τ.

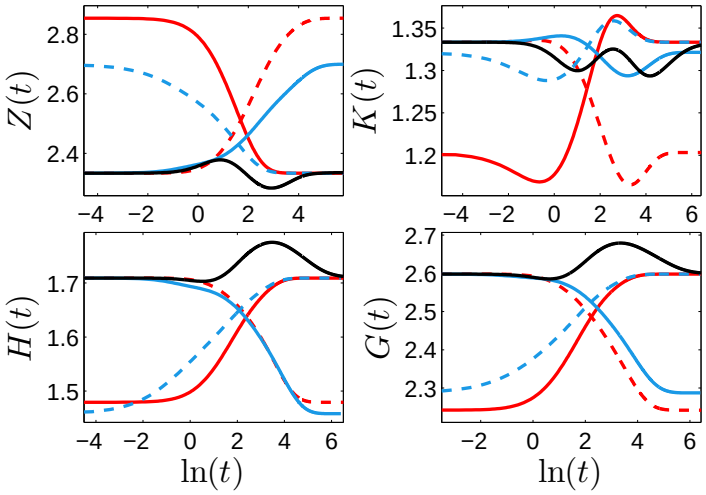

Figure 6.17: Relaxation in real time t of the 8-repton RD polymer in a deterministic ratchet potential, with uniform (blue line), positively (black lines) and negatively (red lines) optimized charge distributions. Dashed lines (when present) are for the 'on → off' and solid ones for the 'off → on' processes.

polymer with uniform and optimized charge distributions. The data is the same as shown in Figs. 6.15 and 6.16 for the large τ limit (bold lines). The largest changes are observed in roughly the same time scale, around $\ln(t) \approx 2$, for all observables. Steady state values of observables for the positively optimized polymer in a flashing ratchet are independent of the potential state (on or off). In addition to the kink dynamics, large differences are seen in zero-bond dynamics. Note that for positively optimized polymer, values remain unchanged during 'on → off' switching and are therefore not shown in the figure. This is because, in the steady state, the potential has no effect on the conformations of the polymer, which would require more than one charged repton. For the traveling potential, the time-evolution of the observables is more complex.

6.7 Transition sequences

We now turn to the dominating transport cycles of the polymer motion using measures (5.3) and (5.5) for γ, with the weight function f given by the center-of-mass displacements. It is found that the common transportation type is what we call the 's_1-s_2-scheme' consisting of cyclically accumulated (lengths s_1 and s_2 with $|s_1 - s_2| = 1$) and elongated parts of the polymer. Corresponding to the direction of moves, this scheme can be either positive (up) or negative (down). To illustrate the scheme, we have sketched the positive 4-5 scheme in Fig. 6.19. The numbered arrows indicate the order and direction of the corresponding repton moves. After all marked moves are

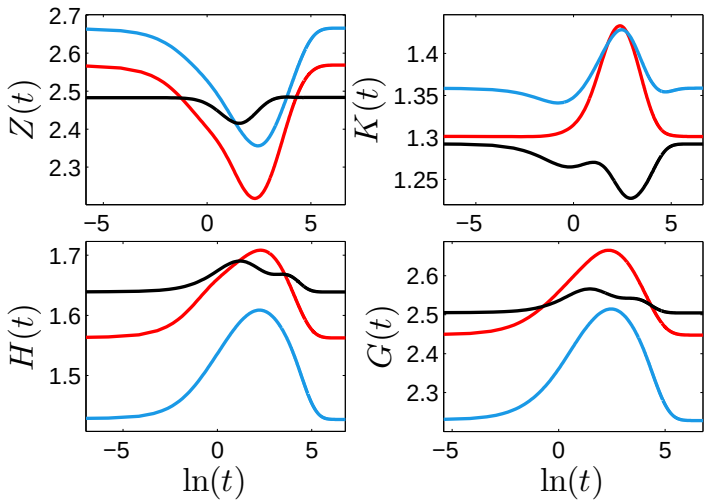

Figure 6.18: Relaxation in real time t of the 8-repton RD polymer in the deterministic traveling potential, with uniform (blue line), positively (black lines) and negatively (red lines) optimized charge distributions.

done, the initial state is recovered and the cycle is repeated. We concentrate on eight different situations for the RD polymer: transport in positive and negative directions in a ratchet and traveling potential, using uniform and optimized charge configurations (*i.e.* $2 \times 2 \times 2 = 8$). In the five cases out of these eight, the dominating transport process is the s_1-s_2-scheme.

In Fig. 6.20 we show the remaining three situations that are not of the type above. Note that for negative transport in a ratchet with the uniform charge distribution, the mechanism is almost the 4-5-scheme.

In Table 6.1, we have collected the core results of this subsection. The last column lists the ratios of average cycle velocities v_c per edge, divided by the average velocity for all transitions $v_{\text{all}} = v/5832$, where 5832 is the total number of edges in the directed graph G (see Section 5.2.1). This ratio is significantly larger for uniformly charged polymers, indicating that the optimization process increases the velocities in a large number of paths and makes differences between paths smaller. It is also somewhat surprising that there is not much difference between the dominating mechanisms for forward or backward motion, and for uniformly charged polymers in a ratchet they are actually the same. One can therefore conclude that the current inversion for the RD model is not caused by some abrupt 'phase transition', but by gradual changes in the probability distribution along internal states.

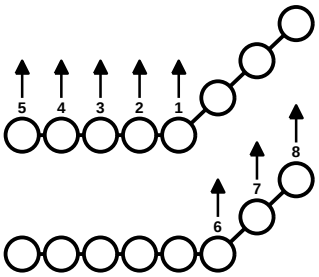

Figure 6.19: Illustration of the positive 4-5-scheme for the 8-repton polymer. The arrows and numbers indicate the direction and the order of the transition for the corresponding reptons. For clarification, the process is shown here in two parts.

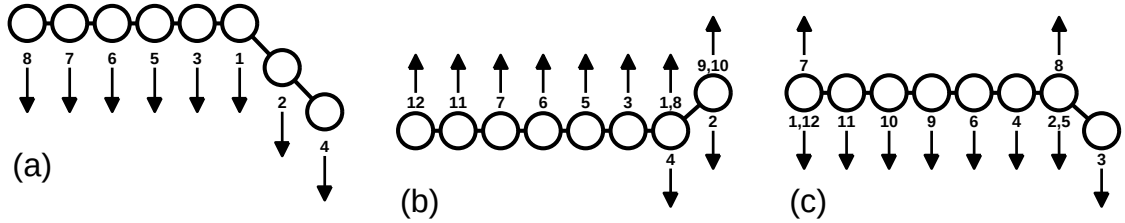

Figure 6.20: Dominating transport cycles for the inverse velocity in the traveling potential ($L = 3$ and $V_{\max} = 1$) with (a) the uniform charge distribution, (b) the main velocity in the traveling potential with the uniform charge distribution, and (c) the backward velocity in a ratchet with the optimal charge distribution.

Table 6.1: Dominating transport cycle types for polymers in ratchet and traveling potentials for forward (F) and backward (B) transport, with uniform (unif.) and optimized (optim.) charge distributions.

Case	Cycle	v_c/v_{all}
Ratchet potential		
unif. F	pos. 4-5	46,4
unif. B	neg. 4-5	554
optim. F	pos. 2-3	6,5
optim. B	Fig. 6.20(c)	164
Traveling potential		
unif. F	Fig. 6.20(b)	60,0
unif. B	Fig. 6.20(a)	371
optim. F	pos. 2-3	29,4
optim. B	neg. 1-2	91,3

6.8 Discussion

We have studied reptation of polymers in time-dependent potentials by analyzing the master equations of pure and modified Rubinstein-Duke model. We found complex dynamics that results from the non-pointlike structure of the polymers by the coupling between the potential and polymer internal states.

By varying the temporal period τ of flashing ratchet and traveling potentials, we found non-trivial inversions of the polymer drift direction, which cannot occur with pointlike particles. The Peclet number grows as the polymer gets longer and is largely independent of the polymer type, thus allowing more coherent transport for longer polymers. The overall polymer dynamics in ratchet potentials was found to be very model specific. It was found that a deterministically flashing potential is superior compared to a smoothly or stochastically varying potential in terms of velocity, coherence and energetic efficiency. However, despite the scaling in velocity and diffusion, the time-dependency scheme of the potential only has a minor effect on the qualitative results.

By using the stochastic potential scheme, we computed the optimal charge distributions to maximize the steady state velocity in flashing ratchets and traveling potentials. The differences in transport properties and dynamics between these and the uniformly charged polymers were found to be drastic. By studying the relaxation in ratchet potentials, it was found that non-uniform distributions cause very slow or fast velocity relaxation depending on which transport direction was preferred. Changing the charge distribution also changes the mechanism of how the polymer reshapes itself with respect to the potential. This mechanism either amplifies or reduces the 'rebound' effect that is responsible for the current inversion of the RD polymers in a flashing ratchet with $L = 3$ and large τ for polymers with more than 5 reptons. This type of current inversion was not found with other types of flashing ratchet potential.

The current inversion phenomenon was investigated by using the optimal charge distributions which were found by using the numerical optimization method. The expected values of certain macroscopic observables (*e.g.* length and zero-bond count) were computed and large differences between differently charged polymers were found. The graph optimization method described in Section 5.2.1 was used to identify the dominating transport processes of the polymer transport and was found to be very useful in characterizing polymer motion. To further investigate the origins of the current inversion phenomenon, additional studies with a refined reptation model taking into account effects such as bending rigidity and excluded-volume effects, is needed.

While above results provide useful insight into the behavior of linear polymers in a ratchet potential, the nature of the model employed imposes limitations on its rele-

vance to experimental systems. Currently, no experimental data is available for direct comparison against the results discussed here. Majority of the experimental research on the ratchet effect for polymers has been for the DNA segments moving in various types of periodic potentials [13, 10]. The simple repton model cannot accurately model a real DNA in such situations. On the other hand, simple discrete dynamics is a good model for many natural [197] and artificial molecular motors [85, 93]. As the complexity of artificial motors is increasing, many-particle effects similar to those discussed here are expected to emerge (*e.g.* parallel motors).

7 Results for the island model

In this Section we present selected results from Article III for the island migration model introduced in Section 3.4. We apply both the numerical master equation method to study the ME model (also called the reduced model, see Section 3.4.2) and Monte Carlo simulations to study the MC model (the full model, see Section 3.4.1). Both of these methods have been separately used in several previous studies of islands [24, 122, 163, 183, 115, 157, 124, 153, 167, 80, 162]. We apply them both in order to utilize their strengths and also compare their differences.

We have carried out extensive computations for islands with $N < 100$ atoms. Selected MC simulations were also performed for larger islands up to thousand atoms. All results are computed with the parametrization given for Cu atoms on the Cu(001) surface. We consider temperatures $T = 400 \ldots 1000$ K and field strengths $E = 0 \ldots 0.25$ eV varying the field direction (the angle α) and the measurement direction (the angle γ). To reduce the amount of data shown below, we present detailed results for the ME model (data with better numerical accuracy) and selected results for the MC model (allowing larger islands).

For better comparison between different values of E and T in a time-dependent field, we have re-scaled τ such that $\tau = 1$ always corresponds to the largest rate available for the island. Therefore the value of τ in the figures is a multiple of the fastest rate in the system, which is the jump along the terrace in the field direction (*i.e.* $\Delta_{f,i} = 0$ and $E_{f,i} = E$ in Eq. (3.3)) and hence depends on both values E and T.

With the Monte Carlo method, all results were averaged from 100-2000 independent runs (more iterations for small islands). The approach to the steady state was confirmed from the position and geometry data. Using the geometry data, such as the perimeter length and the island width/length, was found to be important, since the actual relaxation observed through the island shape can take significantly longer than it appears from the position data alone. The initial states for the simulations were sampled from the corresponding equilibrium shapes. Since these states are generally far from the nonequilibrium steady states, the simulations quickly become difficult for large islands because of the long times needed to reach the nonequilibrium steady state. Also because of the greater migration velocity, simulations with the field direction along the axis tend to be more accurate when compared to the diagonal fields.

7.1 Pulsed field and electrophoretic ratchet

We consider two types of time-dependent fields: the pulsed field and the electrophoretic ratchet. The variation of the field is taken to be discrete, *i.e.* with two constant fields varied temporally corresponding to two sets of rates $\Gamma^k_{f,i}$ with $k \in \{1, 2\}$. The periods of the fields are τ_1 and τ_2 with the total period $\tau = \tau_1 + \tau_2$ and the symmetry parameter $x = \tau_1/\tau$.

For MC computations, the field variation is deterministic, whereas for the ME computations stochastic (Markovian type) switching is applied. These choices allow the best possible computational accuracy for both methods, avoiding serious numerical problems arising from the bad statistics of the Monte Carlo simulations or numerical integration of stiff master equation sets. This choice also allows comparison between these types of variation.

For the pulsed field, we consider the measurement angles $\gamma = 0°$ (in the direction of the coordinate axis) and $\gamma = 45°$ (the diagonal direction). The field angles are $\pm\alpha$ (for $\gamma = 0°$) and $45° \pm \alpha$ (for $\gamma = 45°$). The velocity is always positive when $0° < \alpha < 45°$. Field periods and amplitudes are taken to be identical (*i.e.* $x = 1/2$ and $E_1 = E_2$), so that the average velocity is always in the measurement direction γ (see Fig. 3.3). This type of a pulsating field is used in gel electrophoresis to increase the mobility of the DNA samples [172].

The electrophoretic ratchet, also known as a zero-integrated field, is defined by choosing $\gamma = 0°$ with α taking values $0°$ and $180°$. As the total force affecting the island is $F = 2NE/k_\mathrm{B}T$, by choosing $\tau_1 F_1 = \tau_2 F_2$ where forces F_1 and F_2 are in opposite directions, the average force integrated over time is always zero (hence the term 'ratchet'). In the (perfect) linear response regime (*i.e.* $v \propto D_\mathrm{eff} F$), this leads to zero mean velocity. Beyond that, non-zero velocity is expected. This type of time-dependent force has been previously studied in the context of electrophoresis [72, 171] and in ratchet effect studies [22]. If one chooses $E_1 > E_2$, the expected velocity based on the single atom case always has a positive sign. However, for $N > 1$, the sign depends on the model properties and is generally unknown. The electrophoretic ratchet is therefore a good tool to study and quantify many-particle effects.

7.2 Static field

7.2.1 Velocity as a function of field

The velocity as a function of the field is shown for $N = 4 \ldots 20$ (MC model) and $N = 4 \ldots 12$ (ME model) in Fig. 7.1, using $\gamma = \alpha$ and $T = 500\,\mathrm{K}$. There are noticeable differences between ME and MC models especially for $E > 0.1$ eV as the velocities begin to decrease for the largest $N > 7$ islands in the ME model. This 'negative conductivity' type effect is caused by the trap configurations as demonstrated in Fig. 7.1(f) for $N = 11$ and in Fig. 7.1(e) for $N = 12$, where velocities and probabilities of the main trap configurations are shown as a function of E with (f) diagonal and (e) axis directed fields and temperatures 400 K, 600 K and 800 K. In the diagonal field there are several energetically equivalent trap configurations for the 11-atom island, hence the probability of the main trap configuration does not reach 1.

Within the linear response regime (with a field up to $E \sim 0.01\,\mathrm{eV}$), the velocity is affected by the diffusion coefficient and the 'magic size' effect[1] strongly affects the velocity for small islands ($N < 11$); in the regime $E > 0.1\,\mathrm{eV}$ the velocity depends strongly on whether N is odd or even and the velocity is significantly larger for odd-N islands. This effect is stronger for the axis-directed field, for which all odd-N islands are faster and curves become 'bunched' in two distinctive groups with a noticeable gap in between. At least for smaller islands, this is caused by the fact that the even-N islands easily fall into complete rectangle shapes of width 2 (*i.e.* two atom rows). Escaping this shape requires breaking two nearest-neighbor bonds. For odd-N islands, such a compact shape is unavailable, and hence they have faster transition paths available (this aspect is studied further in Sec. V). Around $E \sim 0.1$ eV the velocity behavior clearly changes for all but the smallest islands. At $E \sim 0.25$ eV the velocity is no longer increasing for the MC model.

The behavior of the island $N = 10$ is somewhat special for both the ME model and the MC model, since at low temperatures the velocity is decreasing for $E = 0.02 \ldots 0.05\,\mathrm{eV}$. At larger fields, the behavior becomes similar to large even-N islands, indicating that 10 atoms is already enough to capture the characteristic behavior of larger islands.

The simulation data (not shown) indicates that in fields $E \sim 0.1$ eV and beyond, the island becomes strongly deformed and would be much more likely to break up for diagonal fields when compared to axis-directed fields with the same magnitudes. The reason for this is that the islands on average have less atomic bonds in a diagonal

[1] In small fields, the velocity and diffusion are greatly reduced for islands that can form a compact near-square rectangular configuration with a minimum escape barrier of $2E_B$. The smallest islands with this property contain $4 = 2 \times 2,\ 6 = 2 \times 3,\ 8 = 2 \times 4,\ 9 = 3 \times 3,\ 12 = 3 \times 4$ atoms.

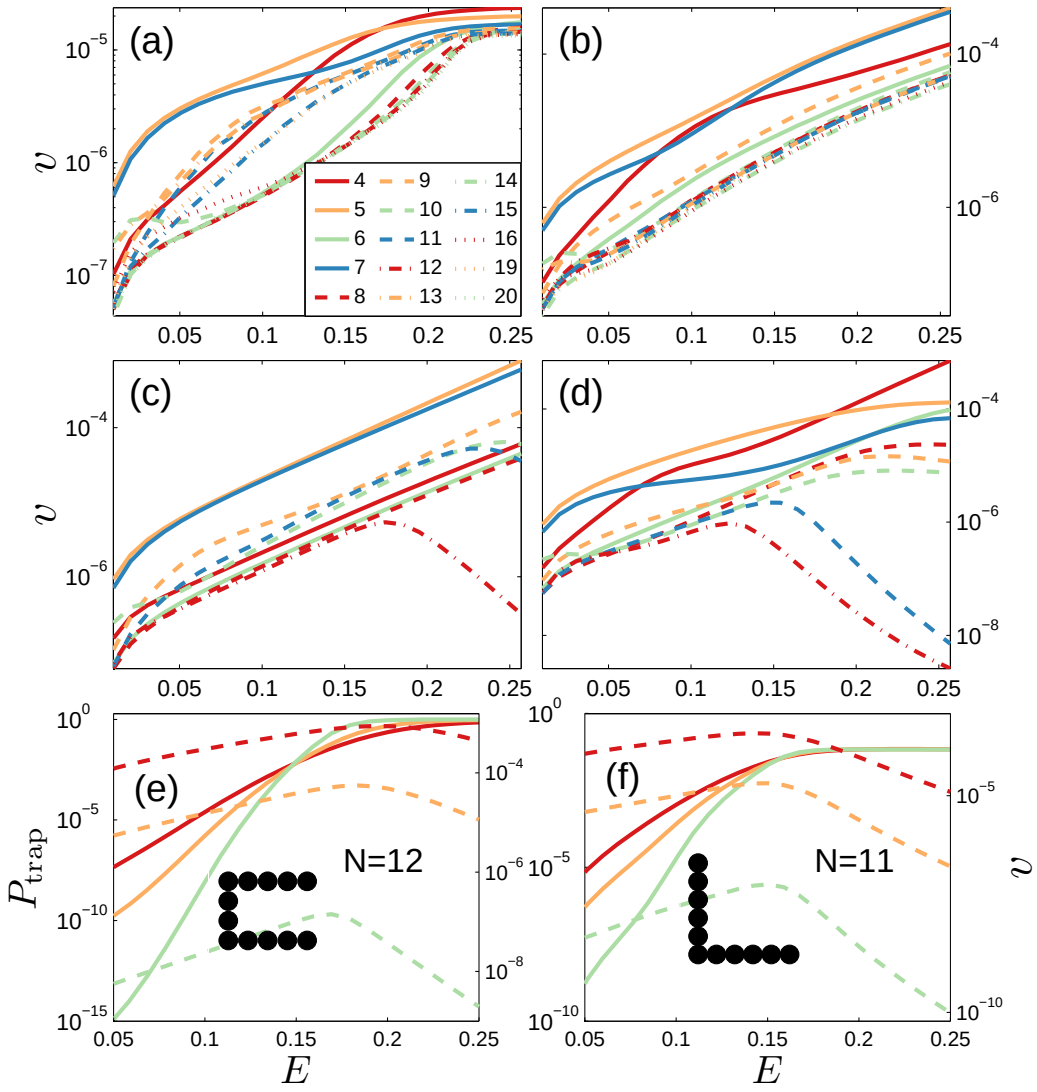

Figure 7.1: (a)-(d) Island velocity in the (a and b) MC model $N = 4 \ldots 20$ and (c and d) ME model $N = 4 \ldots 12$ at $T = 500$ K with (a and c) $\gamma = 0°$ and (b and d) $\gamma = 45°$. (e)-(f) Velocity (dashed lines) and probabilities P_{trap} (solid lines) of the main trap configurations shown in the inset figures in the ME model for (e) $N = 12$ and (f) $N = 11$. The vertical axes on the left shows P_{trap} and the axes on the right shows v. Corresponding temperatures, as indicated here with the dashed v lines, are 800 K (red upmost), 600 K (yellow middle) and 400 K (green lowest).

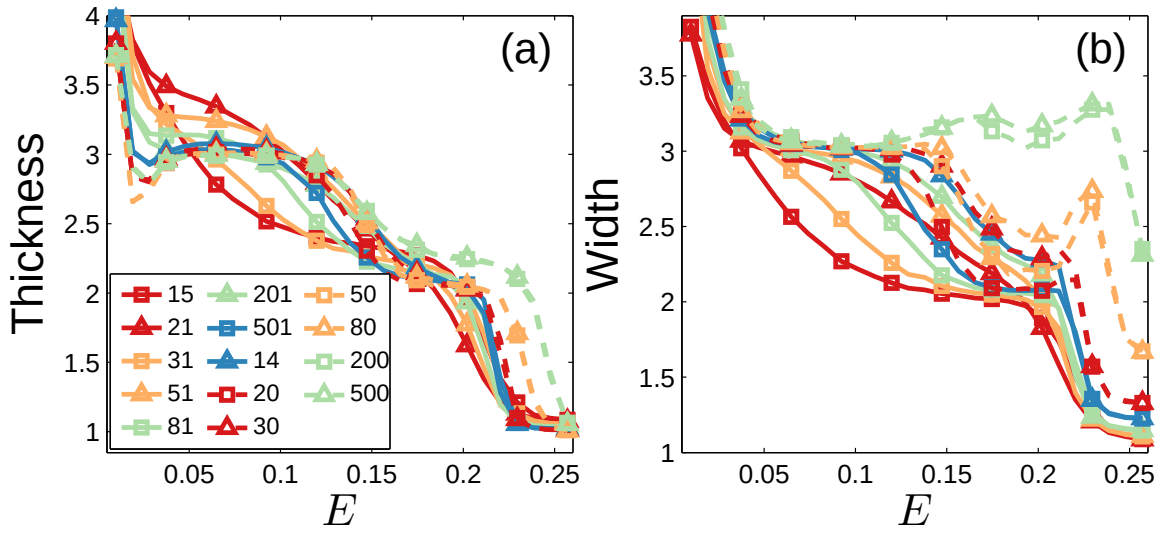

Figure 7.2: Change of average geometry of various island sizes at $T = 500$ K as a function of field amplitude ($\alpha = \gamma = 0°$) measured by the island (a) average thickness and (b) width perpendicular to the field (see text). Note that the density of data points is higher than the density of plotting symbols. The data is for the MC model.

field, which more easily results into break-up of the island.

In Fig. 7.2 we show the transition of the island geometry as a function of the axis-directed field ($\gamma = \alpha = 0°$) for the MC model. The geometry is characterized by the average thickness and width of the island, which can be computed from the maximum elongation of the island in both parallel and perpendicular to the field: Width is given by the perpendicular size and thickness by the number of atoms N divided by the parallel size.[2]

Three distinctive steps in the curves of Fig. 7.2 corresponding to widths 1, 2 and 3 are seen (*i.e.* on average the island consist of 1-3 rows of atoms). Step 3 becomes visible only for large enough systems ($N \sim 50$), whereas the other two steps are visible for all systems. For smaller islands ($N < 100$) there is a clear even-odd effect for the island size at $E \approx 0.05 \ldots 0.20$ eV. The average shape of even-N islands is flatter, which indicates that they are usually found in their tightly-bound rectangle configurations, whereas the sizes of odd-N islands can vary more freely. The increase of the width for large islands in fields $E \sim 0.2$ eV is caused by configurations where, instead of a single rod, there are several smaller rods that together occupy adjacent rows and consecutive small rods have single row misplacement in perpendicular axis direction (see Fig. 1 in the supplemental material of Article III). Only increasing the field further, a single rod structure with smaller total energy becomes a dominating configuration. For average

[2]For example, consider the island configuration in Fig. 4.5 with $N = 10$ and $\gamma = \alpha = 0°$. Thickness for this configuration is 10/4 and width is 4.

thickness, there is also local minimum at $E \approx 0.02$ eV. Similar behavior can be also found by using other measures, such as the variance of the width (see Fig. 2 in the supplemental material).

7.2.2 The effect of the measuring and field angles

Now let us consider the case $\alpha \neq \gamma$. In Fig. 7.3 the effect of the field angle α is shown for $N = 6 \ldots 12$ for the measuring directions $\gamma = 0°$ and $\gamma = 45°$ computed for the ME model using $E = 0.08$ eV and $T = 500$ K. To find out the proportional velocity, we scale the results by corresponding $v(\gamma = \alpha)$. In the following we present results for the interval $\alpha \in [\gamma, \gamma + 90°]$ from which the results for all angles can be extracted.

In contrast to the single particle in the case $\gamma = 0°$, the maximum velocity is not always at $\alpha = 0°$, but can indeed have a value between $0° < \alpha < 90°$ depending on the island size. Increasing E and decreasing T leads to increased velocity, however the field E must be large enough for the non-linear effect to appear. The maximum velocity is found with $\alpha = 15 \ldots 25°$ for islands over 10 atoms. Rotating the field slightly (*i.e.* increasing $|\gamma - \alpha|$) creates a small field component in y direction. This decreases the barrier for the corner rounding process on one side of the island, which leads to increased velocity.

For the measuring direction $\gamma = 45°$, the maximum velocity is found for $45° < \alpha < 90°$ for all but the smallest islands. This is expected from the single particle case. However, there are two local maxima for islands of size $N > 10$ located both sides of the angle $\alpha = 90°$, creating a small deviation of approximately 15° from angle 90°. The global maximum is found around $\alpha \approx 70°$ and the second one around 105°. For the smallest islands $N < 7$, no increase is found. As demonstrated for the case $N = 11$, a two-maximum structure appears when the field gets strong enough. Transport in the diagonal direction is generally more difficult compared to the axis direction because of the absence of stable rectangular configurations. By rotating the field, rectangular shapes become stable and the velocity increase occurs for a much larger range of field angles than for $\gamma = 0°$.

The findings above can be also verified for the MC model with some differences in the odd-even effect and in field amplitude response. The maximum increase of the velocity is plotted in Fig. 7.4 for islands $N = 4 \ldots 24$ with several field amplitudes using the MC model. The odd-even effect is strong for $N < 15$ and only for larger islands, deviations begin to appear. The results for the MC model show that in the case $\gamma = 0°$ velocity increase, caused by the rotated field, is larger for even-N islands than odd-N islands, and in the case $\gamma = 45°$ it is other way around. The optimal angles for odd-N islands are smaller than for the even-N islands in the case $\gamma = 0°$, whereas for the case $\gamma = 45°$ the behavior is just the opposite.

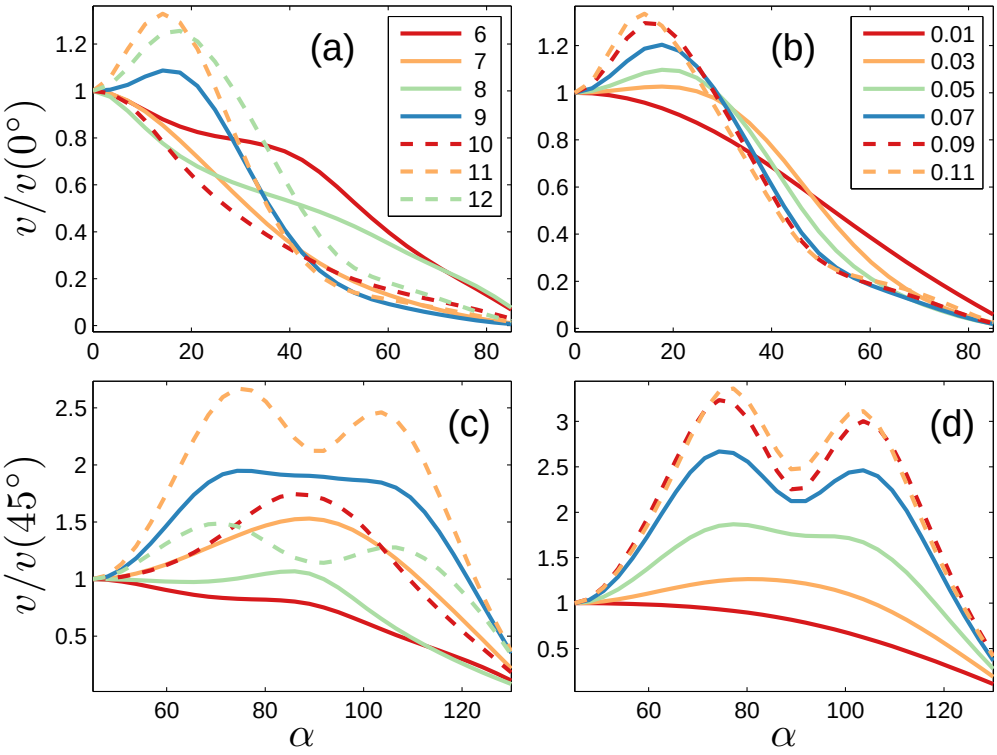

Figure 7.3: Velocity increase in directions (a and b) $\gamma = 0°$ and (c and d) $\gamma = 45°$ as a function of field angles at temperature $T = 500$ K. (a) Velocity scaled with $v(\alpha = 0°)$ for $N = 6 \ldots 12$ and $E = 0.08$ eV. (b) Case $N = 12$ with several field amplitudes $E = 0.01 \ldots 0.11$ eV. (c) Velocity scaled with $v(\alpha = 45°)$ for $N = 6 \ldots 12$ and $E = 0.07$ eV. (d) Case $N = 11$ with several field amplitudes $E = 0.01 \ldots 0.11$ eV. The data is for the ME model.

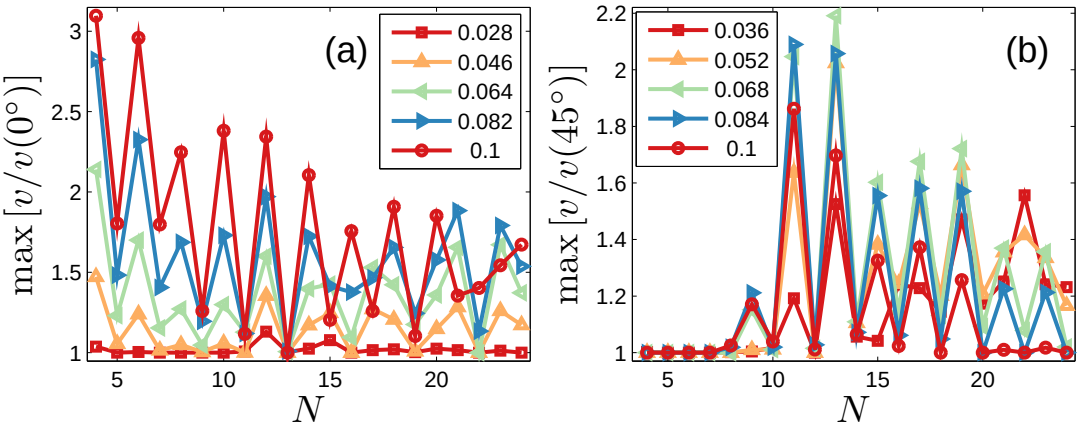

Figure 7.4: Maximum velocity increase for $N = 4 \ldots 24$ compared to (a) $v(0°)$ and (b) $v(45°)$ for several field amplitudes $E = 0.028 \ldots 0.1$ eV in $T = 500$ K. The data is for the MC model.

The results above show that the velocity depends strongly on the measurement and field directions and the velocity can be significantly increased by setting a small $15° \ldots 25°$ difference between the field and measurement directions. This can be exploited by using a time-dependent field. For the case $\gamma = 45°$ a velocity increase can be expected based on the single atom case, however the optimal field angle for islands is not $\alpha \approx 90°$, but has a double maxima structure with optimal angles around 70° and 105°. This deviation from the single atom case results from the corner process. By introducing a small non-axis-directed field component, going around the corner is made easier. For the same reason, the velocity increase is present also in the case $\gamma = 0°$, where the maximum velocity is found for field angles $\alpha \approx 20°$. It is also found that there is a strong odd-even island-size effect affecting the amount of velocity increase and also the values of optimal α. For the case $\gamma = 0°$, even-N islands become significantly faster and for the case $\gamma = 45°$ the behavior is just the opposite. Here the results differ between the ME and MC models, especially for the case $\gamma = 0°$, as the ME model does not reproduce the odd-even effect or the increase for the smallest islands. This indicates that the configurations with only diagonal bonds between parts of the island, present only in the MC model, become important in this particular situation.

7.2.3 Energy barriers and the leading relaxation constant

Energy barriers

An effective energy barrier for the island dynamics can be found via Arrhenius plots $\ln(D_{\text{eff}})$ or $\ln(v)$ vs. $\beta = 1/k_{\text{B}}T$. If the effective barrier is constant for a large temperature interval, it means that the transport process is similar in that region and a data collapse is possible. In previous studies concerning equilibrium and very small fields, it has been found that the effective barrier is around 0.75 eV for large islands $N > 10$ [80, 122, 115, 124] and varies between $0.5 \ldots 0.8$ eV for the smallest islands [168]. With nearest-neighbor count energetics, this is roughly equivalent to transitions that break two nearest-neighbor bonds. The effective barrier is typically lower for small islands and in higher temperatures [124, 183]. We used the ME model to compute accurately the temperature dependent effective barriers for small islands for several field amplitudes. Because of a large statistical error, a similar study would be complicated by using only simulation data. Because of the computational difficulties in low temperatures (especially for D_{eff}), we show only those values that remain reliable and omit the results for the lowest temperatures where data becomes noisy.

In Fig. 7.5, the running slope of the Arrhenius curve or the effective activation barrier is shown for several field amplitudes for $N = 11$ (a and c) and 12 (b and d) using both D_{eff} (a and b) and v (c and d) in direction $\gamma = \alpha = 0°$. In zero field, an effective barrier around 0.7 eV is found with only a minor temperature dependence. However,

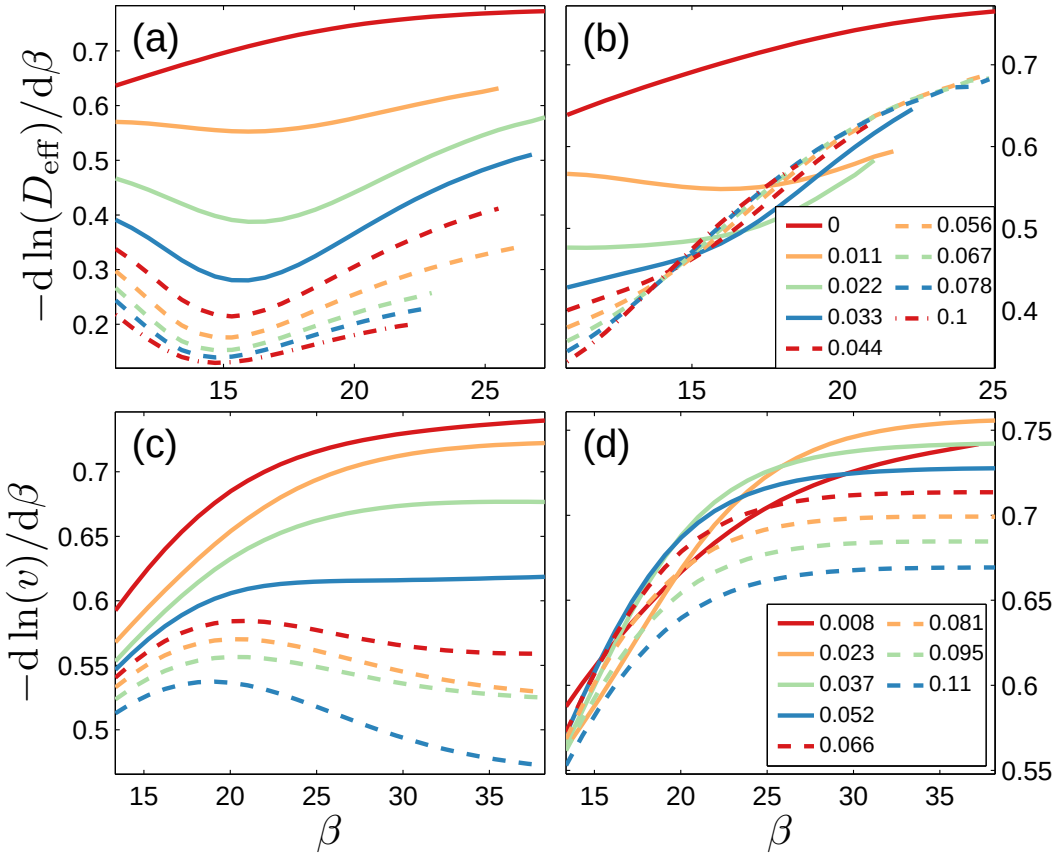

Figure 7.5: Running slope of the Arrhenius curves computed using (a and b) D_{eff} and (c and d) v for (a and c) $N = 11$ and (b and d) $N = 12$ with axis directed field (*i.e.* $\gamma = \alpha = 0°$) and amplitudes $E = 0 \ldots .1$ eV.

as the field gets stronger, the effective barrier depends strongly on the temperature. At temperatures around $700 \ldots 800$ K a distinctive local minimum is found for $N = 11$ using D_{eff}, which indicates some type of change in the diffusive property of the island transport. For v, there is a local maximum instead of a minimum. A strong even-odd effect is visible. At low temperatures, the field has only a minor effect on the effective barrier for even islands, whereas the effect is large for odd islands. The spread for the effective barriers is much smaller for the scaling of v when compared to that computed using D_{eff}, otherwise the behavior is similar. The behavior for $\gamma = 45°$ is found to be very similar and is not shown here. Since islands $N = 11$ and $N = 12$ already have characteristics of large islands (see [183] and Sec. VI), we expect similar behavior to be observed also for somewhat larger islands.

There is no well-defined effective energy barrier in the presence of an electric field. In addition to the field amplitude, the effective barrier depends strongly on the temperature, especially for temperatures above 500 K. In the general case, velocities and effective diffusion coefficients of small islands do not follow any simple scaling laws

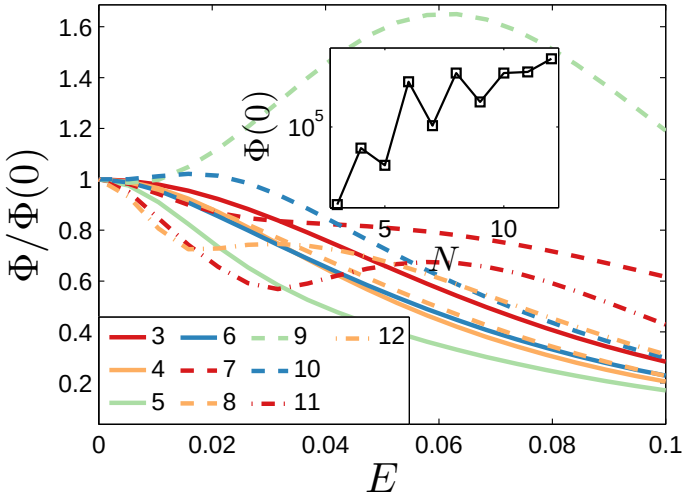

Figure 7.6: Leading relaxation constant Φ as a function of field amplitude for $N = 3 \ldots 12$ re-scaled with zero field values (shown in inset) with $T = 600$ K and $\gamma = \alpha = 0°$.

such as in the case of the linear response [122]. Also the effective barriers for diffusion and the velocity differ.

The leading relaxation constant

Next we study the leading relaxation constant of the ME model. The expected result is that the relaxation constant decreases monotonously as the field gets stronger. However, because of the trap configurations of the ME model, the relaxation constants must eventually increase rapidly as the field becomes very large. We are aware of only one previous study where the relaxation constant and few other eigenvalues were computed directly, for vacancy islands using a discretized continuous-space model [77].

In Fig. 7.6, we show the leading relaxation constant Φ in zero field (inset figure) and as a function of the axis directed field for $N = 3 \ldots 12$ in $T = 600$ K. Within the linear response regime, the relaxation times are indeed decreasing for all N. However, for $N = 9 \ldots 12$ there exist local maxima with $E = 0.02 \ldots 0.06$ eV. This effect is not caused by intersections with other eigenvalues, in that it is a genuine property of the second eigenvalue (as identified at $E = 0$). For $N = 9$, the phenomenon is strongest. The locations and heights of the maxima are slightly shifted by changing the temperature. For fields beyond $E > 0.1$ eV, we can confirm that that relaxation times for $N > 7$ increase rapidly. However, the computations become cumbersome and the data is noisy because of the instability of solving eigenvalues iteratively for highly non-symmetric matrices.

The maximum of Φ seems to appear shortly after the field amplitude reaches the

non-linear regime. The location of the maximum is around 0.06 eV for island sizes 9 and 11 and around 0.03 eV for island sizes 10 and 12. Also, this effect seems to become weaker as the island size increases from $N = 9$ to $N = 12$. The increased relaxation time does not have an evident correlation with the transport properties in this Section. Although for $N = 10$ and $N = 12$ a slight correlation can be seen with Figs. 7.5(b) and (d), where the effective barrier turns from decreasing into increasing around 0.03 eV, however this cannot be directly related to any microscopic processes.

7.3 Time-dependent field

7.3.1 Pulsed field

From the static-field results, we expect that the velocity can be increased by rotating the field. In its most simple form, this can be utilized by introducing a pulsating field with a varying angle and setting a temporal period τ larger than the relaxation time of the island (the adiabatic limit). In most cases, this would lead to increased long time velocity. For example, using two (strong) fields with angles $\pm 20^\circ$ and large equal temporal periods, would increase the long-time transport velocity of almost all islands, and especially those with even N, in direction 0°. In the following we study the behavior of islands for small values of τ. As before, we re-scale the velocities with the corresponding velocity without rotation (*i.e.* $v(\alpha = \gamma)$).

In Fig. 7.7, we show velocities for $N = 4 \ldots 12$ with $T = 500$ K and $\alpha = \pm 10^\circ$ compared to the static field velocity in the direction $\alpha = \gamma = 0^\circ$. For all but $N = 10$, the velocity can be slightly increased for small τ. Odd-N islands have a distinctive local maximum around $\tau = 10^1 \ldots 10^2$, but the largest increase occurs typically at the adiabatic limit. For larger islands $N > 10$, minimum velocity is found with $\tau \sim 10^3 \ldots 10^4$.

In Fig. 7.8, we show similar results for $\gamma = 45^\circ$. Because of the double-maximum structure, we show results for both $\alpha = 45 \pm 20^\circ$ and $45 \pm 50^\circ$ keeping other parameters the same as before. Again, the large τ limit yields the largest velocity for almost all islands. For $N \in \{8, 10, 12\}$ small local maximum occurs around $\tau = 10^4 \ldots 10^5$ for suitable parameters. This is demonstrated in detail in Fig. 7.8(c) for $N = 8$ for several field amplitudes. For $N = 9$ and $N = 11$ the minimum is created around $\tau = 10^3 \ldots 10^4$. It can be also found for $N = 12$ by fine-tuning the parameters (data not shown).

Similar results are also found for larger islands using the MC model. Although there is some structure (such as local maxima) for small τ values for large N, there is no

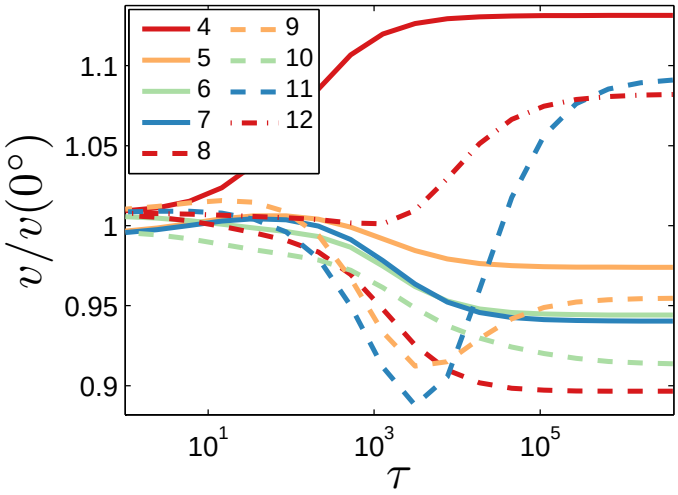

Figure 7.7: Velocity increase in the pulsed field for $N = 4 \ldots 12$, $T = 500$ K, $E = 0.06$ eV with $\gamma = 0°$ and $\alpha = \pm 10°$. The data is for the ME model.

longer any noticeable increase for the velocity for small τ's. Increase is found only at the adiabatic limit. In Fig. 7.9 we show the velocity for $N = 20$ with several values of α for $\gamma = 0°$ and $\gamma = 45°$.

The results indicate that the steady state velocity of the islands in a pulsed field depends strongly on the period τ for small islands, but the dependency becomes weaker for large islands $N > 10$. For large islands, a significant increase in velocity is found only at the adiabatic limit (large τ) for both $\gamma = 0°$ and $\gamma = 45°$. A small τ tends to increase the velocity of small islands. There is a velocity minimum at $\tau \sim 10^4$ for all large and also many small islands, indicating the sensitivity to this specific period. Alternatively, the same period produces a maximum velocity for some small even-N islands. Lowering the temperature significantly increases the sensitivity of the velocity to the τ.

7.3.2 Electrophoretic ratchet

In Fig. 7.10 we show the velocity of islands $N = 4 \ldots 12$ in an electrophoretic ratchet as a function of τ for the ME model using $T = 500$ K, $x = 1/4$ and $E_1 = 0.03$ eV (*i.e.* $E_2 = 0.03x/(1-x) = 0.01$ eV). For $N \in \{4, 10, 12\}$, there is a current inversion. For all other N, the velocity remains positive.

For $N = 4$ and $N = 10$, the current inversion is expected, since velocities computed at the simple limits of $\tau \to \{0, \infty\}$ have a different sign. We call this an adiabatic type current inversion. As explained in Section 3.1.3, at $\tau \to 0$ the velocity follows from the mean-field stochastic generator. For $E_1 > E_2$, the mean-field velocity is

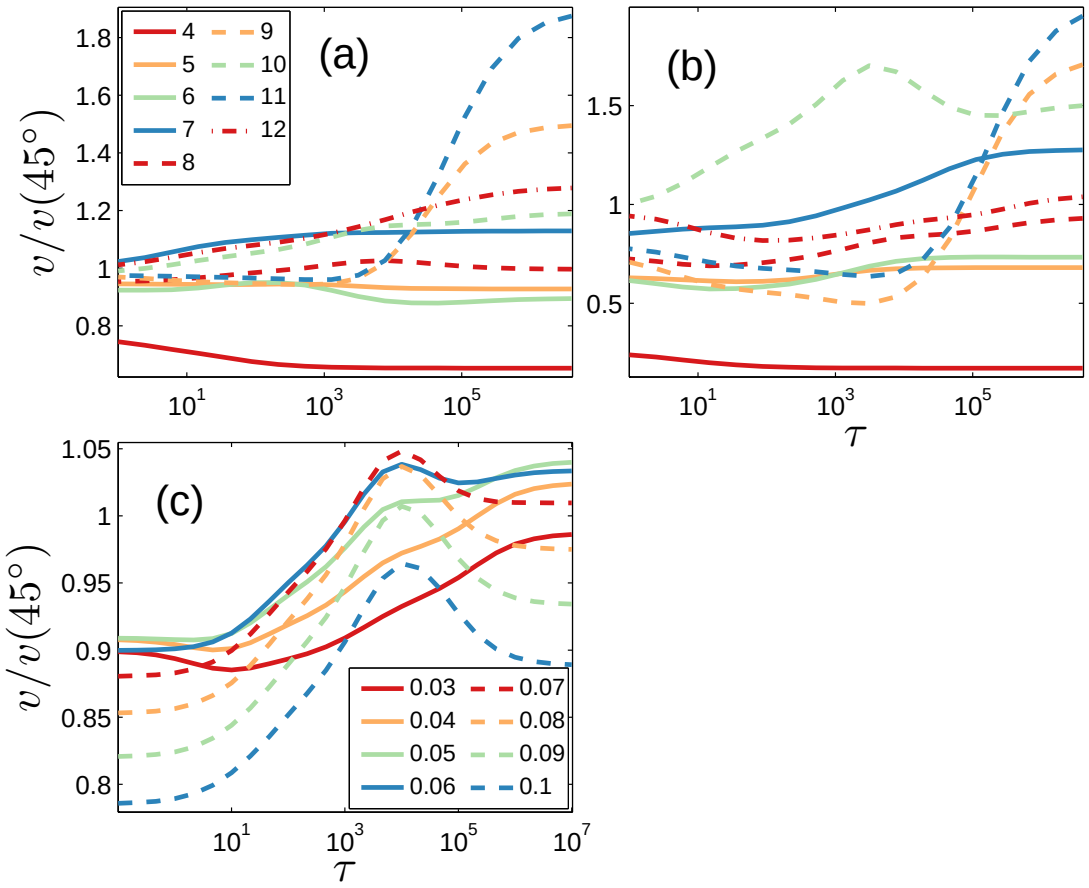

Figure 7.8: Velocity increase in a pulsed field for several small islands with $\gamma = 45°$ and $T = 500$ K. (a)-(b) $N = 4 \ldots 12$, $T = 500$ K, $E = 0.06$ eV with (a) $\alpha = 45 \pm 20°$ and (b) $\alpha = 45 \pm 50°$. (c) Distinctive behavior of $N = 8$ with $E = 0.03 \ldots 0.1$ eV and $\alpha = 45 \pm 30°$.

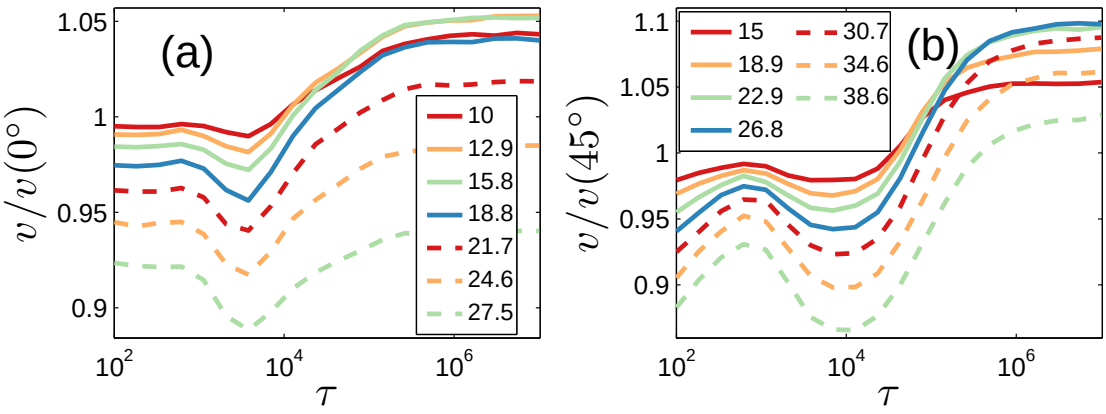

Figure 7.9: Velocity increase in a pulsed field with several pairs of the field angle α (values $|\alpha - \gamma|$ are shown in the figure) for $N = 20$ and $T = 600$ K with field amplitude $E = 0.05$ eV for (a) $\gamma = 0°$ and (b) $\gamma = 45°$. The data is for the MC model.

expected to be positive in the non-linear regime, because of the exponential rates.[3] At the adiabatic limit $\tau \to \infty$, the velocity approaches $v_{\mathrm{ad}} = xv(E_1) - (1-x)v(E_2)$. The sign of v_{ad} therefore results from the shape of the velocity curve $v(E)$, which can be non-monotonous and depends strongly on the island size (see Fig. 7.1). Therefore both signs for v_{ad} are possible in theory. For the island model, the negative sign for v_{ad} is typical for $N = 4$ and $N = 10$, but very rare for others. For $N = 12$, the simple limits typically yield the same sign and instead the inversion results from a time-dependent field in a non-trivial fashion.

The velocity for $N = 12$ is shown in more detail in Fig. 7.11 with temperature $T = 500$ K and $T = 700$ K and several field amplitudes. The temperature and the field amplitude have a very large effect on the velocity in an electrophoretic ratchet. The current inversion easily disappears for increasing the temperature or the field amplitude.

The results for the MC model are similar. There are indeed deep minima for $\tau = 10^4 \ldots 10^6$ for large islands which creates a current inversion. This is shown in Fig. 7.12 for several islands. For large islands, two local maxima appear at $\tau = 10^3 \ldots 10^4$. Since the current inversion occurs typically only at finite values of τ, it is indeed caused by the interaction between time-dependent field and atoms. For small islands $N < 15$, there is a strong odd-even island size dependency which eventually disappears for larger islands. For an electrophoretic ratchet this odd-even effect becomes important already at much smaller fields than in the case of a static field. This is because the

[3]For example, consider a single free particle affected by the field $E_1 > 0$ on the right and $E_2 = E_1 x/(1-x)$ on the left with temporal periods $\tau_1 = x\tau$ and $\tau_2 = (1-x)\tau$. For the corresponding mean field rates Γ_{right} and Γ_{left}, one has $\frac{\Gamma_{\mathrm{right}}}{\Gamma_{\mathrm{left}}} = \frac{xe^{E_1}+(1-x)e^{-E_2}}{xe^{-E_1}+(1-x)e^{E_2}} > 1$ for $0 < x < 1/2$, *i.e.* the mean field drift $\Gamma_R - \Gamma_L > 0$ is always on the right.

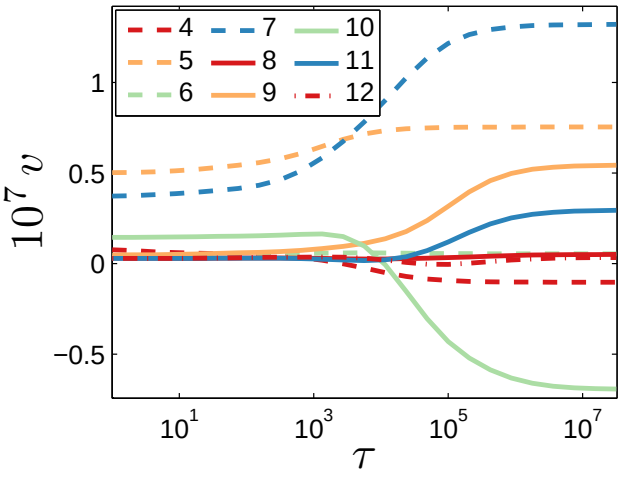

Figure 7.10: Velocity in an electrophoretic ratchet with $N = 4 \ldots 12$ and $x = 1/4$ as a function of τ with $T = 500$ K and $E_1 = 0.03$ eV. The data is for the ME model.

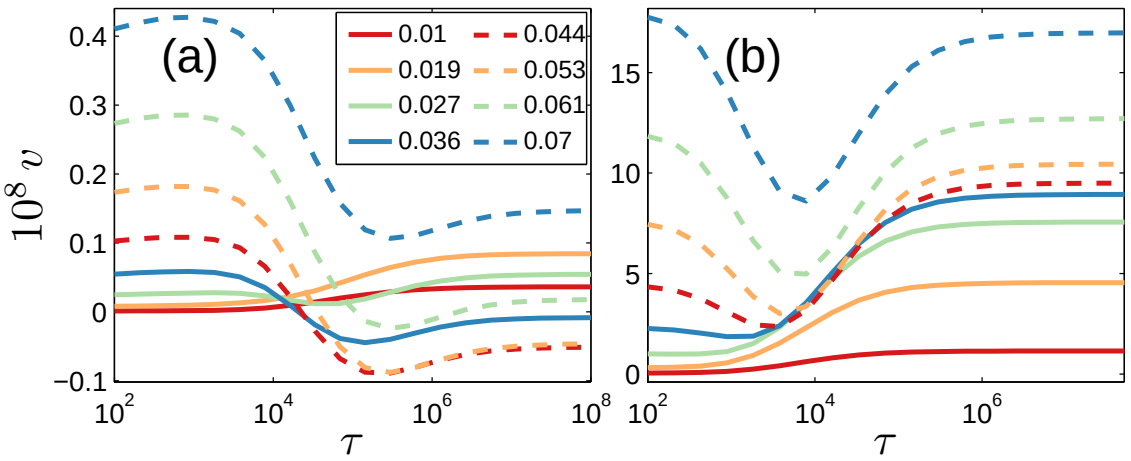

Figure 7.11: Velocity in an electrophoretic ratchet with $N = 12$ and $x = 1/4$ as a function of τ for several field amplitudes $E = 0.01 \ldots 0.07$ eV with (a) $T = 500$ K and (b) $T = 700$ K. The data is for the ME model.

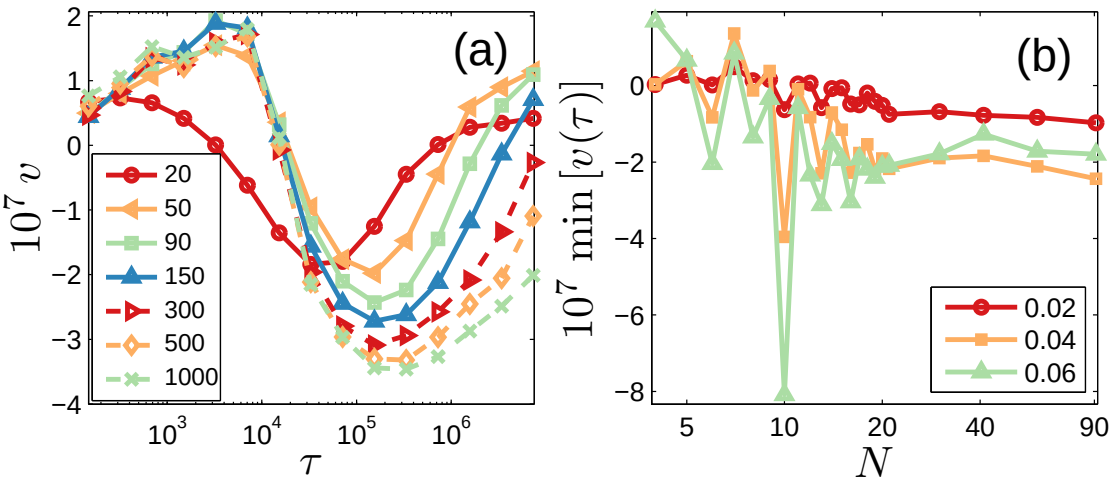

Figure 7.12: Velocity in the electrophoretic ratchet with $T = 600$ K and $x = 1/4$ for the MC model. (a) Velocity for the large islands as a function of τ for $E_1 = 0.04$ eV. (b) Minimum velocities for several islands $N = 4 \ldots 91$ for $E_1 = 0.02 \ldots 0.06$ eV.

ratcheting mechanism with an alternating field direction tends to force islands into thin rectangular shapes.

We conclude that the τ-dependency in an electrophoretic ratchet is found to be much stronger than in the case of a pulsed field. With suitable field periods τ around $10^4 \ldots 10^6$, a velocity inversion occurs for all large islands ($N > 10$) and also for smaller even-N islands. Especially for smaller islands with $N < 20$, the inversion depends strongly on the temperature and field strength, disappearing at large temperatures. Compared to velocity increase in a pulsed field, inversion phenomena are observed already with very small field amplitudes near the linear response regime ($E \sim 0.01$ eV). An electrophoretic ratchet have been previously studied within the context of reptating polymers where a similar type of current inversion was found as a function of polymer size [134].

7.4 Transition sequences

In this Section, we present typical transport mechanisms computed using the cycle optimization method of Section 5.2.1 for small islands using the ME model. We found that the dominating transport cycles for time-dependent fields are usually the same as those for the static field, especially for the electrophoretic ratchet where two directions of motion are competing. Also the results for the $\gamma = 0°$ and $\gamma = 45°$ are qualitatively similar (the 'zig-zag' configurations appear only for islands much larger than $N = 12$).

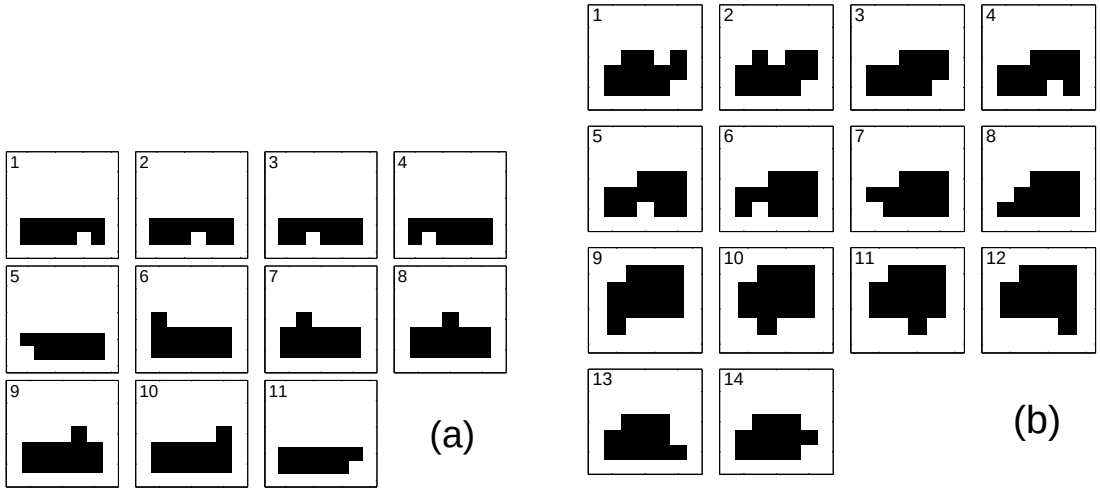

Figure 7.13: The dominating transport cycle for (a) $N = 11$ and (b) $N = 12$ in large fields in axis direction.

For time-dependent fields, dominating cycles differ from the static field case only for small values of τ, for which the islands have no time to go through a full static-field-type cycles before the potential is changed. Therefore the dominating transport cycles cannot be used to explain the velocity increase by a pulsed field in large τ limit or velocity inversion for the electrophoretic ratchet with $\tau = 10^4 \ldots 10^6$. In the following, we set $T = 600$ K and try various field amplitudes E and report a few optimal cycles of the type (5.6), with function f being the displacement matrix D. It was found that the results are usually the same for both (5.5) and (5.6).

In a static field, typically two kinds of dominating cycles are found corresponding to the small and large fields. For small fields, $E < 0.1$ eV, the island remains nearly square and for large fields, $E > 0.1$ eV, the island becomes flatter. In Fig. 7.13 we show dominating transport cycles for (a) $N = 11$ and (b) $N = 12$ in a large axis-directed field. The cycle shown for $N = 11$ is found for all small odd-N islands in large fields and proceeds by breaking only single nearest-neighbor bonds. This is a similar mechanism as previously proposed being the easiest diffusion pathway for $N = 5$ [183]. For $N = 12$ and other small even-N islands, the previous type cycle would lead to configuration that requires breaking of two nearest-neighbor bonds, whereas the optimized cycle shown in Fig. 7.13(b) can work with only single bond-breaking transitions. Unlike one might expect based on the Fig. 7.2, optimal cycles involving islands with an expected width 1 are not found even for very large fields $E \approx 0.25$ eV. This is probably because of the trap configurations that appear for the ME model.

In Fig. 7.14, we show the dominating cycles in the pulsed field case for $N = 9$ and $N = 10$ with small τ. In Fig. 7.14(a) the cycle is shown for $N = 9$ using $\gamma = 0°$ and

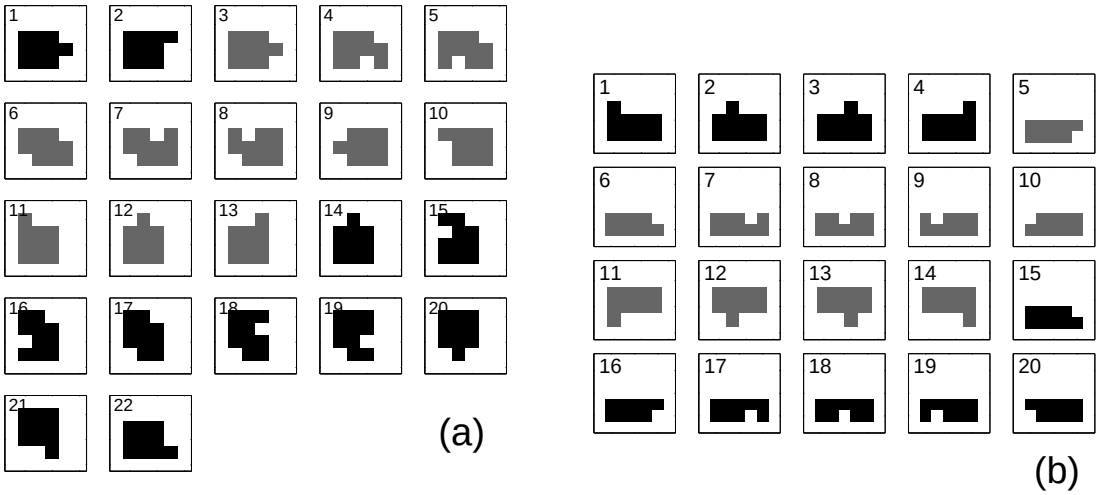

Figure 7.14: A dominating cycles in pulsed field with small τ. (a) $N = 10$ with $\gamma = 45°$ and $\alpha = 45 \pm 25°$, gray color indicates $\alpha = 20°$ state. (b) $N = 9$ with $\gamma = 0°$ and $\alpha = \pm 20°$, gray color indicates $\alpha = -20°$ state.

$\alpha = \pm 20°$, and in figure Fig. 7.14(b) for $N = 10$, $\gamma = 45°$ and $\alpha = 45 \pm 20°$. With these parameters, the velocity is increased when compared to the static field case (see Section 7.3.1). The configurations for $\alpha = -20°$ and $\alpha = 20°$ are shown in gray and the change of potential occurs between the gray and black frames. The cycles are basically the same as for the static field case except that the barriers for the transitions are lowered due to the pulsed field. This stochastic-resonance-type mechanism, where the time-scales of two processes are matched, explains the results seen in Section 7.3.1 for the increase of the velocity for small τ.

7.5 Discussion

We have studied the dynamics of single-layer metal-on-metal islands under strong static and time-dependent forces with a continuous-time Monte Carlo and numerical master equation methods. The aim was to study complex non-linear transport phenomena arising when islands are driven out of equilibrium, far beyond the linear response regime. Several non-linear effects were identified, most importantly the increase of the velocity by a rotated field and velocity inversions in the electrophoretic ratchet. Although the behavior was found to be highly complex, depending strongly on many parameters such as temperature, field (angle, amplitude and period) and island size, generic behavior could be identified.

First, we studied static-field transport up to field strengths corresponding single bond-

breaking energy barrier (*i.e.* term E_B in Eq. (3.3), 0.260 eV for Cu(001)). For large fields, many differences arise when compared to equilibrium or linear-response conditions because typical island configurations are no longer nearly square, but are heavily deformed by the field. A strong even-odd dependence on the island size was found, which has an influence to even large islands (up to $\sim$100 atoms). The range of field amplitudes $E = 0.01 \ldots 0.1$ eV for Cu was found to be especially interesting from the point of view of velocity increase and inversion, since for larger fields these phenomena tend to disappear. In this regime, the model is also expected to remain somewhat realistic, based on the observations of the island geometry changes (no rod configurations) and simulations (small island break-up rate). This is also the regime, where the results for the MC and ME models coincide. The direction of the field with respect to the axis was found to have a large effect on the drift. Introducing a small deviation between the measurement and field angles usually leads to an increased velocity. Although this is expected in the case of the diagonal measurement direction, it was also found in the direction of axis, which purely results from many-particle interactions coupling the internal degrees of freedom with the center-of-mass motion. A two-maxima structure for the velocity was found as a function of the field angle. By computing the second-highest eigenvalue of the stochastic generator (the highest one being zero), it was found that the leading relaxation time displays a non-monotonous behavior as a function of the field strength for small islands. The physical meaning of this is unclear and further studies are needed.

When a periodic time-dependent variation was added to the field, a complex dependence between the velocity and the field period was found. First we studied the pulsed-field case using symmetrically rotated fields around the measuring direction along the axis and the diagonal. It was found that the velocity was increased at very large periods (*i.e.* slowly varying field), and maxima/minima were found for smaller periods. The second type of field was an electrophoretic ratchet that creates a time-dependent force with a zero mean force. It was found to produce current inversions for all large islands. There are two types of inversion: a genuine time-dependent inversion and an adiabatic inversion for a slowly varying field. Since current inversions are not possible for a single atom, it is a pure many-particle effect. In theory, this type of electrophoretic ratcheting would allow separation of islands based on their size. In contrast with the velocity increase phenomenon for the pulsed field, current inversion occurs already in very small fields near linear response regime. One must, however, note that velocities in the electrophoretic ratchet are very small compared to velocities in non-zero mean force fields.

For both types of time-dependent fields, it was found that for certain large field switching periods (namely for $\tau = 10^4 \ldots 10^6$ for temperatures $T = 400 \ldots 700\,\mathrm{K}$), the velocity has a minimum for large islands. This time scale corresponds to an atom breaking two nearest neighbor bonds, which is the effective energy barrier process found in this and all previous studies for this model.

Our results indicate that the typical large island behavior begins already for islands with just above 10 atoms and the small-size effects become much weaker for larger islands. A similar result was also found in previous studies in equilibrium [183]. For this reason, the behavior of the 10 atom island was found to be somewhat special. Most phenomena found in this work can already be produced with islands up to 12 atoms. In general, lowering the temperature tends to make velocity increase, current inversion and τ sensitivity much stronger at the expense of significantly reducing the absolute velocities. The current inversion in the electrophoretic ratchet may disappear completely in large temperatures. This indicates that a large separation in time scales is a required element for these phenomena (at high temperature limit, all rates become equal). Increasing the field amplitude amplifies the velocity increase and inversion up to some point. Very strong fields, however, can have a decreasing effect. Because of this complex dependence on temperature and the field, a data collapse by dimensionless E/T is not possible far from equilibrium, which is in contrast to the linear response regime [122].

The ME and MC models were found to be generally in good agreement. Using suitable parameters, both models were able to reproduce most of the key findings of this Chapter - especially in small fields. The largest differences were found for the smallest islands $N < 8$, for which the aggressive state reduction (*i.e.* the island must be connected via nearest-neighbor bonds) of the ME model appears to have the largest effect. The vacancy diffusion process was not found to have any significant effect for the ME model. Also, the type of the variation of the field, stochastic or deterministic, was found to have only a minor effect. This is because the time-scale separation of different processes are large, hence the time-scales remain well separated also for random field periods.

By applying the ME model, we were able to investigate large portions of the parameter-space with high accuracy, compute effective exponents of the Arrhenius curves, relaxation times and also identify typical reaction pathways of the islands during transport. The numerically exact ME method shows its power in making the non-linear effects and their systematics discernible. However, the MC model arguably remains physically more realistic than the ME for the treatment of atoms diffusing around a corner and for the deterministic field switching scheme.

Since the barrier structure of our semi-empirical model for the processes on fcc(100) surface is quite generic [123], one can expect similar non-linear phenomena to be present also in other metal-on-metal systems. As long as distinctive barriers exist, the non-linear transport properties reported here are not limited to any precise values of barriers. Although our model is simple, it displays a rich variety of phenomena. This emphasizes the complexity of nonequilibrium many-particle systems and that there is still much to be done in exploring transport in the presence of time-dependent fields.

As discussed in Section 3.4.1, the electromigration force currently achievable in experiments is too small to cause strong non-linear effects discussed here. Our simple model does not allow a direct comparison with experimental data, but our conclusions are generic in nature. By introducing more accurate energetics and adding new microscopic transition types, it is possible that some phenomena disappear while new ones appear, which we demonstrated by comparing the MC and ME models. It would be also interesting to study similar properties on other lattice geometries such as close-packed surfaces, with the effect of steps, strain, detachment/attachment processes and other types of driving or interfering forces included. Experimental results for an electrophoretic ratchet mechanism in the absence of periodic potentials would be of interest also for other types of two and three-dimensional many-particle systems. One may assume that current inversions are indeed common. So far these experiments have been limited to study DNA separation techniques [72, 171, 172].

8 Summary

In this work, we have studied nonequilibrium properties of many-particle systems by numerically solving master equations using linear algebra ('direct') and by Monte Carlo ('indirect') methods. The focus of this work has been in solving the transport properties with a direct method. We have thoroughly discussed relevant practical aspects of the theory and the numerics of master equations and their applicability in the studies of complex many-particle models. We have tested a suitable set of linear algebraic and optimization methods related to the direct method. Both direct and indirect methods were applied to study transport of polymers and metal-on-metal islands in non-homogeneous time-dependent potentials. Although the equilibrium properties of these models are well known, predicting transport properties far from equilibrium is very difficult, because the velocity and diffusion coefficient no longer have a linear relationship. Currently, the only way to gain access to such nonequilibrium properties is by simulation or by solving corresponding master equations numerically.

Although the repton and island migration models are different, they share many common properties. Because of the similar structure with roughly same number of edges per nodes in the transition graphs, both models exhibit similar numerical behavior in linear algebraic and integration computations. Both models also exhibit explicit non-monotonous response to the potential strength. For models with more than one spatial dimension, the directions of the potential and measuring are of a special interest because of inherent spatial anisotropy. As seen for the island model, a properly chosen direction can increase the velocity. For time-dependent potentials, velocity minima and maxima typically appear as a function of the temporal period of the potential. This is caused by correlations between the time-scales of the center-of-mass displacement and internal configurations of the many-particle system. The most striking feature is the current reversal phenomenon that was found in both repton and island models. Although this phenomenon is quite typical when the direction of the forces caused by the potential are changing (*e.g.* flashing ratchet potential and electrophoretic field), its occurrence and details depend strongly on the details of the model. Detailed discussion of results can be found in the discussion sections of Chapters 6 and 7.

Hopefully the results and methods presented in this work also support the efforts to better understand cooperative transport occurring in biological systems and to develop complex artificial molecular motors. Especially having externally adjustable parameters to control molecular motors, such as time-dependent potentials studied in this work, are an important aspect in designing artificial molecular motors [93, 19].

Due to the advances in computer technology and numerical methods, direct solution of the master equation has become a practical method only within the last decade or so. As demonstrated in this work, an ordinary desktop computer can handle systems large enough for large-system characteristics to appear. The master equation method has several advantages. The most important is its numerical accuracy, which can be typically pushed all the way to the extent of floating point arithmetics for non-stiff master equations. Even for stiff systems, the accuracy is usually much better than in Monte Carlo simulations. The second advantage is that the computation is fast, which allows more extensive exploration of the parameter space. Unlike the Monte Carlo method, the master equation method is typically robust against the choice of the initial state, and the arrival to the steady state is straightforward to verify. Also less manual work is required to compute, verify and analyze the results as compared to what is typically needed in the Monte Carlo method. Good accuracy, rapid computations and full knowledge of the available configuration space allow using efficient optimization methods to find optimal parameters and transition cycles.

The most severe limitation of the master equation method is the size limitation. In this work, the practical upper limit for stochastic many-particle systems with sparse transition graphs (*e.g.* repton, island and TASEP models) was found to be around 10^6 states. This limit is often easily met, since the number of states typically grows exponentially with the number of particles. The upper limit is set by the scaling of the computing time and memory consumption as a function of the number of equations. Iterative algorithms that are applied to solve eigenstates, linear problems, and optimize cycles and parameters, are beyond linear. Therefore simply increasing the computing power and time cannot overcome the size limitations. To study larger systems, reduction methods (*e.g.* DMRG) must be applied, which however makes the method less robust and numerically unpredictable because of additional approximations. Compared to Monte Carlo method, the master equation method is not well suited for studying non-Markovian systems. Also setting up the master equation sets and related operators takes some effort, whereas in Monte Carlo simulation, knowing the full configuration space is not required.

There are several ways to extend this work. Detailed discussion for extending the studies of repton and island models can be found in the discussion sections of Chapters 6 and 7. The presented framework including computational methods and model analysis are, however, readily applicable to other models as well. For the master equation method, large separation of timescales makes the equation set stiff, which causes severe numerical instabilities and inaccuracies. Current techniques to overcome this problem are typically based on the assumption of quasi-steady states [44, 135, 146]. However, these techniques cannot be directly applied to study transport in many-particle systems, because stochastic generators are often too complicated and one must also keep track of displacements. Instead, a desired way would be to apply idea of Ref. [163], where both stochastic generator and related operators (*e.g.* a displacement matrix)

were reduced to smaller ones. Turning this procedure into a general and numerically efficient algorithm is, however, technically challenging. The cycle optimization results in this work suggests that dominating cycles remain relatively short even for large systems. Since the total number of short cycles is quite small, optimization with general weight functions might be possible, at least approximatively. Finally, in order to make a numerical master equation method a standard numerical tool to study transport in complex nonequilibrium systems, a comprehensive testing of available numerical linear algebraic, optimization and reduction methods and different types of many-particle models would be in order.

A Time-dependent DMRG

In this Appendix, we describe the time-dependent DMRG method. Steps concerning the construction of the operators are model-specific and are discussed in detail in Section 4.1.1 for the repton model. Here we only go through the basic working principles behind the method, technical details can be found in Ref. [166]. Time-dependent DMRG is based on the normal DMRG, which is often called the ground-state DMRG method, so we begin with that.

Consider a one-dimensional many-particle system (such as a Heisenberg or a repton chain) in a state $|\Psi\rangle$, which is either a wavefunction or a probability distribution for the ground state or the steady state. This is called a target state and more than one target state can be used. Instead of presenting this state in the basis of the full system of all sites, we can alternatively express it as an entangled state of two (or more) subsystems such that $|\Psi\rangle = \sum_{i=1}^{N_1} \sum_{j=1}^{N_2} c_{i,j}|i\rangle \otimes |j\rangle$, where $|i\rangle$ and $|j\rangle$ are basis vectors of separate subsystems and $c_{i,j}$ are coefficients. For one-dimensional systems the natural choice for subsystems is to use left (basis $|i\rangle$) and right (basis $|j\rangle$) parts. Theorem, known as Schmidt decomposition, states that there exists orthonormal basis $|i_1\rangle$ and $|i_2\rangle$ such that $|\Psi\rangle = \sum_{i=1}^{M=\min[N_1,N_2]} \alpha_i |i_1\rangle \otimes |i_2\rangle$ with $\sum_i \alpha_i^2 = 1$. Such decomposition can be found by creating and diagonalizing reduced density operators ρ_1 and ρ_2 with elements $[\rho_1]_{i,i'} = \sum_j c^\dagger_{i,j} c_{i',j}$ and similarly for ρ_2. By the construction ρ_1 and ρ_2 have the same spectrum.[1] This decomposition is at the center of the DMRG method. Coefficients α_i include information about the correlations between subsystems. If there is no correlation, only one of the coefficients is non-zero [127].

Now suppose that we want to use only $n < M$ basis vectors for the first (left) subsystem, *i.e.* we want to find a *truncated* state $|\widetilde{\Psi}\rangle \approx |\Psi\rangle$. By using basic linear algebra, one can show that such truncation minimizing the norm $||\Psi\rangle - |\widetilde{\Psi}\rangle|^2$ is achieved by choosing the states with largest weights α_i. From this partial set of most important eigenstates, one can create a truncated change-of-basis operator, which can be used to truncate states and operators accordingly. Based on this theoretical framework, during 1992-93, White proposed DMRG method to study one-dimensional quantum systems [195]. The proposed algorithms are commonly known as *infinite-size* and *finite-size* algorithms. The infinite-size algorithm is used to construct reduced operators for large systems by starting with a small system, which can still be diagonalized exactly. Then

[1] In practical computations, typically one only needs to find a truncated basis for one of the blocks (the 'system'). Given a target state(s) and block dimension, this can be done without creating decompositions and more than one density matrix.

one increases the system size by adding new sites and using the truncation procedure based on density matrices and Schmidt decomposition. The finite-size algorithm is similar, but instead of increasing the system size, it is used to improve the state and operators created with the infinite-size algorithm.

We now present the basic steps of the infinite-size algorithm, which already includes the central parts of the DMRG method.

1. By using the left and right subsystems, form a superblock Hamiltonian H containing L sites and having dimension $N_1 \times N_2$.
2. Compute the ground/steady state $|\Psi\rangle = \sum_{i=1}^{N_1} \sum_{j=1}^{N_2} c_{i,j}|i\rangle \otimes |j\rangle$ for H.
3. Form the reduced density matrix $\rho_1 = \sum_{i,i'=1}^{N_1} \sum_{j,j'=1}^{N_2} c_{i,j} c^*_{i',j'} |i\rangle\langle i'|$ for the left part and similarly ρ_2 for the right one.
4. Diagonalize ρ's to obtain $n_1 < N_1$ and $n_2 < N_2$ eigenvectors with the largest eigenvalues separately for the left and right part. Using these vectors, create a reduced basis transformation operators O_1 and O_2.
5. Transform Hamiltonians and all associated operators for both subsystems into their reduced eigenbasis using O operators.
6. Add new sites into the newly reduced subsystems. Now the total number of sites in the subsystems is $N + 2$. Goto step 1. Now $L \to L + 2$, $N_1 \to n_1 \times M_1$ and $N_2 \to M_2 \times n_2$, where M_1 and M_2 are the dimensions of new sites (typically $M_1 = M_2$).

To increase the accuracy and stability, infinite-size algorithm should be always accompanied by the finite-size version. The finite-size algorithm is a modification of the above scheme. Instead of increasing the system size, one keeps the system size L fixed all the time and performs 'sweeping'. Sweeping is done by adding new sites into one block while reducing them from the other. Operators for the shrunk blocks are retrieved from the memory in which they were stored during previous steps (either during infinite-size algorithm or previous sweeps). After couple of such sweeps, where both blocks have been fully shrunk and grown, more accurate operators and target state(s) are obtained. See Fig. A.1 for an illustration of the both infinite-size algorithm and sweeping.

Dividing the system into smaller parts and then using the information of all parts to reduce the subsystems is the key idea of the DMRG method. The amount of entanglement between subsystems regulate the success of the truncation [7]. Basis truncation is kept under a given *truncation tolerance*, which is typically small (*e.g.* $\sim 10^{-10}$). This is the single most important parameter in the method. Block sizes are

increased step-by-step and it is required that the operators can be build recursively. The size of the reduced basis must remain small, typically less than a hundred or so. Due to its working principle, DMRG can be efficiently applied only to one-dimensional systems with short interaction lengths. There has been attempts to extend DMRG technique to include two-dimensional systems and more complicated many-particle interactions, but with poor results. The best performance is received for open system, although periodic systems can be also handled with less precision.

Instead of targeting the ground or steady states, one can also target time-dependent states. This is the case with the time-dependent DMRG method which uses Runge-Kutta approach [58]. After computing the target state $|\Psi(t)\rangle$ at $t = 0$ using time-step Δt and the infinite and finite-size algorithms, one can compute

$$\begin{aligned}
|k_1\rangle &= \Delta t H(t)|\Psi(t)\rangle \\
|k_2\rangle &= \Delta t H(t + \Delta t/2)\left[|\Psi(t)\rangle + 1/2|k_1\rangle\right] \\
|k_3\rangle &= \Delta t H(t + \Delta t/2)\left[|\Psi(t)\rangle + 1/2|k_2\rangle\right] \\
|k_4\rangle &= \Delta t H(t + \Delta t)\left[|\Psi(t)\rangle + |k_3\rangle\right].
\end{aligned}$$

Using these, approximations for the intermediate states are

$$\begin{aligned}
|\Psi(t + \Delta t/3)\rangle &\approx |\Psi(t)\rangle + \frac{1}{162}\left[31|k_1\rangle + 14|k_2\rangle + 14|k_3\rangle - 5|k_4\rangle\right] \\
|\Psi(t + 2\Delta t/3)\rangle &\approx |\Psi(t)\rangle + \frac{1}{81}\left[16|k_1\rangle + 20|k_2\rangle + 20|k_3\rangle - 2|k_4\rangle\right] \\
|\Psi(t + \Delta t)\rangle &\approx \frac{1}{6}\left[|k_1\rangle + 2|k_2\rangle + 2|k_3\rangle + |k_4\rangle\right],
\end{aligned}$$

which are used as the target states. After sweeping, all operators are well adapted to these states and one can advance $t + \Delta t$ in time and repeat the process.

During the past 20 years a large number of modifications and improvements of these original algorithms have been proposed, involving different block arrangements, finite-temperature extension, state estimation and better targeting, time-development and technical improvements. More recently, focus has shifted towards matrix product state formalism, instead of working with matrices and vectors as presented here. This has lead to new extension of the DMRG method and better theoretical understanding how it works [166].

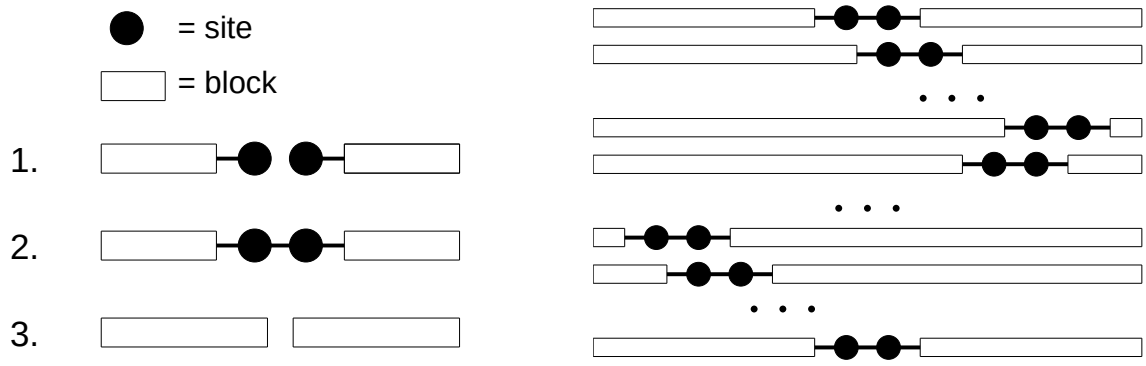

Figure A.1: Illustrations of the DMRG procedures. On the left, one iteration of the infinite-system DMRG algorithm is shown: (1) Free sites are added in left and right blocks, (2) the super-block is formed and a target state (e.g. the steady state) is solved, (3) both blocks are renormalized. On the right, one complete 'sweeping' for the finite-size algorithm and time-dependent DMRG is shown.

B Derivation of equations (4.2) and (4.3)

In this Section we derive equations (4.2) and (4.3), which are valid for any finite master equation system. The derivation follows the seminal work by Derrida [46] and later works closely related to it, such as [64, 26, 101, 178]. For a general system, we are only able to derive the equations which are to be solved using numerical methods. See also Ref. [188] where similar derivation is done for the discretized Fokker-Planck equation.

Let us consider a finite discrete stochastic system with states $y \in \{1, 2, \ldots, N\}$ and let us define a real-valued counting process x, such as the displacement of the center-of-mass, given by an antisymmetric matrix D, *i.e.* moving from state i to j increases (or decreases) the counter by $D_{j,i}$ and with $D_{i,i} = 0$ and no branching. Then for an ergodic system, one can start from any state and construct the relative spatial positions of all N states using D, this defines values $x_y \in \mathbb{R}$ for the counter. Let the primitive period of the counter be $L > 0$ and define $x_y^l := x_y + Ll$ with $l \in \mathbb{Z}$. This means, that in the configuration graph of the model, there exists one or more simple cycles C such that $\sum_{\langle i,j\rangle \in C} D_{i,j} = L$. For the center-of-mass transport in particle models, one may conclude that there cannot be simple cycles with a different L, because the period is bind to the displacement of the center-of-mass, which results from a precise number if single particle moves (*e.g.* reptons or atoms)[1]. However, this is merely a technical requirement to simplify the derivation. As we will see, expressions for $v(t)$ and $D_{\text{eff}}(t)$ only depend on H and D. Finally, note that one can have $x_{y'}^{l'} = x_y^l$ for some $l' \neq l$ and/or $y' \neq y$. This is typically the case when the configuration graph has a complicated structure.

Let the joint probability for a state y in a period l be given by p_y^l with its time-evolution given by the master equation

$$\frac{dp_y^l(t)}{dt} = \sum_{y'} \left[H_{y,y'} p_{y'}^{l+f(y,y')}(t) - H_{y',y} p_y^l(t) \right],$$

where $H_{y,y} = 0$ and the anti-symmetric function f takes values $\{-1, 0, 1\}$, depending on whether the state y' actually belongs to the previous $(l-1)$, the same (l) or the next

[1] Because $|x_l^k - x_l^y|$ is fixed for all l, the assumption of two or more different periods immediately leads to a contradiction

$(l+1)$ period. This 'bookkeeping' function depends on how one chooses x_y. However, as we will see, it has no effect on the final results because it will disappear in the summation over all periods l. The n^{th} moment of the counter is

$$\langle x^n(t)\rangle = \sum_{l=-\infty}^{\infty} \sum_{y} \left(x_y^l\right)^n p_y^l(t).$$

Definitions for the velocity and the effective diffusion coefficient are given in Section 3.2.1. After these preliminaries, let us begin the derivation by defining following auxiliary functions

$$\begin{aligned} q_y(t) &= \sum_{l=-\infty}^{\infty} p_y^l(t) \\ s_y(t) &= \sum_{l=-\infty}^{\infty} x_y^l p_y^l(t) - \langle x(t)\rangle q_y(t), \end{aligned}$$

where $x(t)$ is the value of the counter at time t. One can see that conditions $\sum_y q_y = 1$ and $\sum_y s_y = 0$ hold. From now on, we drop the explicit t-dependency to simplify the notation. Taking time derivative and using master equations, we have

$$\begin{aligned} \dot{q_y} &= \sum_{l=-\infty}^{\infty} \sum_{y'} \left[H_{y,y'} p_{y'}^{l+f(y,y')} - H_{y',y} p_y^l\right] = \sum_{y'} \left[H_{y,y'} q_{y'} - H_{y',y} q_y\right] \\ \dot{s_y} &= \sum_{l=-\infty}^{\infty} x_y^l \sum_{y'} \left[H_{y,y'} p_{y'}^{l+f(y,y')} - H_{y',y} p_y^l\right] - \frac{d\langle x\rangle}{dt} q_y - \langle x\rangle \dot{q_y}. \end{aligned}$$

For the value of the counter, we can write $x_y^l = x_{y'}^{l+f(y,y')} + D_{y,y'}$ for states y' reachable from y. Now we can re-arrange terms

$$\begin{aligned} \dot{s_y} = &\sum_{l=-\infty}^{\infty} \sum_{y'} \left[H_{y,y'} \left(x_{y'}^{l+f(y,y')} + D_{y,y'}\right) p_{y'}^{l+f(y,y')} - H_{y',y} x_y^l p_y^l\right] - \langle x\rangle \sum_{y'} \left[H_{y,y'} q_{y'} - H_{y',y} q_y\right] \\ &- \frac{d\langle x\rangle}{dt} q_y \\ = &\sum_{y'} H_{y,y'} \left[\sum_{l=-\infty}^{\infty} x_{y'}^{l+f(y,y')} p_{y'}^{l+f(y,y')} - \langle x\rangle q_{y'}\right] - \sum_{y'} H_{y',y} \left[\sum_{l=-\infty}^{\infty} x_y^l p_y^l - \langle x\rangle q_y\right] \\ &+ \sum_{y'} H_{y,y'} D_{y,y'} \sum_{l=-\infty}^{\infty} p_{y'}^{l+f(y,y')} - \frac{d\langle x\rangle}{dt} q_y \\ = &\sum_{y'} \left[H_{y,y'} s_{y'} - H_{y',y} s_y + H_{y,y'} D_{y,y'} q_{y'}\right] - \frac{d\langle x\rangle}{dt} q_y. \end{aligned}$$

Time-derivatives of the first two moments can be now computed.

$$\begin{aligned}
v(t) = \frac{d\langle x(t)\rangle}{dt} &= \sum_{l=-\infty}^{\infty} \sum_{y'} x_{y'}^{l} \sum_{y} \left[H_{y',y} p_{y}^{l+f(y',y)} - H_{y,y'} p_{y'}^{l} \right] \\
&= \sum_{y} \sum_{y'} \sum_{l=-\infty}^{\infty} \left[x_{y}^{l+f(y',y)} H_{y',y} p_{y}^{l+f(y',y)} + D_{y',y} H_{y',y} p_{y}^{l} - x_{y'}^{l} H_{y,y'} p_{y'}^{l} \right] \\
&= \sum_{y} \sum_{y'} D_{y',y} H_{y',y} \sum_{l=-\infty}^{\infty} p_{y}^{l} \\
&= \sum_{y'} \sum_{y} D_{y',y} H_{y',y} q_{y}.
\end{aligned}$$

By using identity $\left(x_{y'}^{l}\right)^2 = \left(x_{y}^{l+f(y',y)}\right)^2 + 2D_{y',y} x_{y}^{l+f(y',y)} + D_{y',y}^2$, we get

$$\begin{aligned}
\frac{d\langle x(t)^2\rangle}{dt} &= \sum_{l=-\infty}^{\infty} \sum_{y'} \left(x_{y'}^{l}\right)^2 \sum_{y} \left[H_{y',y} p_{y}^{l+f(y',y)} - H_{y,y'} p_{y'}^{l} \right] \\
&= \sum_{l=-\infty}^{\infty} \sum_{y} \sum_{y'} \Bigg\{ \left[\left(x_{y}^{l+f(y',y)} \right)^2 + 2D_{y',y} x_{y}^{l+f(y',y)} + D_{y',y}^2 \right] H_{y',y} p_{y}^{l+f(y',y)} \\
&\quad - \left(x_{y'}^{l}\right)^2 H_{y,y'} p_{y'}^{l} \Bigg\} \\
&= \sum_{l=-\infty}^{\infty} \sum_{y} \sum_{y'} \left[2D_{y',y} x_{y}^{l+f(y',y)} + D_{y',y}^2 \right] H_{y',y} p_{y}^{l+f(y',y)} \\
&= 2 \sum_{y} \sum_{y'} D_{y',y} H_{y',y} \sum_{l=-\infty}^{\infty} x_{y}^{l} p_{y}^{l} + \sum_{y} \sum_{y'} D_{y',y}^2 H_{y',y} q_{y}.
\end{aligned}$$

Inserting these into the definition of $D_{\text{eff}}(t)$, with $d = 1$, we get

$$\begin{aligned}
D_{\text{eff}}(t) &= \frac{1}{2} \frac{d\langle x(t)^2\rangle}{dt} - \langle x(t)\rangle \frac{d\langle x(t)\rangle}{dt} \\
&= \sum_{y} \sum_{y'} D_{y',y} H_{y',y} \sum_{l=-\infty}^{\infty} x_{y}^{l} p_{y}^{l} + \frac{1}{2} \sum_{y} \sum_{y'} D_{y',y}^2 H_{y',y} q_{y} - \langle x \rangle \sum_{y'} \sum_{y} D_{y',y} H_{y',y} q_{y} \\
&= \sum_{y} \sum_{y'} D_{y',y} H_{y',y} \left[\sum_{l=-\infty}^{\infty} x_{y}^{l} p_{y}^{l} - \langle x \rangle q_{y} \right] + \frac{1}{2} \sum_{y} \sum_{y'} D_{y',y}^2 H_{y',y} q_{y} \\
&= \sum_{y} \sum_{y'} D_{y',y} H_{y',y} s_{y} + \frac{1}{2} \sum_{y} \sum_{y'} D_{y',y}^2 H_{y',y} q_{y}.
\end{aligned}$$

In the case of time-independent H, taking the limit $t \to \infty$ gives the long-time velocity and diffusion coefficient for the center-of-mass transport. For time-dependent systems, integration over time is required.

References

[1] R. K. Ahuja, T. L. Magnanti, and J. B. Orlin: *Network Flows: Theory, Algorithms, and Applications*, Prentice Hall, New Jersey (1993).

[2] B.-Q. Ai and L.-G. Liu: *Current in a three-dimensional periodic tube with unbiased forces*, Phys. Rev. E **74**, 051114 (2006); D. Reguera, G. Schmid, P. S. Burada, J. M. Rubi, P. Reimann, and P. Hänggi: *Entropic Transport: Kinetics, Scaling, and Control Mechanisms*, Phys. Rev. Lett. **96**, 130603 (2006); P. S. Burada, G. Schmid, Y. Li, P. Hänggi: *Controlling diffusive transport in confined geometries*, Acta Physica Polonica B **41**, 935 (2010);

[3] B.-Q. Ai , X.-J. Wang, G.-T. Liu, H.-Z. Xie, D.-H. Wen, W. Chen, and L.-G. Liu: *Current reversals in an inhomogeneous system with asymmetric unbiased fluctuations*, Eur. Phys. J. B **37**, 523 (2004).

[4] R. Ait-Haddou and W. Herzog: *Brownian Ratchet Models of Molecular Motors*, Cell Biochemistry and Biophysics **38**, 191 (2003).

[5] T. Ala-Nissilä, R. Ferrando, and S. C. Ying: *Collective and single particle diffusion on surfaces*, Advances in Physics **51**, 949 (2002).

[6] D. Aldous and J. A. Fill: *Reversible Markov chains and random walks on graphs*, (unpublished), `http://www.stat.berkeley.edu/~aldous/RWG/book.html`.

[7] L. Amico, R. Fazio, A. Osterloh, V. Vedra: *Entanglement in many-body systems*, Rev. Mod. Phys. **80**, 517 (2008).

[8] D. Andrieux and P. Gaspard: *Fluctuation Theorem for Currents and Schnakenberg Network Theory*, J. Stat. Phys. **127**, 107 (2007); D. Andrieux and P. Gaspard: *Network and thermodynamic conditions for a single macroscopic current fluctuation theorem*, C. R. Physique **8**, 579 (2007); J. L. Lebowitz and H. Spohn: *A Gallavotti-Cohen-Type Symmetry in the Large Deviation Functional for Stochastic Dynamics*, Journal of Statistical Physics **95**, 333 (1999); D. Andrieux and P. Gaspard: *Fluctuation theorem for transport in mesoscopic systems*, J. Stat. Mech. **1**, P01011 (2006).

[9] U. M. Ascher, R. M. M. Mattheij, and R. D. Russell: *Numerical Solution of Boundary Value Problems for Ordinary Differential Equations*, SIAM, Philadelphia (1995).

[10] R. Ashton, C. Padalay and R. S. Kanez: *Microfluidic separation of DNA*, Current Opinion in Biotechnology **14**, 497 (2003).

[11] R. D. Astumian: *Thermodynamics and Kinetics of Molecular Motors*, Biophysical Journal **98**, 2401 (2010); R. D. Astumian: *Design Principles for Brownian Molecular Machines: How to Swim in Molasses and Walk in a Hurricane*, Phys. Chem. Chem. Phys. **9**, 5067 (2007).

[12] R. D. Astumian and M. Bier: *Fluctuation driven ratchets: molecular motors*, Phys. Rev. Lett. **72**, 1766 (1994).

[13] J. S. Bader, R. W. Hammond, S. A. Henck, M. W. Deem, G. A. McDermott, J. M. Bustillo, J. W. Simpson, G. T. Mulhern, and J. M. Rothberg: *DNA transport by a micromachined Brownian ratchet device*, Proc. Natl. Acad. Sci. USA **96**, 13165 (1999); R. W. Hammond, J. S. Bader, S. A. Henck, M. W. Deem, G. A. McDermott, J. M. Bustillo, and J. M. Rothberg: *Differential transport of DNA by a rectified Brownian motion device*, Electrophoresis **21**, 74 (2000); J. S. Bader, M. W. Deem, R. W. Hammond, S. A. Henck, J. W. Simpson, and J. M. Rothberg: *A Brownian-ratchet DNA pump with applications to single-nucleotide polymorphism genotyping*, Appl. Phys. A: Mater. Sci. Process. **75**, 275 (2002).

[14] M. Badoual, F. Julicher, and J. Prost: *Bidirectional cooperative motion of molecular motors*, Proc. Natl. Acad. Sci. USA **99**, 6696 (2002).

[15] V. Balakrishnan: *Schaum's Outline of Graph Theory*, McGrawn-Hill, New York (1997); J. Bang-Jensen and G. Gutin: *Digraphs: Theory, Algorithms and Applications*, Springer-Verlag, London (2009).

[16] A. Barrat, M. Barthelemy, and A. Vespignani: *Dynamical processes on complex networks*, Cambridge University Press, Cambridge (2008).

[17] R. Barrett, M. Berry, T. F. Chan, J. Demmel, J. Donato, J. Dongarra, V. Eijkhout, R. Pozo, C. Romine, and H. Van der Vorst: *Templates for the Solution of Linear Systems: Building Blocks for Iterative Methods*, SIAM, Philadelphia (1994).

[18] F. Berger, T. Schmiedl, and U. Seifert: *Optimal potentials for temperature ratchets*, Phys. Rev. E **79**, 031118 (2009).

[19] V. Bermudez, N. Capron, T. Gase, F. G. Gatti, F. Kajzar, D. A. Leigh, F. Zerbetto, and S. Zhang: *Influencing intramolecular motion with an alternating electric field*, Nature **406**, 605 (2000); A. Credi: *Artificial Molecular Motors Powered by Light*, Aust. J. Chem. **59**, 157 (2006).

[20] L. Bitar, P. A. Serena, P. Garcia-Mochales, N. Garcia, and Vu Thien Binh: *Mechanism for diffusion of nanostructures and mesoscopic objects on surfaces*, Surf. Sci. **339**, 221 (1995).

[21] B. Bortz, M. H. Kalos, and J. L. Lebowitz: *A new algorithm for Monte Carlo simulation of Ising spin systems*, J. Comput. Phys. **17**, 10 (1975).

[22] M. van den Broek, R. Eichhorn, and C. Van den Broeck: *Intrinsic ratchets*, Europhys. Lett. **86**, 30002 (2009).

[23] M. O. Caceres and A. M. Lobos: *Theory of eigenvalues for periodic non-stationary Markov processes: the Kolmogorov operator and its applications*, J. Phys. A: Math. Gen. 39, 1547 (2006).

[24] A. M. Cadilhe, C. R. Stoldt, C. J. Jenks, P. A. Thiel, and J. W. Evans: *Evolution of far-from-equilibrium nanostructures on Ag(100) surfaces: Protrusions and indentations at extended step edges*, Phys. Rev. B **61**, 4910 (2000); S. Pal and K. A. Fichthorn: *Size dependence of the diffusion coefficient for large adsorbed clusters*, Phys. Rev. B **60**, 7804 (1999); H. Mehl, O. Biham, I. Furman, and M. Karimi: *Models for adatom diffusion on fcc (001) metal surfaces*, Phys. Rev. B **60**, 2106 (1999); X. Wang, F. Xie, Q. Shi, and T. Zhao: *Effect of atomic diagonal motion on cluster diffusion coefficient and its scaling behavior*, Surf. Sci. **561**, 25 (2004);

[25] E. Carlon, A. Drzewinski, and J. M. J. van Leeuwen: *Reptation in the Rubinstein-Duke model: The influence of end-reptons dynamics*, J. Chem. Phys. **117**, 2425 (2002).

[26] J. Casado-Pascual: *Flux reversal in a simple random-walk model on a fluctuating symmetric lattice*, Phys. Rev. E **74**, 021112 (2006).

[27] D. Chandler: *Introduction to modern statistical mechanics*, Oxford University Press, New York (1987).

[28] A. Chatterjee and D. G. Vlachos: *An overview of spatial microscopic and accelerated kinetic Monte Carlo methods*, J. Computer-Aided Mater. Des. **14**, 253 (2007); J. L. Blue, I. Beichl, and F. Sullivan: *Faster Monte Carlo simulations*, Phys. Rev. E **51**, R867 (1995).

[29] V. Y. Chernyak and N. A. Sinitsyn: *Pumping Restriction Theorem for Stochastic Networks*, Phys. Rev. Lett. **101**, 160601 (2008); N. A. Sinitsyn: *The stochastic pump effect and geometric phases in dissipative and stochastic systems*, J. Phys. A: Math. Theor. **42**, 193001 (2009); S. Rahav, J. Horowitz, and C. Jarzynski: *Directed Flow in Nonadiabatic Stochastic Pumps*, Phys. Rev. Lett. **101**, 140602 (2008).

[30] J.-Y. Chen, D. R. Kincaid, and D. M. Young: *Generalizations and modifications of the GMRES iterative method*, Numerical Algorithms **21**, 119 (1999).

[31] H. Chen, Q. Wang, and Z. Zheng: *Deterministic directed transport of inertial particles in a flashing ratchet potential*, Phys. Rev. E **71**, 031102 (2005).

[32] Y. D. Chen, B. Yan, and R. Miura: *Asymmetry and direction reversal in fluctuation-induced biased Brownian motion*, Phys. Rev. E **60**, 3771 (1999).

[33] T. Chou, K. Mallick, and R. K. P. Zia: *Non-equilibrium statistical mechanics: from a paradigmatic model to biological transport*, Rep. Prog. Phys. **74**, 116601 (2011).

[34] D. Chowdhury, A. Schadschneider, and K. Nishinari: *Physics of Transport and Traffic Phenomena in Biology: from molecular motors and cells to organisms*, Phys. of Life Reviews **2**, 318 (2005).

[35] B. E. Clancy, W. M. Behnke-Parks, J. O. L. Andreasson, S. S. Rosenfeld, and S. M. Block: *A universal pathway for kinesin stepping*, Nature structural and molecular biology **18**, 1020 (2011); R. Lipowsky, S. Liepelt, and A. Valleriani: *Energy Conversion by Molecular Motors Coupled to Nucleotide Hydrolysis*, J. Stat. Phys. **135**, 951 (2009).

[36] N. Combe and H. Larralde: *Low-temperature shape relaxation of two-dimensional islands by edge diffusion*, Phys. Rev. B **62**, 16074 (2000); P. Jensen, N. Combe, H. Larralde, J. L. Barrat, C. Misbah, and A. Pimpinelli: *Kinetics of shape equilibration for two dimensional islands*, Eur. Phys. J. B **11**, 497 (1999); Da-Jiang Liu and J. W. Evans: *Sintering of two-dimensional nanoclusters in metal.100. homoepitaxial systems: Deviations from predictions of Mullins continuum theory*, Phys. Rev. B **66**, 165407 (2002).

[37] A. R. Conn, K. Scheinberg, and L. N. Vicente: *Introduction to derivative-free optimization*, SIAM, Philadelphia (2009).

[38] E. M. Craig, M. J. Zuckermann, and H. Linke: *Mechanical coupling in flashing ratchets*, Phys. Rev. E **73**, 051106 (2006).

[39] W. J. Culver: *On the Existence and Uniqueness of the Real Logarithm of a Matrix*, Proceedings of the American Mathematical Society **17**, 1146 (1966).

[40] A. Dasdan: *Experimental Analysis of the Fastest Optimum Cycle Ratio and Mean Algorithms*, ACM Transactions on Design Automation of Electronic Systems **9**, 385 (2004).

[41] A. Dasdan and R. K. Gupta: *Faster maximum and minimum mean cycle algorithms for system-performance analysis*, IEEE transactions on computer-aided design of integrated circuits and systems **17**, 889 (1998);

[42] A. Dasdan, S. S. Irani, and R. K. Gupta: *Efficient algorithms for optimum cycle mean and optimum cost to time ratio problems*, Proceedings of the 36$^{\text{th}}$ ACM/IEEE conference on Design automation, 37 (1999).

[43] T. A. Davis: *Direct Methods for Sparse Linear Systems*, SIAM, Philadelphia (2006).

[44] T. Dayar and W. J. Steward: *Comparison of partitioning techniques for two-level iterative solvers on large, sparse Markov chains*, SIAM Journal on Scientific Computing **21**, 1691 (2000).

[45] I. Derenyi, M. Bier, and R. D. Astumian: *Generalized Efficiency and its Application to Microscopic Engines*, Phys Rev. Lett. **83**, 903 (1999).

[46] B. Derrida: *Velocity and diffusion constant of a periodic one-dimensional hopping model*, J. Stat. Phys. **31**, 433 (1983).

[47] B. Derrida: *Non-equilibrium steady states: fluctuations and large deviations of the density and of the current*, J. Stat. Mech. **07**, P07023 (2007).

[48] R. Dickman: *Numerical analysis of the master equation*, Phys. Rev. E **65**, 047701 (2002).

[49] L. Dinis: *Optimal sequence for Parrondo games*, Phys. Rev. E **77**, 021124 (2008).

[50] J. R. Dormand and P. J. Prince: *A family of embedded Runge-Kutta formulae*, J. Comp. Appl. Math. **6**, 19 (1980).

[51] S. Dorosz and M. Pleimling: *Characterizing steady-state and transient properties of reaction-diffusion systems*, Phys. Rev. E **80**, 061114 (2009); D. ben-Avraham, S. Dorosz, and M. Pleimling: *Realm of validity of the Crooks relation*, Phys. Rev. E **83**, 041129 (2011).

[52] A. Drzewinski and J. M. J. van Leeuwen: *Field induced orientation of reptating polymers*, J. Stat. Mech. **2**, P02004 (2005).

[53] A. Drzewinski and J. M. J. van Leeuwen: *Crossover from reptation to Rouse dynamics in a one-dimensional model*, Phys. Rev. E **73**, 061802 (2006); A. Drzewinski and J. M. J. van Leeuwen: *Crossover from reptation to Rouse dynamics in the extended Rubinstein-Duke model*, Phys. Rev. E **77**, 031802 (2008).

[54] M. T. Downton, M. J. Zuckermann, E. M. Craig, M. Plischke, and H. Linke: *Single-polymer Brownian motor: A simulation study*, Phys. Rev. E **73**, 011909 (2006).

[55] T. A. J. Duke: *Tube model of field-inversion electrophoresis*, Phys. Rev. Lett. **62**, 2877 (1989).

[56] A. Efremov and Z. Wang: *Universal optimal working cycles of molecular motors*, Phys. Chem. Chem. Phys. **13**, 6223 (2011).

[57] M. Esposito and K. Lindenberg: *Continuous-time random walk for open systems: Fluctuation theorems and counting statistics*, Phys. Rev. E **77**, 051119 (2008).

[58] A. Feiguin and S. R. White: *Time-step targeting methods for real-time dynamics using the density matrix renormalization group*, Phys. Rev. B **72**, 020404 (2005).

[59] M. Feito and F. J. Cao: *Optimal operation of feedback flashing ratchets*, J. Stat. Mech. **1**, P01031 (2009).

[60] A. J. Fendrik, L. Romanelli, and R. P. J. Perazzo: *Collective modes in a coupled ratchet model*, Physica A: Statistical Mechanics and its Applications **368**, 7 (2006).

[61] H. Feng, B. Han, and J. Wang: *Dominant Kinetic Paths of Complex systems: Gene Networks*, J. Phys. Chem. Lett. **1**, 1836 (2010).

[62] R. P. Feynman, R. B. Leighton, and M. Sands: *The Feynman Lectures on Physics*, Pearson/Addison-Wesley, San Francisco (2006).

[63] T. J. Frankcombe and S. C. Smith: *Numerical solution methods for large, difficult kinetic master equations*, Theor. Chem. Acc. **124**, 303 (2009).

[64] J. A. Freund and L. Schimansky-Geier: *Diffusion in discrete ratchets*, Phys. Rev. E **60**, 1304 (1999).

[65] F. R. Gantmacher: *The theory of matrices*, AMS Chelsea Publishing, Providence (2000).

[66] C. W. Gardiner: *Handbook of Stochastic Methods: for Physics, Chemistry and the Natural Sciences*, Springer-Verlag, Berlin (2004); N. G. Van Kampen: *Stochastic processes in physics and chemistry*, Elsevier, Amsterdam (2007).

[67] P. G. de Gennes: *Scaling Concepts in Polymer Physics*, Cornell University Press, Ithaca (1979).

[68] S. von Gehlen, M. Evstigneev, and P. Reimann: *Dynamics of a dimer in a symmetric potential: Ratchet effect generated by an internal degree of freedom*, Phys. Rev. E **77**, 031136 (2008).

[69] G. H. Golub and C. F. Van Loan: *Matrix computations*, The Johns Hopkins University Press, Baltimore (1996).

[70] M. Gorissen and C. Vanderzande: *Finite size scaling of current fluctuations in the totally asymmetric exclusion process*, Journal Of Physics A: Mathematical and theoretical **44**, 115005 (2011); M. Gorissen, J. Hooyberghs, and C. Vanderzande: *Density-matrix renormalization-group study of current and activity fluctuations near nonequilibrium phase transitions*, Phys. Rev. E **79**, 020101 (2009).

[71] A. Greenbaum: *Iterative methods for solving linear systems*, SIAM, Philadelphia (1997).

[72] G. A. Griess, E. Rogers, and P. Serwer: *Application of the concept of an electrophoretic ratchet*, Electrophoresis **22**, 981 (2001).

[73] G. Grimmett and D. Stirzaker: *Probability and random processes*, Oxford university press, Oxford (2001).

[74] I. Griva, S. G. Nash, and A. Sofer: *Linear and nonlinear optimization*, SIAM, Philadelphia (2009).

[75] S. R. de Groot and P. Mazur: *Non-equilibrium thermodynamics* Dover publications, New York (1984).

[76] R. J. Harris and G. M. Schütz: *Fluctuation theorems for stochastic dynamics*, J. Stat. Mech. **7**, P07020 (2007).

[77] F. Haußer, P. Kuhn, J. Krug, and A. Voigt: *Morphological stability of electromigration-driven vacancy islands*, Phys. Rev. E **75**, 046210 (2007).

[78] Y. He and J. G. Che: *Electric-field effects on the diffusion of Si and Ge adatoms on Si(001) studied by density functional simulations*, Phys. Rev. B **79**, 235430 (2009); J. M. Carpinelli and B. S. Swartzentruber: *Direct measurement of field effects on surface diffusion*, Phys. Rev. B **58**, R13423 (1998); G. L. Kellogg: *Electric field inhibition and promotion of exchange diffusion on Pt(001)*, Phys. Rev. Lett. **70**, 1631 (1993); F. Dulot, J. Eugene, B. Kierren, and D. Malterre: *STM-TIP induced surface diffusion of copper on copper (100)*, Applied Surface Science **162-163**, 86 (2000); M. R. Sørensen, K. W. Jacobsen, and H. Jónsson: *Thermal Diffusion Processes in Metal-Tip-Surface Interactions: Contact Formation and Adatom Mobility*, Phys. Rev. Lett. **77**, 5067 (1996); L. M. Sanders, R. Stumpf, T. R. Mattsson, and B. S. Swartzentruber: *Changing the Diffusion Mechanism of Ge-Si Dimers on Si(001) using an Electric Field*, Phys. Rev. Lett. **91**, 206104 (2003); S. V. Kolesnikov, A. L. Klavsyuk, and A. M. Saletsky: *Vacancy formation on stepped Cu(100) accelerated with STM: Molecular dynamics and kinetic Monte Carlo simulations*, Phys. Rev. B **80**, 245412 (2009); K. Pottinga, N. B. Luquea, P. M. Quainoa, H. Ibachb, and W. Schmickler: *Island dynamics on charged silver electrodes: Kinetic Monte-Carlo simulations*, Electrochimica Acta **54**, 4494 (2009).

[79] J. Heinonen: *Diffusion and growth of steps and islands on surfaces*, Dissertation 110, Helsinki University Of Technology (2001).

[80] J. Heinonen, I. T. Koponen, J. Merikoski, and T. Ala-Nissilä: *Island Diffusion on Metal fcc(100) Surfaces*, Phys. Rev. Lett. **82**, 2733 (1999); J. Heinonen, I. T. Koponen, P. Salo, and T. Ala-Nissilä: *Time correlations and statistics*

of atomistic processes in island diffusion on fcc(100) metal surfaces, Surf. Sci. **507-510**, 146 (2002).

[81] W.-K. Ching and M. K. Ng: *Markov Chains: Models, Algorithms and Applications*, Spinger, New York (2006); D. Helbing: *Traffic and related self-driven many-particle systems*, Rev. Mod. Phys. **73**, 1067 (2001).

[82] V. Hernandez, J. E. Roman, A. Tomas, and V. Vidal: *A Survey of Software for Sparse Eigenvalue Problems*, SLEPc Technical Report STR-6 (`www.grycap.upv.es/slepc`) (2007).

[83] R. A. Howard: *Dynamic programming and Markov processes*, The M.I.T. Press, Cambridge (1960); J. Cochet-Terrason, G. Cohen, S. Gaubert, M. McGettrick, and J. P. Quadrat: *Numerical computation of spectral elements in max-plus algebra*, IFAC Conference on System Structure and Control, Pergamon press (1998).

[84] P. Hänggi, P. Talkner, and M. Borkovec: *Reaction rate theory - 50 years after Kramers*, Rev. Mod. Phys. **64**, 251 (1990).

[85] P. Hänggi and F. Marchesoni: *Artificial Brownian motors: Controlling transport on the nanoscale*, Rev. Mod. Phys. **81**, 387 (2009).

[86] H. Ibach: *Physics of Surfaces and Interfaces*, Springer (2006).

[87] K. R. James: *Convergence of matrix iterations subject to diagonal dominance*, SIAM J. Numer. Anal. **10**, 478 (1973).

[88] A. P. V. Jansen: *An Introduction To Monte Carlo Simulations Of Surface Reactions*, (unpublished) `arXiv:cond-mat/0303028v1` (2003).

[89] C. Jarzynski and O. Mazonka: *Feynman's ratchet and pawl: An exactly solvable model*, Phys. Rev. E **59**, 6448 (1999).

[90] I. Jensen: *Enumerations of Lattice Animals and Trees*, J. Stat. Phys. **102**, 865 (2001).

[91] D. B. Johnson: *Find all the elementary circuits of a directed graph*, J. SIAM **4**, 77 (1975); R. Tarjan: *Enumeration of the elementary circuits of a directed graph*, J. SIAM **3**, 211 (1973).

[92] K. Kawasaki: *Diffusion constants near the critical point for time-dependent ising models*, Phys. Rev. B **145**, 224 (1966).

[93] E. R. Kay, D. A. Leigh, and F. Zerbetto: *Synthetic molecular motors and mechanical machines*, Angew. Chem. Int. Ed. **46**, 72 2007; W. B. Sherman and N. C. Seeman: *A Precisely Controlled DNA Biped Walking Device*, Nano Letters

4, 1203 (2004); Z. Wang: *Bio-inspired track-walking molecular motors (Perspective)*, Biointerphases **5**, FA63 (2010); E. H. C. Bromley, N. J. Kuwada, M. J. Zuckermann, R. Donadini, L. Samii, G. A. Blab, G. J. Gemmen, B. J. Lopez, P. M. G. Curmi, N. R. Forde, D. N. Woolfson, and H. Linke: *The Tumbleweed: towards a synthetic protein motor*, HFSP Journal **3**, 204 (2009); N. J. Kuwada, M. J. Zuckermann, E. H. C. Bromley, R. B. Sessions, P. M. G. Curmi, N. R. Forde, D. N. Woolfson, and H. Linke: Tuning the performance of an artificial protein motor, Phys. Rev. E **84**, 031922 (2011); R. Pei, S. K. Taylor, D. Stefanovic, S. Rudchenko, T. E. Mitchell, and M. N. Stojanovic: *Behavior of Polycatalytic Assemblies in a Substrate-Displaying Matrix*, J. Am. Chem. Soc. **128**, 12693 (2006).

[94] J. Keizer: *On the solutions and the steady states of a master equation*, J. Stat. Phys. **6**, 67 (1972).

[95] F. P. Kelly: *Reversibility and Stochastic Networks*, Wiley, Chichester (1979).

[96] V. M. Kenkre, E. W. Montroll, and M. F. Shlesinger: *Generalized Master Equations for Continuous-Time Random Walks*, J. Stat. Phys. **9**, 45 (1973); U. Landman, E. W. Montroll, and M. F. Shlesinger: *Random walks and generalized master equations with internal degrees of freedom*, Proc. Natl. Acad. Sci. **74**, 430 (1977).

[97] M. Kenward and G. W. Slater: *Polymer deformation in Brownian ratchets: Theory and molecular dynamics simulations*, Phys. Rev. E **78**, 051806 (2008).

[98] S. Y. Kim, I.-H. Lee, and S. Jun: *Transition-pathway models of atomic diffusion on fcc metal surfaces II: Stepped surfaces*, Phys. Rev. B **76**, 245408 (2007).

[99] S. Klamt and A. von Kamp: *Computing paths and cycles in biological interaction graphs*, BMC Bioinformatics **10**, 181 (2009).

[100] S. Klumpp, A. Mielke, and C. Wald: *Noise-induced transport of two coupled particles*, Phys. Rev. E **63**, 031914 (2001).

[101] A. Kolomeisky: *Exact results for parallel-chain kinetic models of biological transport*, J. Chem. Phys. **115**, 7253 (2001); A. B. Kolomeisky and M. E. Fisher: *Periodic sequential kinetic models with jumping, branching and deaths*, Physica A **279**, 1 (2000).

[102] A. B. Kolomeisky and A. Drzewiski: *Polymer dynamics in repton model at large fields*, J. Chem. Phys. **120**, 7784 (2004).

[103] A. B. Kolomeisky and B. Widom: *An invariance property of the repton model*, Physica A **229**, 53 (1996).

[104] A. Kooiman and J. M. J. Van Leeuwen: *The drift velocity in reptation models for electrophoresis*, J. Chem. Phys. **99**, 2247 (1993).

[105] B. Korte and J. Vygen: *Combinatorial Optimization: Theory and Algorithms*, Springer (2007).

[106] M. Kostur and J. Luczka: *Multiple current reversal in Brownian ratchets*, Phys. Rev. E **63**, 021101 (2001).

[107] H. J. Kreuzer: *Nonequilibrium thermodynamics and its statistical foundations*, Clarendon Press, Oxford (1983).

[108] G. Lattanzi and A. Maritan: *Master equation approach to molecular motors*, Phys. Rev. E **64**, 061905 (2001).

[109] S. H. Lee and D.G. Grier: *Flux reversal in two-state symmetric optical thermal ratchet*, Phys. Rev. E **71**, 060102(R) (2005).

[110] J. M. J. van Leeuwen and A. Drzevinski: *Stochastic lattice models for the dynamics of linear polymers*, Phys. Rep. **475**, 53 (2009).

[111] R. B. Lehoucq and D. C. Sorensen: *Deflation techniques for an implicitly restarted Arnoldi iteration*, SIAM J. Matrix Analysis and Applications **17**, 789 (1996).

[112] R. B. Lehoucq, D. C. Sorensen, and C. Yang: *ARPACK Users Guide: Solution of Large Scale Eigenvalue Problems with Implicitly Restarted Arnoldi Methods*, SIAM, Philadelphia (1998).

[113] D. A. Levin, Y. Peres, and E. L. Wilmer: *Markov Chains and Mixing Times*, American Mathematical Society, Providence (2008).

[114] H. Liu and J. Wang: *A new way to enumerate cycles in graph*, AICT/ICIW Conference Proceedings, 0-7695-2522-9/06 (2006).

[115] A. Lo and R. T. Skodje: *Diffusion and evaporation kinetics of large islands and vacancies on surfaces*, J. Chem. Phys. **111**, 2726 (1999).

[116] T. P. Lodge: *Reconciliation of the Molecular Weight Dependence of Diffusion and Viscosity in Entangled Polymers*, Phys. Rev. Lett. **83**, 3218 (1999).

[117] L. Lovasz: *Random Walks on Graphs: A survey*, Combinatorics, Paul Erdos is Eighty **2**, 1 (1993).

[118] M. O. Magnasco: *Forced thermal ratchets*, Phys. Rev. lett. **71**, 1477 (1993).

[119] K. Mallick: *Some Exact Results for the Exclusion Process*, J. Stat. Mech. **1**, P01024 (2011); G. Terranova, H. O. Mártin, and C. M. Aldao: *Drift velocity for a chain of beads in one dimension*, Phys. Rev. E **74**, 021116 (2006); Y. Lee, A. Allison, D. Abbott, and H. E. Stanley: *Minimal Brownian Ratchet: An Exactly Solvable Model*, Phys. Rev. Lett. **91**, 220601 (2003); B. Derrida, M. R. Evans, V. Hakim, and V. Pasquier: *Exact solution of a 1D asymmetric exclusion model using a matrix formulation*, J. Phys. A: Math. Gen. **26**, 1493 (1993); B. Derrida, M. R. Evans, and K. Mallick: *Exact diffusion constant of a one-dimensional asymmetric exclusion model with open boundaries*, J. Stat. Phys. **79**, 833 (1995); G. M. Schütz: *Exact solution of the master equation for the asymmetric exclusion process*, J. Stat. Phys. **88**, 427 (1997); R. J. Baxter: *Exactly Solved Models in Statistical Mechanics*, Academic Press, London (1982); F. Y. Wu: *Exactly Solved Models: A Journey In Statistical Mechanics: Selected Papers with Commentaries (1963-2008)*, World Scientific (2009); G. M. Schütz: *Exactly solvable models for many-body systems far from equilibrium*, Phase Transitions and Critical Phenomena **19**, 1 (2001).

[120] U. M. B. Marconia, A. Puglisi, L. Rondonic, and A. Vulpiani: *Fluctuation-dissipation: Response theory in statistical physics* Physics Reports **461**, 111 (2008).

[121] J. L. Mateos: *A random walker on a ratchet*, Physica A **351**, 79 (2005).

[122] H. Mehl, O. Biham, O. Millo, and M. Karimi: *Electromigration-induced flow of islands and voids on the Cu(001) surface*, Phys. Rev. B **61**, 4975 (2000).

[123] J. Merikoski, I. Vattulainen, J. Heinonen, and T. Ala-Nissilä: *Effect of Kinks and Concerted Diffusion Mechanisms on Mass Transport and Growth on Stepped Metal Surfaces*, Surf. Sci. **387**, 167 (1997).

[124] G. Mills, T. R. Mattsson, L. Møllnitz, and H. Metiu: *Simulations of mobility and evaporation rate of adsorbate islands on solid surfaces*, J. Chem. Phys. **111**, 8639 (1999).

[125] C. Moler and C. Van Loan: *Nineteen Dubious Ways to Compute the Exponential of a Matrix, Twenty-Five Years Later*, SIAM Review **45**, 3 (2003).

[126] M. E. J. Newman and G. T. Barkema: *Monte Carlo methods in statistical physics*, Oxford university Press, Oxford (2001).

[127] M. A. Nielsen and I. L. Chuang: *Quantum Computation and Quantum Information*, Cambridge University Press, Cambridge (2000).

[128] J. Nocedal and S. J. Wright: *Numerical Optimization*, Springer, New York (2006).

[129] J. R. Norris: *Markov Chains*, Cambridge University Press, New York (1998).

[130] M. Paeßens and G. M. Schütz: *Density matrix renormalization group studies of the effect of constraint release on the viscosity of polymer melts*, Phys. Rev. E **66**, 021806 (2002).

[131] J. M. R. Parrondo: *Reversible ratchets as Brownian particles in an adiabatically changing periodic potential*, Phys. Rev. E **57**, 7297 (1998); R. D. Astumian and I. Derenyi: *A Chemically Reversible Brownian Motor: Application to Kinesin and Ncd*, Biophys. J. **77**, 993 (1999); R. D. Astumian: *Adiabatic operation of a molecular machine*, PNAS **104**, 19715 (2007);

[132] J. M. R. Parrondo and B. J. de Cisneros: *Energetics of Brownian motors: a review*, Appl. Phys. A **75**, 179 (2002).

[133] J. M. R. Parrondo, G. P. Harmer, and D. Abbott: *New Paradoxical Games Based on Brownian Ratchets*, Phys. Rev. Lett. **85**, 5226 (2000).

[134] P. Pasciak, K. Kulakowski, and E. Gudowska-Nowak: *Diffusion coefficient in an electrophoretic asymmetrically tilting ratchet*, Acta Physica Polonica B **36**, 1737 (2005); P. Pasciak, M. J. Krawczyk, E. Gudowska-Nowak, and K. Kulakowski: *Diffusion of DNA Molecules in Gel at High Electric Fields*, J. Biol. Phys. **31**, 365 (2005).

[135] S. Peles, B. Munsky and M. Khammash: *Reduction and solution of the chemical master equation using time scale separation and finite state projection*, J. Chem. Phys. **125**, 204104 (2006).

[136] E. Penev, P. Kratzer, and M. Scheffler: *Effect of strain on surface diffusion in semiconductor heteroepitaxy*, Phys. Rev. B **64**, 085401 (2001); M. I. Larsson, K. Cho, and B. M. Clemens: *Surface diffusion mechanisms for strain-induced self-assembly*, Phys. Rev. B **69**, 155426 (2004); W. Xiao, P. A. Greaney, and D. C. Chrzan: *Pt adatom diffusion on strained Pt(001)*, Phys. Rev. B **70**, 033402 (2004); W. Xiao, P. A. Greaney, and D. C. Chrzan: *Adatom Transport on Strained Cu(001): Surface Crowdions*, Phys. Rev. Lett. **90**, 156102 (2003); Z. Duan and W. Xiao: *Cu dimer diffusion on strained Cu(001)*, Surf. Sci. **604**, 337 (2010).

[137] O. Pierre-Louis and T. L. Einstein: *Electromigration of single-layer clusters*, Phys. Rev. B **62**, 13697 (2000); M. Schimschak and J. Krug: *Electromigration-Induced Breakup of Two-Dimensional Voids*, Phys. Rev. Lett. **80**, 1674 (1998); P. Kuhn and J. Krug: *Islands in the Stream: Electromigration-Driven Shape Evolution with Crystal Anisotropy*, International Series of Numerical Mathematics **149**, 159 (2005); P. Kuhn, J. Krug, F. Hausser and A. Voigt: *Complex Shape Evolution of Electromigration-Driven Single-Layer Islands*, Phys. Rev. Lett. **94**,

166105 (2005); F. Hausser, S. Rasche and A. Voigt: *The influence of electric fields on nanostructures: simulation and control*, Mathematics and Computers in Simulation **80**, 1449 (2010).

[138] M. Plischke and B. Bergersen: *Equilibrium statistical physics*, World Scientific Publishing, Singapore (1994).

[139] V. N. Pokrovskii: *The Mesoscopic Theory of Polymer Dynamics*, Springer (2010).

[140] M. Porto, M. Urbakh and J. Klafter: *Hopping motion of interacting particles: From time-dependent interaction to directed transport*, Phys. Rev. E **65**, 011108 (2001).

[141] J. Prost, J.-F. Chauwin, L. Peliti, and A. Ajdari: *Asymmetric Pumping of Particles*, Phys. Rev. Lett **72**, 2652 (1994); J.-F. Chauwin, A. Ajdari, and J. Prost: *Current Reversal in Asymmetric Pumping*, Europhys. Lett. **32**, 373 (1995).

[142] H. Qian and M. Qian: *Pumped Biochemical Reactions, Nonequilibrium Circulation, and Stochastic Resonance*, Phys. Rev. Lett. **87**, 2271 (2000).

[143] M. Qian, M.-P. Qian, and X.-J. Zhang: *Fundamental facts concerning reversible master equations*, Physics Letters A **309**, 371 (2003).

[144] S. Rahav, I. Gilary, and S. Fishman: *Effective Hamiltonians for periodically driven systems*, Phys. Rev. A **68**, 013820 (2003).

[145] N. Rajewsky, L. Santen, A. Schadschneider and M. Schreckenberg: *The asymmetric exclusion process: Comparison of update procedures*, J. Stat. Phys. **92**, 151 (1998); C. Appert-Rolland, J. Cividini and H. Hilhorst: *Frozen shuffle update for an asymmetric exclusion process on a ring*, J. Stat. Mech. **7**, P07009 (2011).

[146] C. V. Rao and A. V. Arkin: *Stochastic chemical kinetics and the quasi-steady-state assumption: Application to the Gillespie algorithm*, J. Chem. Phys. **118**, 4999 (2003); S. MacNamara, A. M. Bersani, K. Burrage and R. B. Sidje: *Stochastic chemical kinetics and the total quasi-steady-state assumption: Application to the stochastic simulation algorithm and chemical master equation*, J. Chem. Phys. **129**, 095105 (2008).

[147] D. H. Redelmeier: *Counting polyominoes: Yet another attack*, Discrete Mathemetics **36**, 191 (1981).

[148] P. Reimann: *Brownian motors: noisy transport far from equilibrium*, Phys. Rep. **361**, 57 (2002).

[149] R. Retkute and J. P. Gleeson: *Role of interaction on noise-induced transport of two coupled particles in Brownian ratchet devices*, Fluctuation and noise letters **6**, 3 (2006).

[150] M. J. E. Richardson and G. M. Schütz: *Inhomogeneous reptation of polymers*, Physica A **235**, 440 (1996).

[151] L. M. Rios and N. L. Sahinidis: *Derivative-free optimization: A review of algorithms and comparison of software implementations*, (unpublished) `http://thales.cheme.cmu.edu/dfo`.

[152] H. Risken: *The Fokker-Planck Equation: Methods of Solutions and Applications*, Springer-Verlag, New York (1996).

[153] P. J. Rous: *Theory of surface electromigration on heterogeneous metal surfaces*, Applied surface science **175**, 212 (2001).

[154] P. E. Rouse: *A Theory of the Linear Viscoelastic Properties of Dilute Solutions of Coiling Polymers*, J. Chem. Phys. **21**, 1272 (1953).

[155] V. M. Rozenbaum and T. E. Korochkova: *Analytical Model of a Brownian Motor with a Fluctuating Potential*, Journal of Experimental and Theoretical Physics **100**, 218 (2005).

[156] M. Rubinstein: *Discretized model of entangled-polymer dynamics*, Phys. Rev. Lett. **59**, 1946 (1987).

[157] M. Rusanen, P. Kuhn, and J. Krug: *Kinetic Monte Carlo simulations of oscillatory shape evolution for electromigration-driven islands*, Phys. Rev. B **74**, 245423 (2006).

[158] Y. Saad: *Overview of Krylov subspace methods with application to control problems*, Report MTNS89, RIACS, NASA Ames Research center, Moffett Field (1989).

[159] Y. Saad: *Iterative methods for sparse linear systems*, SIAM, Philadelphia (2000).

[160] Y. Saad: *Numerical methods for large eigenvalue problems*, SIAM (2011);

[161] M. Salehi and T. J. Perkins: *Maximum probability reaction sequences in stochastic chemical kinetic systems*, Frontiers in physiology **1**, 170 (2010).

[162] P. Salo, J. Hirvonen, I. T. Koponen, O. S. Trushin, J. Heinonen, and T. Ala-Nissilä: *Role of concerted atomic movements on the diffusion of small islands on fcc(100) metal surfaces*, Phys. Rev. B **64**, 161405(R) (2001).

[163] J. R. Sanchez and J. W. Evans: *Diffusion of small clusters on metal (100) surfaces: Exact master-equation analysis for lattice-gas models*, Phys. Rev. B **59**, 3224 (1999).

[164] G. Sartoni and J. M. J. van Leeuwen: *Reptation in linear systems*, Phys. Rev. E **57**, 3088 (1998).

[165] J. Schnakenberg: *Network theory of microscopic and macroscopic behavior of master equation systems*, Rev. Mod. Phys. **48**, 571 (1976).

[166] U. Schollwöck: *The density-matrix renormalization group*, Rev. Mod. Phys. **77**, 259 (2005); U. Schollwöck: *The density-matrix renormalization group in the age of matrix product states*, Ann. Phys. (NY) **326**, 96 (2011); M. N. Reinhard and S. R. Manmana: *Diagonalization- and Numerical Renormalization-Group-Based Methods for Interacting Quantum Systems*, AIP Conf. Proc. **789**, 93 (2004); G. De Chiara, M. Rizzi, D. Rossini, and S. Montangero: *Density Matrix Renormalization Group for Dummies*, Journal of Computational and Theoretical Nanoscience **5**, 1277 (2008); U. Schollwöck and S. R. White: *Methods for Time Dependence in DMRG*, AIP Conf. Proc. **816**, 155 (2005); J. J. Garcia-Ripoll: *Time evolution of Matrix Product States*, New Journal of Physics **8**, 305 (2006).

[167] H. Shao, P. C. Weakliem, and H. Metiu: *Evaporation of single atoms from an adsorbate island or a step to a terrace: Evaporation rate and the underlying atomic-level mechanism*, Phys. Rev. B **53**, 16041 (1996).

[168] Z.-P. Shi, Z. Zhang, A. K. Swan, and J. F. Wendelken: *Dimer Shearing as a Novel Mechanism for Cluster Diffusion and Dissociation on Metal (100) Surfaces*, Phys. Rev. Lett. **76**, 4927 (1996).

[169] T. Shimokawa and K. Mouri: *The enhancement of the energetic efficiency by the cooperation of low-efficient flashing ratchets*, BioSystems **88**, 316, (2007); K. Mouri and T. Shimokawa: *Effect of the number of molecules on the energetic efficiency in molecular motors using the Flashing Ratchet model*, Physica A **387**, 5169 (2008).

[170] R. B. Sidjea and W. J. Stewartb: *A numerical study of large sparse matrix exponentials arising in Markov chains*, Computational Statistics and Data Analysis **29**, 345 (1999).

[171] G. W. Slater, H. L. Guo, and G. I. Nixon: *Bidirectional Transport of Polyelectrolytes Using Self-Modulating Entropic Ratchets*, Phys. Rev. Lett. **78**, 1170 (1997); L. L. Frumin, S. E. Peltek, and G. V. Zilberstein: *Nonlinear focusing of DNA macromolecules*, Phys. Rev. E **64**, 021902 (2001); A. Marziali, J. Pel, D. Bizzotto, L. A. Whitehead: *Novel electrophoresis mechanism based on synchronous alternating drag perturbation*, Electrophoresis **26**, 82 (2005).

[172] G. W. Slater, S. Guillouzic, M. G. Gauthier, J.-F. Mercier, M. Kenward, L. C. McCormick, and F. Tessier: *Theory of DNA electrophoresis*, Electrophoresis **23**, 3791 (2002); E. H. C. Lai and B. W. Birren: *Electrophoresis of Large DNA Molecules: Theory and Applications*, Cold Spring Harbor, NY (1990); J.-L. Viovy: *Electrophoresis of DNA and other polyelectrolytes: Physical mechanisms*, Rev. Mod. Phys. **72**, 813 (2000).

[173] G. L. G. Sleijpen and D. R. Fokkema: *BiCGstab for Linear Equations involving Unsymmetric Matrices with Complex Spectrum*, ETNA **1**, 11 (1993); G. L. G. Sleijpen, H. A. van der Vorst, and D. R. Fokkema: *BiCGstab(l) and other hybrid Bi-CG methods*, Numerical Algorithms **7**, 75 (1994).

[174] M. von Smoluchowski: *Experimentell nachweisbare, der Ublichen Thermodynamik widersprechende Molekularphenomene*, Phys. Zeitshur. **13**, 1069 (1912).

[175] I. M. Sokolov and A. Blumen: *Non-equilibrium directed diffusion and inherently irreversible heat engines*, J. Phys. A: Math. Gen. **30**, 3021 (1997); I. M. Sokolov and A. Blumen: *Thermodynamical and mechanical efficiency of a ratchet pump*, Chemical Physics **235**, 39 (1998).

[176] D. C. Sorensen: *Implicit Application of Polynomial Filters in a k-Step Arnoldi Method*, SIAM. J. Matrix Anal. & Appl. **13**, 357 (1992).

[177] D. W. Stroock: *An Introduction to Markov Processes*, Springer, Berlin (2005).

[178] E. Stukalin and A. Kolomeisky: *Transport of single molecules along the periodic parallel lattices with coupling*, J. Chem. Phys. **124**, 204901 (2006).

[179] S. X. Sun: *Path Summation Formulation of the Master Equation*, Phys. Rev. Lett. **96**, 210602 (2006); B. Harland and S. X. Sun: *Path ensembles and path sampling in nonequilibrium stochastic systems*, J. Chem. Phys. **127**, 104103 (2007).

[180] D. Suzuki and T. Munakata: *Rectification efficiency of a Brownian motor*, Phys. Rev. E **68**, 021906 (2003).

[181] U. M. Titulaer and J. M. Deutch: *Some aspects of cluster diffusion on surfaces*, J. Chern. Phys. **77**, 472 (1982); Victor Pereyra, Andrey Milchev, and Victor Fleurov: *Diffusion of single particles in cellular media*, Phys. Rev. E **50**, 4636 (1994); Z. Koza: *General technique of calculating the drift velocity and diffusion coefficient in arbitrary periodic systems*, J. Phys. A: Math. Gen. **32**, 7637 (1999).

[182] T. Vicsek: *Fluctuations and scaling in biology*, Oxford University Press, Oxford (2001).

[183] A. F. Voter: *Classically exact overlayer dynamics: Diffusion of rhodium clusters on Rh(100)*, Phys. Rev. B **34**, 6819 (1986).

[184] C. Vuik: *Iterative solution methods*, (unpublished) `http://ta.twi.tudelft.nl/users/vuik/burgers/lin_notes.pdf`, Delft Institute of Applied Mathematics (2011).

[185] H. Wang: *Chemical and mechanical efficiencies of molecular motors and implications for motor mechanisms*, J. Phys.: Condens. Matter **17**, 3997 (2005).

[186] H. Wang: *Several Issues in Modeling Molecular Motors*, J. Comput. Theor. Nanosci. **5**, 1 (2008).

[187] H. Wang and J. D. Bao, *Transport coherence in coupled Brownian ratchet*, Physica A **374**, 33 (2006).

[188] H. Wang and T. C. Elston: *Mathematical and computational methods for studying energy transduction in protein motors*, J. Stat. Phys. **128**, 35 (2007).

[189] H. Wang and G. Oster: *The Stokes efficiency for molecular motors and its applications*, Europhys. Lett. **57**, 134 (2002).

[190] Z. Wang and M. Li: *Force-velocity relations for multiple-molecular-motor transport*, Phys. Rev. E **80**, 041923 (2009).

[191] S. Warshall: *A theorem on Boolean matrices*, Journal of the ACM **9**, 11 (1962).

[192] R. Weiss: *A theoretical overview of Krylov subspace methods*, Applied Numerical Mathematics **19**, 207 (1995).

[193] B. Widom, J. Viovy, and A. Defontaines: *Repton model of gel electrophoresis and diffusion*, J. Phys. I France **1**, 1759 (1991).

[194] H. S. Wio: *An introduction to stochastic processes and nonequilibrium statistical physics*, World Scientific, Singapore (1994).

[195] S. R. White: *Density matrix formulation for quantum renormalization groups*, Phys. Rev. Lett. **69**, 2863 (1992); S. R. White: *Density-matrix algorithms for quantum renormalization groups*, Phys. Rev. B **48**, 10345 (1993).

[196] B. Yan, R. Miura, and Y. D. Chen: *Direction Reversal of Fluctuation-induced Biased Brownian Motion on Distorted Ratchets*, J. Theor. Biol. **210**, 141 (2001).

[197] R. Yasuda, H. Noji, M. Yoshida, K. Kinosita Jr., and H. Itoh: *Resolution of distinct rotational substeps by submillisecond kinetic analysis of F1-ATPase*, Nature **410**, 898 (2001); H. Itoh, A. Takahashi, K. Adachi, H. Noji, R. Yasuda, M. Yoshida, and K. Kinosita Jr.: *Mechanically driven ATP synthesis by F1-ATPase*, Nature **427**, 465 (2004); A. Yildiz, M. Tomishige, R. D. Vale and P. R. Selvin: *Kinesin Walks Hand-Over-Hand*, Science **303**, 676 (2004); S. Toba, T.

M. Watanabe, L. Yamaguchi-Okimoto, Y. Y. Toyoshima, and H. Higuchi: *Overlapping hand-over-hand mechanism of single molecular motility of cytoplasmic dynein*, Proc. Natl. Acad. Sci. USA **103**, 5741 (2006).

[198] J. Zhuang, Z. Sun, W. Zhang, M. Zhuang, X. Ning, L. Liu, and Y. Li: *Structures and magic numbers of adatom clusters on metal fcc(001) surfaces*, Phys. Rev. B **69**, 165421 (2004).

[199] Y. Zhou and J. D. Bao: *Optimal number of disperse states in the model of Brownian motors*, Physica A **343**, 515 (2004).

[200] R. K. P. Zia and B. Schmittmann: *A possible classification of nonequilibrium steady states*, Journal of physics A: Mathematical and general **39**, L407 (2006); R. K. P. Zia and B. Schmittmann: *Probability currents as principal characteristics in the statistical mechanics of non-equilibrium steady states*, J. Stat. Mech. **07**, P07012 (2007).

[201] `http://science.energy.gov/bes/efrc/research/grand-challenges`